Development of cell confinement and manipulation microfluidics and methods for optimal biopreservation

Cifeng Fang

A dissertation
submitted in partial fulfillment of the
requirements for the degree of

Doctor of Philosophy

University of Washington

2017

Reading Committee:

Dayong Gao, Chair

Jaehyun Chung, Chair

Alberto Aliseda

Program Authorized to Offer Degree:
Mechanical Engineering

University of Washington

Abstract

Development of cell confinement and manipulation microfluidics and methods for optimal biopreservation

Cifeng Fang

Co-Chairs of the Supervisory Committee:
Professor Dayong Gao
Mechanical Engineering

Professor Jaehyun Chung
Mechanical Engineering

Biopreservation, especially cryopreservation, of bio-samples, includeing DNA/RNA, proteins, bio-fluids, cells, tissues and organs, has attracted more and more attentions, because of its great support in clinical research and trials. The successful biopreservation of bio-samples enables the cellular therapy, drug development and diagnosis of disease. To achieve the best biopresration result, various of factors and steps need to be optimized, including selection of the optimal cryoprotective agent (CPA), successful addition of CPA, optimization of the cooling protocol, thawing of the frozen samples, removal of CPA after thawing, and others. Cryobiologists rely on the theoretical interpretation of bio-heat and mass transfer and novel measurement techniques to design optimal cryopreservation protocol. In this dissertation, cell confinement and manipulation devices were developed to determine the fundamental cryobiological properties of cells, and a novel across cell membrane temperature dependent mass transfer model were investigated with measurement methods proposed.

Determianation of the intrinsic cryobiological characteristics of the cells is the very first steps of cryopreservation protocol optimization, which includes the cell membrane permeabilities to water and the CPA at different temperatures, the osmotically inactive cell volume, the activation energy of water/CPA transport across cell membranes, osmotic tolerance limit,

sensitivity to the CPA toxicity and others. To determine these cyobiological properties, two kinds of microfluidic device are proposed and applied: a microfluidic perfusion channel and non-contact cell confinement and manipulation platform.

Studying the phase contrast microscopy of cell volume excursion history when perfused with solutions is the common method to evaluate the cell membrane properties, which requires the measurement devices equiped with features as followed: (1) steadily trap cells for long time; (2) change the extracellular media cell exposed to; (3) control and monitor the extracellular media temperature and the whole cell volume excursion history can be recorded and easily analyzed.

The microfluidic perfusion channel is used to determine the cell membrane transport properties of human vaginal mucosal immune cells (T cells and macrophages), because of their importance in HIV vaccine research. The cell membrane permeabilities to four different CPAs (Dimethyl sulfoxide (DMSO), glycerol, propylene glycol and ethylene glycol) at room temperature are measured, indicating that DMSO and propyleneglycol could be a potencial CPA options, while glycerol is not a good choice for these cells as to the slow across membrane transport of which.

Though a low cost and easy to operate tool the microfuidic perfusion channel is, the challenges, like the intense images processing effort, due to the shadow from the blocker, lack of on-chip temeprature control, remain to be solved for better measurement precision and efficiency. To overcome the challenges unsolved in microfludic perfusion channel, a cell confinement and manipulation platform with instananous flow and local temperature control was developed. Numerical simulation of in-channel laminar flow coupled heat transfer was coducted to exam various heater desgins, to achieve the best temperature uniformity and heating efficiency. The fabrication protocol was developed and tested to provide the optimal device performance of the integrated microfludics.

With the developed cell confinement and manipulation platform, two practices of cell membrane properties measurement were executed, with both the traditional mass transfer model under static temperatures and the originally proposed temperature dependent mass transfer model. With the assist of the numerical simulation of temperature dependent mass transfe model, the temperature profile during the measurmenet was identified and used for the estimation of activation energy.

The further development vista beyond the projects covered in this dissertation was also discussed, including the integration of on-chip active cooling design, options to scale up current system, and some other applications, for instance exploring new potencial CPAs.

TABLE OF CONTENTS

LIST OF FIGURES

LIST OF TABLES

GLOSSARY

A: Area, μm^2

B: Colling rate, K/min

C: Concentration or osmolality (Osm/kg water)

CPA: cryoprotective agent

E_A: Arrhenius activation energy, kcal/mole

L_P: Membrane permeability to water, $\mu m/(atm \cdot min)$

$L_{P,0}$: Membrane permeability to water at reference temperature Tr, $\mu m/(atm \cdot min)$

N: Number of osmoles

P_S: Membrane permeability of CPA, cm/min

R: Radius (μm), or normalized concentration of NaCl with respective to that in isotonic NaCl solution

R: Universal gas constant, 0.008207 $atm\ L/(mole \cdot K)$

T: Absolute temperature, K

T0: reference temperature (=295.15K)

V: Volume, μm^3

V_O: Isosmotic cell volume

V_C: Total cell volume (at time t)

V_N: V (normalized) = V_c/V_o

$\widehat{V}$: Partial volume, μm^3

V_B: Osmotically-inactive volume or volume fraction, μm^3 or %

V_W: The specific molar volume of water

σ: Reflection coefficients of cell membrane to CPA

σ_{NI}: Sigma noninteracting (no solutesolvent flux interaction present)

V_0: Molar volume, $\mu m^3/mole$

N_S: Osmoles of solute, moles

C, N, O, S, W: Subscripts (c, total cellular; n, nonpermeating solute; o, initial value; s, permeating solute; w, water)

E, I: Superscripts (e, external to cell; i, internal to cell)

ACKNOWLEDGMENTS

I would like to express my earnest gratitude to my supervisors Prof. Dr. Dayong Gao and Prof. Dr. Jae-Hyun Chung, who always support me and my projects, inspire and encourge me to move forward in my research. I would also like to thank my committee membrers, Prof. Dr. Alberto Aliseda and Prof. Dr. Shaoyi Jiang for their input to this work.

I wishes to express sincere appreciation to everyone in Center for Cryo-Biomedical Engineering and Artificial Organs at University of Washington, where I has had the opportunity to work with the world best researchers and greaduate students like Dr. Zhiquan Shu, Dr. Fujun Ji, Jiaji Pan, Ruoxin Wang, Jinyuan Zhang, Shen Ren, Ji Peng; to Dr. Florian Hladik and Mr. Sean M. Hughes from Fred Hutchinson Cancer Research Center; to Prof. Dr. Amy Shen Fried and Dr. Doojin Lee from Okinawa Institute of Science and Technology Graduate University, Japan.

Especially, I give my special thanks to my family. This dissertation would never have been completed without their encouragement and devotion.

DEDICATION

to my dear wife, Eve, and my family

Chapter 1

INTRODUCTION

1.1 Background

Cellular therapy is the therapy that cellular material is injected into a patient. As a novel therapy method brenthing from the field of regenerative medicine, it has transited from basic research/pre-clinical animal model testing into actual clinical evaluation for numerous therapeutic disease areas including cancer, heart disease, bone/cartilage, neurodegenerative, diabetes, gastrointestinal, and autoimmunity. Immune cell therapy specially relies on cell-mediated immunity by injecting activated T cell into a patient modulate the immune responses to fight against cancer cells. Most recently, the guide line of P4 medicine (Predictive, Preventive, Personalized and Participatory) boost the progress of cellular therapy into the direction of more prcise and customized healthcare method. Fourteen cellular therapy products, with a $10 billion market size (2016), have been approved for used in USA. With the anticipatd approval of additional products the global market of cellular therapy is expected to grow at an average annual growth rate of 30%, reaching an amount of $32 billion at 2018, as shown in Fig. 1.1.

A general cellular therapy procedures consist of: harvest cells or tissues from donor, treatment cell separation, preservation of collected cells, thawing and activation of preserved cells and inject the cells back to the patient for the treatment. All these steps are crucial for the success of cellular therapy. During the past few decades, scientists and engineers have created various novel protocols and techniques to optimize these procedures, amount which biopreservation is one of the most challenging yet critical techniques, as to its cell type sensitive nature.

In this dissertation, I will focus on developing tools that assist the determination of

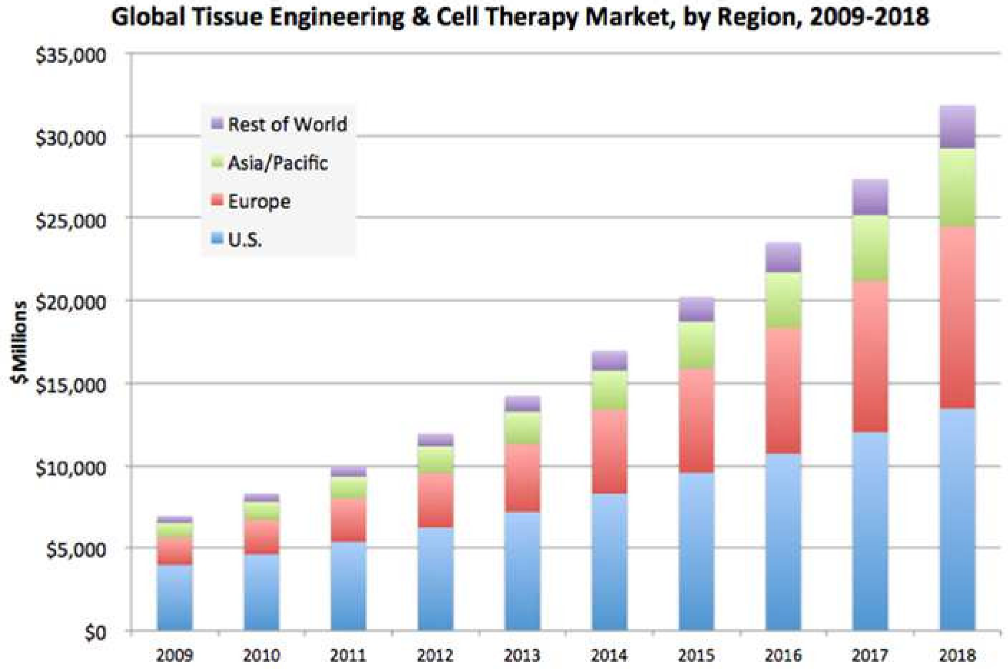

Figure 1.1: Global market predition of tissue engineering & cell therapy [1]

cellular properties and investigeting novel measurement methods, for optimal biopreservation protocol.

1.2 *Cryobiology and cryopreservation*

Cryobioloy studies the interaction of cells, tissue, organ and other biomaterials with extremely low temperature [2], involving injury mechanism, bio-heat and mass transfer modeling of biomaterials experiencing low temperature and methods to help biomaterials survive extremely low termperature. Cryopreservation is the technology that suspends the ”clock” of biomaterials. The underlaying mechamsm of live materials cryopreservation is that chemical reactions and metabolism activities will be slowed down or even paused at low temperatures. Cryopreservatioin is an ideal method for the long term storage of biomaterials as it can truely slow down or halte the ”life clock” of biomaterials (RNA, DNA, cells, tissues, etc.) and then resume it after thawing to normal tempeartures. People can’t preserve mammalian cells, until 1949, when Polge et al. succeeded in cryopreserving bull sperm with glycerol in liquid nitrogen [5]. Since then, cryopreservation has been widely explored and applied for long-term storage of DNA/RNA, proteins, bio-fluids, cells, tissues and organs. The study of cryobiology and cryopreservation filled the needs in various fields from fundamental research to clincial practice. For instance, the successful cryopreservation of human sperm make human sperm long-term storge possible, until being used for fertilization. Stem cells (from bone marrow, cord blood or peripheral blood) have been cryopreserved, transported and then tranplanted to patients to treat many kinds of diseases since the 1950s [6], which includes but not limites to Hodgkin's and non-Hodgkin's lymphoma [7–15], chemosensitive/lymphoid/myeloid/hematological maligencies [10–13], osteogenic/fibro-/Ewing sarcoma [8] myeloid or lymphoblastic leukemia [10–13], solid tumors (testis, breast) [8, 10, 11].

With unique opportunities provided by the discovery and development of cryopreservation, cryopreservation is widely utilized in varoious applications. Cells and tissue banking assist the cinical research and applications. Both healthy and diseased cells and tissues have the need to be preserved. The cryopreservation of healthy cells and tissue enables new treatments and surgeries possiblity. For example, the cryopreservation of heathly bone marrow avoids the damage from radiotherapy and chemotherapy during the treatment of leukemia, which offers flexibility for therapy options. On the other hand, the cryopreservation of diseased cells/tissues assists the disease and drug development. Moreover, with cryopreservation, the tissues and organs from the donor can be stored for a longer waiting time before transplanted to a succeefully matched patient. As a result, cryopreservation increases the chance of successful dornor-recipient screening and mathcing. Moreover, as biomaterials' function and sturcture can be maintained stable via cryopreservation, cryopreservation also enables the transportation of biomaterials.

However, even with decades of reasearch, many types of cell being successully cryopreserved, more kinds of cells still can't be cryopreserved. This is because of the "cryo-injuries" that happen during freezing and thawing processes. In 1970s, Mazur proposed a "two-factor hypothesis" of cryoinjuries [3], as shown in Fig. 1.2. According to Mazurs two-factor hypothesis [3], two different kinds of injuries may happen to cells during cooling: (1) when the cooling rate is too fast, a large amount of water will remain inside the cell and be crystallized, causing intercellular ice formation (IIF) injury; (2) on the other hand, when the cooling rate is too slow, water has enough time to travel out of cell before ice formation happens, raising intercellular medium concentration excessively, causing osmotic and solute injury to the cell. Hence, an optimal cooling procedure should be slow enough to avoid IIF injury and fast enough to avoid the solute injury. Such optimal cooling rate is determined by the temperature-dependent cell membrane permeabilities. As a result, according to this "two-factor hypothesis" (ice injury with high cooling rate and solution injury with low cooling rate), there is an inverted "U" shape of the relationship between cell survival rate and the cooling rate [3], as shown in Fig. 1.3. Beside the existance of the optimal cooling rate, we can see that this optimal cooling rate is cell type dependent. Hence, there is an optimal cooling rate for a specific type of cells, which should be determined by the properties of the cell membranes for an optimal cryopreservation.

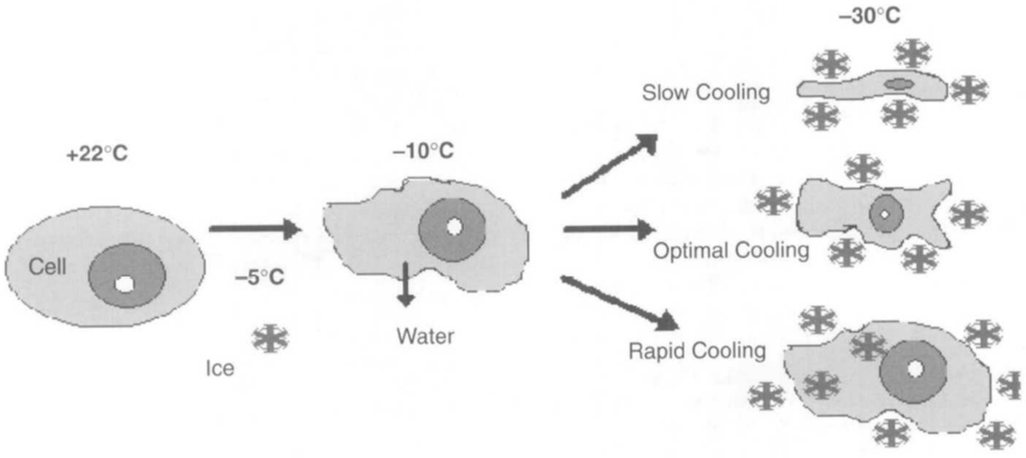

Figure 1.2: "Two-Factor Hypothesis" of cryoinjury [2]

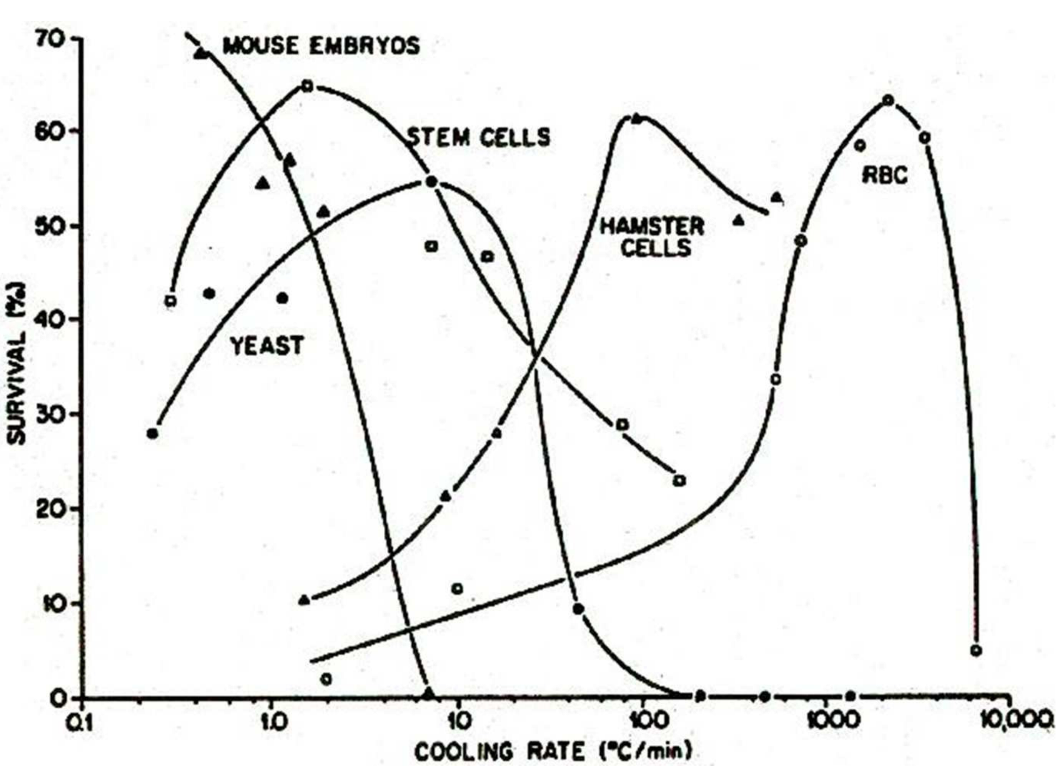

Figure 1.3: Survival of mouse marrow stem cells, yeast, mouse sperm, and human red cells as function of cooling rate [3]

1.3 Cryoprotective agent (CPA)

There are limits to reduce cryo-injuries by using the optimal cooling rate. To further decrease cryoinjuries, specific chemical agents, named cryoprotectants, or cryoprotective agents (CPA) should be added to cell suspension before freezing. Since glycerols protective function in sperm cryopreservation is revealled in 1949, modern cryobiology has established with systematic research about both cryobiological properties of biomaterials and new types of CPA. After that, more than 100 types of CPAs have been used, such as glycerol, dimethyl sulfoxide (DMSO), propylene glycol (PG), ethylene glycol (EG), sucrose, trehalose, dextran, hydroxyethyl starch (HES), Polyvinylpyrrolidone (PVP), and so on. These CPAs can be classified into three categories:

(1) Permeable CPAs, such as glycerol, DMSO, EG, and PG. Permeable CPAs penetrate

into cells, decreasing the freezing temperature of the intracellular environment, and fill in the intracellular volume to compensate for the cell volume reduction due to water loss, preventing excessive cell volume excursion during cooling.

(2) Non-permeable CPAs, such as sucrose, trehalose, dextran, HES, and PVP. Although these CPAs cannot penetrate into cells. they can increase the glass transition temperature (T_g) and glass transition tendency of the extracellular environment dramatically, which supprss the ice formation during cooling.

(3) Anti-freezing proteins (AFP). AFPs function with non-colligative property, which means they do not lower the freezing temperature proportional to the AFP concentration. Since the discovery of the existence of AFP in the blood of arctic fish by Canadian scientist Scholander in 1950s [16], and isolation of AFP by DeVries in 1960s [13], AFPs have been studied and applied in many fields including cryopreservation and food industry (e.g., additives in ice cream). As the name implies, AFP can delay or prevent ice crystallization during cooling. AFPs bind to small ice crystals to inhibit the growth and recrystallization of ice. AFPs may also interact with mammalian cell membranes to protect them from cold damage.

To select an optimal CPA for a specific type of cells, one should consider: (1) the permeability of the cell membrane to the CPA; (2) the toxicity of the CPA to the cells, and (3) the availablity and cost of the CPA.

1.4 General process of cryopreservation

The general process of cell cryopreservation (Fig.1.4 (a)) includes: (1) Loading cryoprotective agent (CPA) to the cell suspension; (2) Freezing the cell suspension with specific protocol (Cooling, ice seeding and freezing); (3) Storing the samples at low temperatures; (4) Thawing the frozen samples; (5) Unloading CPA.

The following factors should be carefully considered to approach a successful cryopreservation:

a. Specific CPA or combiantion of CPAs should be chosen for the cell type according to the cell membrane properties and the CPA toxicity; b. Due to the fact that the addition

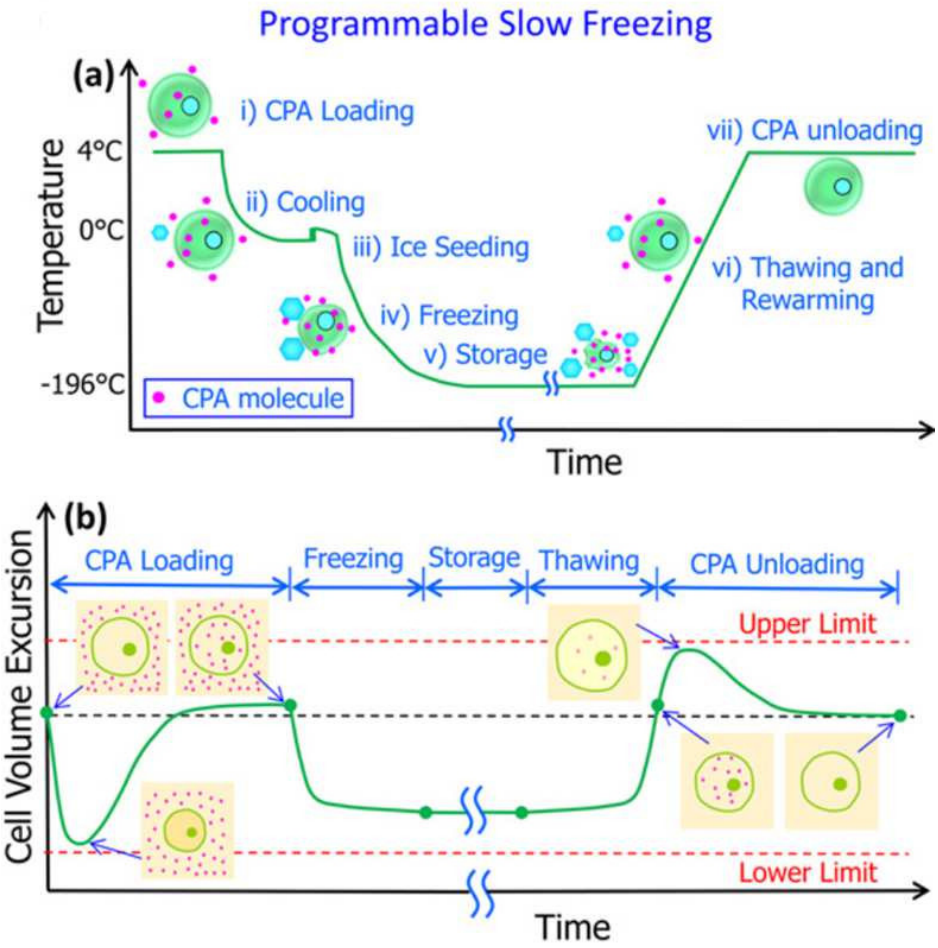

Figure 1.4: Typical thermal profiles (a) and cell volume responses (b) for slow programmable freezing [4]

of CPA introduce osmotic change to the cell, proper designed step-wised manner should be appied to avoid osmotic injury (Fig.1.4 (b)); c. Water, CPA cross membrane transport and ice formation happens simultaneously during freezing, causing ice injury and solution injury to cells, which can be subsided by applying optimal cooling rate in certain temperature range; d. Recrystallization may happen during thawing, which is also fatal to cells. So, if availalbe, ultra-fast thawing should be applied. e. During unloading of CPA, osmotic injury, cell clumping or other damage may also happen to the cells (Fig.1.4 (b)).

In a word, a successful cells cryopreservation relies on the determination of the cell type-specific optimal protocol to prevent all these possible injurites to cells. In order to investigate all these factors simultanously, a proper micro-scale manipulation platform for cellular and biological study is required, which ideally should have the following features (1) the ability to observe the cell with access to manipulate cell location; (2) control the extracelluar chemical environment cell experience; (3) manipulate the themal environment cell experience. This kind of platform involves combination of manipulatoin of momentum transfer, mass transfer and heat transfer at micro-scale.

1.5 Challenges in cryopreservation

At most cases, choosing proper and effective CPA for a cell type is the first step to successful cryopreservation. Cryobiologist choose and optimize CPA for specific cell type by measuring the intrinsic cell membrane properties, such as the cell membrane permeability to the CPA and the CPA toxicity to the cells. So far the general methods to measure the cell membrane permeability depends on the measurements of the cell volume excursion history during the cell expourse to hypertonic CPA solution. However, experiment difficulties like design of the micro-perfusion environment, data capturing and imaging analysis inhibit the accurate measuremnt of these properties in high efficiency.

The determination of optimal cooling rate for specific cell type is another core problem during the development of cryopreservation protocol for cells. It also relies on the measuremnt of the intrinsic cell properties, such as osmotically inactive cell volume, the cell membrane permeabilities to water and CPA at different temperatures, the activation evergy of water transport across cell membranes, and so on. For a non-empirical scientific study, all these properties should be measured, and subsequently be combined with the theoretical analysis of mass transfer across cell membranes to predict the optimal cooling rate. This kind of platform involves combination of manipulatoin of momentum transfer, mass transfer and heat transfer at micro-scale. An ideal micro-scale manipulation platform for cellular and biological study should have the following features: 1. the ability to observe the cell with access to manipulate cell location; 2. control the extracelluar chemical environment cell experience; 3. manipulate the themal environment cell experience.

In other word, a device that is easy-to-operate, precise and can be used to routinely measure all these intrinsic cell properties is still unavailable, yet in critical need.

1.6 Outline of this dissertation

Two core parts build up the entire dissertation. The first prat focuses on the delveloping of the inetegrated plarform for instantaneous flow and local temperature cotorl, with performace test and validation experiment conducted, which covers the chapter 2 to chapter 3. The second part showcasees two applications using the developed plarfrom, covering chapter 4 to chapter 5.

This dissertation is organized as follow.

Firstly, in Chapter 2, a microfluidic perfusion channel was employed to determine the cell membrane permeabilities to water and various CPAs at room temperatrue. The results can assist to choose the optimal CPA, design the optimal CPA addition adn removal protocols, and predict te optimal cooling rate. Human vaginal mucosal immune lymphocytes ($CD3^+$ T cells and $CD14^+$ macrophages) were adopted as model cells to demonstrate the feasibility of the microfluidic testing system because of their importance in vaccine development and microbicide tests in HIV.

However, when the microfluidic perfusion channel was applied to measure the cell properties at various temperatures, a temperature control mechanism is required. Other big limitations, like the shadow casting from the blocking barrier and the cell movement along the edge also introduce errors to the measurement result. Therefore, in Chapter 3, an integrated microfluidic system for cell confinement and manipulation was developed, with instantaneous flow and local temperature control. Moreover, the limitation of current cell manipulation platform and desired design criteria is discussed. Flow and temperature control performance of the developed platform is also evaluated.

Then, the developed cell confinement and manipulation platform was applied to determine the cell membrane permeabilities. Human acute lymphoblastic leukemia cells (Jurkat, Clone E6-1) are used as the model cell to demonstrate the feasibility of the platform. Chapter 4 ultilizes the across cell membrane under static temeprture conditons to interpret the cell volume excursion during exposure to hypertonic CPA solution, for the determination of cell membrane permeabilities.

One step further, in Chapter 5, a direct measuremnt method of the activation energy of cell mebmrane permeabilities, with the coupled across cell membrane mass transfer model under temperature dynamic, is proposed and investigted by numerical simulation. Applying the optimal temperature scanning profile, the activation energy of cell membrane permeabilities is obtained with single measurement experiment.

Finally, Chapter 6 wraps up the entire dissertation with conclusions and future work.

Chapter 2

DETERMINATION OF CELL MEMBRANE PROPERTIES AT ROOM TEMPERATURE WITH A MICROFLUIDIC PERFUSION CHANNEL

In this chapter, a contact cell confinement device, the microfluidic perfusion channel, was appied into the determination of cell (T cells and macrophasges) membrance properties to various CPAs at room temperature. These cell cryobiological properties assist the optimization of cryopreservation protocol of cells (T cells and macrophasges), which is improtant for studying mucosal immunity during HIV prevention trials.

2.1 Introduction

In HIV vaccine and microbicide trials, immune responses are typically evaluated in the peripheral blood, despite the most important immune responses being at the sites of viral entry, namely the genital and rectal mucosae. Sophisticated analyses of fresh mucosal cell and tissue samples are currently being done, but cryopreservation is little used [17–19]. Cryopreservation of mucosal specimens is critically important for immunological studies because it allows samples obtained at tdifferet times and trial sites to be preserved, shipped and stored for later analysis at a central laboratory. However, it is not clear whether the currently used cryopreservation strategies, which were originally developed for peripheral blood mononuclear cells (PBMC), are ideal for mucosal specimens. Publications reporting functional cell-based assays performed with cryopreserved mucosal specimens are limited and in consistent [20–23].

To optimized the cryopreservation of muosal cells, it is necessary to have a quantitative understanding of their biophysical response to the freezing process [3, 24, 25]. According to

Mazur's "Two-Factor Hypothesis", the cellular response to freezing is governed by intrisnsic properties fo the cells, including the portion of the cll volume that does not respond to osmotic pressure (V_b), the permeability of the cell membrane to water (L_p) and the permeability of the membrane to cryoprotective agents (CPAS; P_s) [26]. These properties are unknown for mucosal immune cells.

Our hypothesis is that understanding the fundamental cryobiological characteristics of mucosal immune cells will allow the development of an improved cryopreservation procedure. In the work, the cryobiuological properties of mucosal immune cells were determined using a microfluidic device developed in our group [27, 28]. Since the female genital tract is one of the most common sites of sexual HIV transmission, the cells assessed were isolated form the human vagina. Specificallym two cell populations that are central to adaptive cellular immunity and HIV susceptibility, T lymphocytes and macrophages, were isolated and their osmotically inactive cell volume (V_b), cell membrane permeability to water (L_p), and cell membrane permeability to CPAs (P_s) were determined. Four widely used CPAs - dimethyl sulfoxide (DMSO), glycerol, propylene glycol (PG) and ethylene glycol (EG) - were tested.

2.2 Materials and methods

2.2.1 Human vaginal mucosal specimens

Human vaginal tissues were obtained from healthy women undergoing vaginal repair surgeries in the Department of Obstetrics and Gynecology at the University of Washington. These tissues, which would otherwise have been discarded, were collected without any identifying patient information under a waiver of consent approved by the Institutional Review Boards of the University of Washington and the Fred Hutchinson Cancer Research Center.

2.2.2 Isolation and sorting of vaginal T cells and macrophages

Vaginal tissues were maintained in saline and on ice during transport and dissection. The stroma was removed from the epithelium, leaving epithelial pieces about 2 mm thick. These were subsequently cut into pieces of about 1 × 1*mm* and stored overnight in cell culture medium at 4 °C. The next morning, cells were isolated using an enzymatic digestion protocol [22]. Briefly, tissues were incubated in collagenase type II digestion medium (700 collagen units per mL; Sigma, St. Louis, MO) with 500-1000 units per mL DNase I (Sigma) at 37 °C with shaking for 30 min; tissues were disrupted by passage through a blunt needle and syringe, and the resulting cell suspensions were separated from undigested tissue pieces by filtration through a 70 mm strainer. Remaining tissue pieces were re-digested up to three additional times. Vaginal T cells and macrophages were purified from the bulk cell population by flow cytometric sorting, after staining with CD45 APC, CD3 FITC, and CD14 PE-Cy7 (all mouse anti-human from BD Biosciences, San Jose, CA, USA) and 0.1 mg/mL 40,6-diamidino-2-phenylindole (DAPI) for viability. All antibodies were titrated before use and used at the minimum saturating dose. Live $CD45^+CD3^+CD14^-$ and live $CD45^+CD3^-CD14^+$ events were sorted on a four laser BD FACSAria II (408, 488, 535, and 633 nm). The sorted cells ere suspended in 1×PBS at 10,000 cells/mL, stored at 4 °C, and used for the following experiments within 8 h.

2.2.3 The microfluidic perfusion system

Cell membrane permeabilities were measured with a microfluidic perfusion chamber we developed previously [27]. The microfluidic device was fabricated using soft lithography. The height of the microfluidic perfusion chamber was 15 μm to accommodate a monolayer of the expected cell sizes (8-12 μm). At the edge of the chamber, the channel height was shortened to 3 μm to trap the cells but still allow fluid to flow.

During experiments, the microfluidic device was immobilized on the stage of the microscopy (DM IRB, Leica, Buffalo Grove, IL). A droplet of cell suspension (10 μL) was added gently to the inlet reservoir. The fluid was withdrawn continuously by a digitally controlled syringe pump (PHD 2000 Infusion, Harvard Apparatus, Holliston, MA) with a flow rate of 40 $\mu L/h$ in order to stably trap cells in the chamber. After 10-15 cells were trapped and aligned in front of the block, 0.5 mL perfusion solution was added into the inlet

Table 2.1: Perfusion solutions and osmolalities.

Perfusion solutions	Osmolality (mOsm/kg-H_2O)
0.7×PBS	201
1×PBS	297
2×PBS	605
3×PBS	881
10% (v/v) DMSO in 0.9% NaCl	1823
1.5 M glycerol in 0.9% NaCl	1956
1.5 M ethylene glycol in 0.9% NaCl	1761
1.5 M propylene glycol in 0.9% NaCl	1575

reservoir, avoiding any violent perturbation to the fluid flow. The fluid was drawn into the chamber continuously by the syringe pump. The cell volume excursion history was recorded by a CCD camera (Phantom v310, Vision Research, Wayne, NJ) at 24 frames/ second until osmotic equilibrium was obtained, generally within 2 min. All the experiments were done at room temperature (22 °C).

In order to measure the osmotically inactive cell volume (V_b) and the cell membrane permeability to water (L_p), trapped cells were perfused with hypotonic and hypertonic saline solutions (0.7×PBS, 2×PBS and 3×PBS). To determine the cell membrane permeability to DMSO, glycerol, PG, and EG, dilutions of these chemicals were prepared in 0.9% NaCl saline solution. The osmolalities of the solutions were measured by an osmometer (Wescor Inc., Logan, UT) based on vapor pressure assessment (Table 2.1).

2.2.4 Image analysis

After video capture, the videos were converted to image frames using Cine Viewer software (Vision Research, Wayne, NJ). Cells were cropped from each frame of the image. The cropped images were enhanced and processed to find the cell boundary (see Fig. 1). In order to detect the cell boundary precisely, the Active Contour (dual-snake) algorithm was applied [29]. Thereafter, the two-dimensional cell area was evaluated by pixel counting and then converted to three-dimensional cell surface area and volume based on the assumption of spherical cell shape. All the image processing was performed with MATLAB software (MathWorks, Natick, MA).

In order to assess the hypothesis of spherical cell shape, the sphericity of T cells and macrophages (cell images at the beginning of each experiment) was evaluated, which was defined as $2\pi \cdot r_{equ}/p_{act}$. Here, r_{equ} is the equivalent cell radius calculated with the two-dimensional cell area based on image analysis, and pact is the actual cell perimeter.

2.2.5 Determination of cell membrane properties

Determination of osmotically inactive cell volume (V_b)

The Boyle van't Hoff relationship can be used to determine V_b, the osmotically inactive volume of the cell (μm^3). The osmotic response of the cell volume during hypertonic shrinkage and hypotonic expansion can be described as

$$V = \frac{C_0(V_0 - V_b)}{C_n^i} + V_b \tag{2.1}$$

where V (μm^3) is the cell volume when the intracellular osmolality is C_n^i (Osm/kg water), V_0 is the isotonic cell volume, C_0 is the isotonic osmolality, and V_b is the osmotically inactive cell volume.

Determination of cell membrane permeability to water (L_p) when no CPA exists

The membrane permeabilities to water (L_p) of Jurkat cell (immortalized line of human T lymphocyte cells) were determined by measuring cell volume shrinkage while cells were perfused by hypertonic 3× PBS solutions. The cell volume changes, i.e., water transport across the cell membrane, can be described as [27, 30, 31]

$$\frac{dV_C(t)}{dt} = L_p \cdot A \cdot (C_n^i - C_n^e) \cdot R \cdot T \tag{2.2}$$

where $V_c(t)$ is the cell volumes (μm^3) at time t (min); L_p is the cell membrane permeability to water ($\mu m/atm/min$; A is the cell membrane area (μm^2) and assumed as constant during perfusion ($= 4\pi r^2$ for a spherical cell shape); C_n^i, C_n^e are the intracellular and extracellular molalities (Osm/kg water), respectively; R is the universal gas constant (=0.008207 (atm L)/(mol K); and T is absolute temperature (in Kelvin). All the calculation was done under the assumption that the cells were spherical. The L_p was determined by least-squares curve fitting of the cell volume change data to the equation using MLAB (Civillized Software Inc., Silver Spring, MD).

Determination of cell membrane permeabilities to water (L_p) and CPA (P_S): two-parameter transport formalism

When permeant CPA (e.g. DMSO) and salts (e.g., NaCl) co-exist in a solution, the cell membrane permeability to water (L_p) and to the CPA (P_S) can be determined with a two-parameter transport model, where the cell volume change depends on both factors: [27,32–35]

$$\frac{dV_C(t)}{dt} = \frac{dV_S(t)}{dt} + L_p \cdot A \cdot (C^i - C^e) \cdot R \cdot T \tag{2.3}$$

where $V_C(t)$ and $V_S(t)$ are cell volume and intracellular CPA volume, respectively, at time t, and C^i, C^e are intra- and extracellular molalities (including both salts and CPA).

The CPA flux is given by

$$\frac{dN_S(t)}{dt} = P_S \cdot A \cdot (C_S^e - C_S^i) \tag{2.4}$$

where P_S is the cell membrane permeability to the CPA (cm/min); C_S^e and C_S^i are the extracellular and intracellular CPA molalities, respectively; and $N_S(t)$ is the mole of intracellular CPA at time t.

$N_S(t)$ and $V_S(t)$ are interchangeable by

$$N_S(t) = V_S(t)/\bar{V}_S \tag{2.5}$$

Here, $\bar{V}_S$ is the partial molar volume of the CPA.

The determination of L_p and P_S was done by least-squares curve fitting of the experimental data to the above two-parameter formalism using MLAB (Civilized Software Inc.)

2.2.6 CPA exposure tolerance

The CPA exposure tolerance of human vaginal T cells and macrophages to DMSO, EG and PG was tested. CPA solutions with different concentrations were prepared and precooled to 4 °C. 100 μL of each CPA solution was added dropwise to 100 μL cell suspension with agitation over 5 min. The final CPA concentrations ranged from 5% to 17.5% (v/v). After CPA addition, the cell suspension was kept at 4 °C for 10 min. Then, CPA was removed by adding 4 mL isotonic PBS dropwise with agitation at 4 °C over 5 min. The cells were collected by centrifugation at 300g for 10 min, and then tested for cell viability with flow cytometry

2.2.7 Statistical analysis

The number of data sets for the investigation of each cell property (e.g., the membrane permeability to DMSO for T cells) was 7-15 cells total per CPA and cell type from 4 donors. The statistical analysis was performed using the Student's t-test. The results are presented as mean standard deviation and a P-value less than 0.05 was considered statistically significant.

2.3 Results

2.3.1 Osmotically inactive cell volume V_b

The Boyle van't Hoff plots of human vaginal mucosal T cells and macrophages are shown in Fig. 2.1. The equilibrium cell volumes in hypotonic and hypertonic saline solutions (0.7×, 2× and 3× PBS) normalized to the cell volume in isotonic solution are plotted with respect to the reciprocal of the osmolality of the solution. The yintercept is the osmotically inactive cell volume fraction (V_b=V_0), i.e., the remaining cell volume when the osmolality approaches infinity. Results showed that the cell volumes in isosmotic solution (V_0) were 314.61 ± 36.45 μm^3 and 467.12 ± 32.71 μm^3 with diameters of 8.43 + 0.32 μm^3 and 9.62 ± 0.23 μm^3 for T cells and macrophages, respectively. The osmotically inactive volumes V_b of T cells and macrophages were determined to be 51.6% V_0 and 45.7% V_0, respectively.

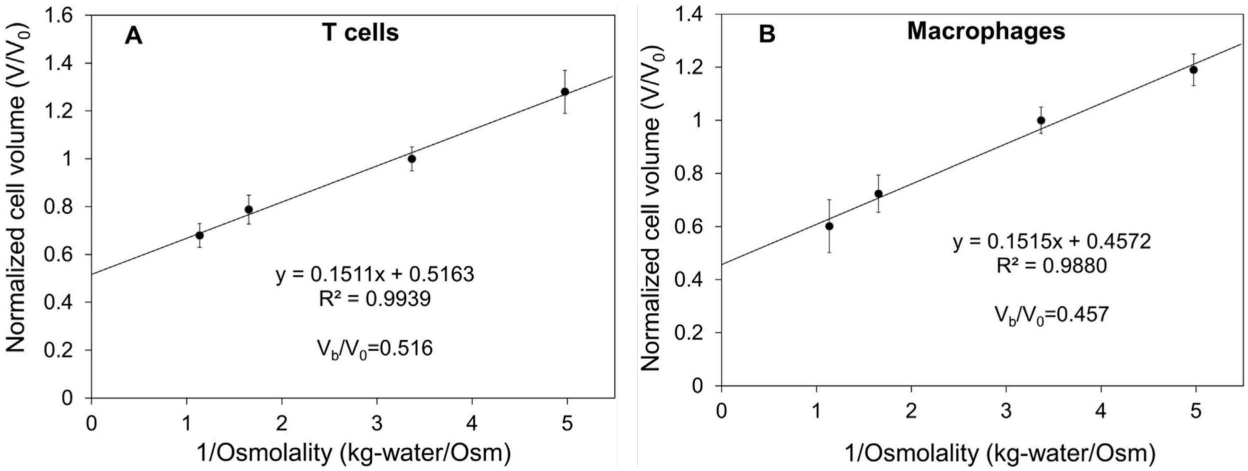

Figure 2.1: Determination of osmotically inactive cell volume V_b with linear curve fitting Boyle van't Hoff plots: x axis indicates the reciprocal of osmolality, y axis shows the equilibrium cell volumes normalized to the cell volume in isotonic solution. The data points used for linear curve fitting are the average of ten measurement results at corresponding concentrations. The obtained osmotically inactive cell volume V_b is 67.41 ± 4.07% V_0.

2.3.2 Cell membrane permeabilities to water (L_p) and cryoprotective agents (P_s)

Examples of the T cell volume excursion history when perfused by a hypertonic saline solution and a permeant CPA solution are shown in Fig. 2.2(a) and Fig. 2.2(b), respectively. The cell volume derived from the last of the 30 frames in each second was calculated and presented in the figures.

Fig. 2.2-a shows that when a cell is exposed to a hypertonic saline solution, its volume monotonically decreases and then reaches the final equilibrium value. Based on these data, the water transport ability, i.e., cell membrane permeability to water L_p, can be simulated. Fig. 2.2(b) shows the volume excursion of one cell perfused by 10% DMSO in 0.9% NaCl solution. The result shows that the cell shrinks first and then expands gradually back to a volume close to the original isotonic one. This phenomenon is caused by the transport of both water and permeant CPA. According to the cell volume excursion history, the cell membrane permeabilities to water and CPA can be calculated.

The cell membrane permeabilities to water (L_p) and CPA (P_s) were simulated by least-squares curve fitting using MLAB software. The results are shown in Table 2.2 and Table 2.3 for human vaginal mucosal T cells and macrophages, respectively. Lp values for T cells and macrophages were 0.196 ± 0.047 and 0.295 ± 0.069 mm/min/atm (mean ± standard deviation), respectively, when no CPA exists. If CPA and salts coexist in the solution, Lp values were reduced, especially for T cells (p ¡ 0.05). In order to test the assumption that cells are spherical, the sphericity of cells (the cell images at the beginning of each experiment) was evaluated. The sphericities were determined to be 0.91 0.04 (n = 45) for T cells, and 0.88 ± 0.04 (n = 48) for macrophages. The imperfect spherical cell shape may cause errors to the data analysis. However, quantitative evaluation of the effect of non-spherical cell shape on the results is complicated and out of the scope of this work.

Glycerol showed very low P_s values for both T cells ($0.005 \pm 0.004 \times 10^{-3}$ cm/min) and macrophages ($0.008 \pm 0.003 \times 10^{-3}$ cm/min). This was 52e146 times lower than the P_s values measured for the other three CPAs (p ¡ 0.05). For T cells, the P_s values for ethylene glycol,

Table 2.2: Membrane permeabilities of T cells to water and CPAs at room temperature (mean±standard deviation)

CPA	Cells	L_p (μm/min/atm)	P_S (10^{-3}cm/min)
PBS	14	0.196 ± 0.047	
DMSO	8	0.089 ± 0.051	0.472 ± 0.230
Propylene glycol	8	0.077 ± 0.054	0.635 ± 0.342
Ethylene glycol	7	0.099 ± 0.053	0.469 ± 0.175
Glycerol	8	0.055 ± 0.003	0.005 ± 0.004

Table 2.3: Membrane permeabilities of macrophages to water and CPAs at room temperature (mean±standard deviation)

CPA	Cells	L_p (μm/min/atm)	P_S (10^{-3}cm/min)
PBS	15	0.295 ± 0.069	
DMSO	9	0.234 ± 0.041	0.978 ± 0.313
Propylene glycol	9	0.221 ± 0.162	1.168 ± 0.484
Ethylene glycol	8	0.241 ± 0.094	0.418 ± 0.074
Glycerol	7	0.192 ± 0.072	0.008 ± 0.003

propylene glycol, and DMSO ranged between 0.469 and 0.635 × 10^{-3} cm/min, and there was no statistical evidence of a difference between them (p = 0.465-0.493). For macrophages, P_s to ethylene glycol (0.418 ± 0.074 × 10^{-3} cm/min) was in the same range as the P_s values for T cells, but P_s values for DMSO (0.978 ± 0.313 × 10^{-3} cm/ min) and propylene glycol (1.168 ± 0.484 × 10^{-3} cm/min) were significantly higher than the values for T cells (p ¡ 0.05).

2.3.3 CPA exposure tolerance

To determine the CPA exposure tolerance of mucosal cells, we added DMSO, EG, or PG at various concentrations dropwise to cell suspensions, incubated for 10 min on ice, and then

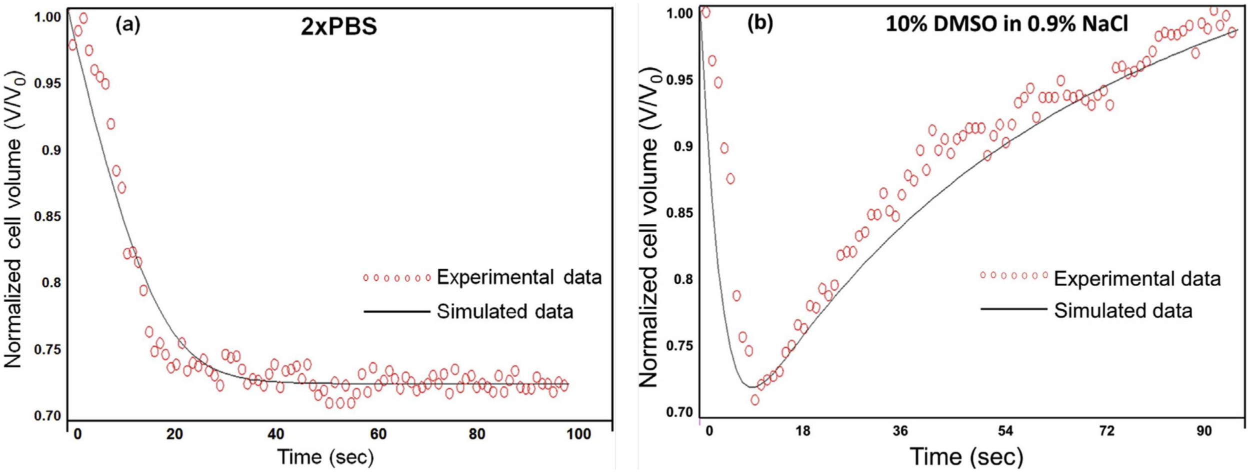

Figure 2.2: Cell volume excursion during perfusion by hypertonic solutions at room temperature:

dropwise diluted them out. We measured viability by cell type with flow cytometry, normalizing to the viability of untreated cells to have a consistent measure across samples. Fig. 2.3 shows the CPA exposure tolerance for human vaginal mucosal T cells and macrophages. The cell viability declined in a linear fashion as CPA concentrations increased. The relative viabilities remained above 90% up to concentrations of about 10% (v/v). DMSO had a more negative effect on T cell viability than the other two CPAs, while EG had a more negative effect on macrophage viability than the other two.

It is worth noting that three permeating CPAs (DMSO, EG and PG) were tested in the CPA exposure tolerance experiment due to their possible applications in the cryopreservation of mucosal cells. Osmotic tolerance limit (OTL) of the cell is another important cryobiological characteristic. For OTL test, cells are exposed to hypo- and hyperosmotic solutions with varying concentrations of non-permeating solute (e.g., NaCl), and then restored to osmotic conditions. Besides the cell viability, cell volume excursion data in this process are also valuable. The obtained cell shrinkage and swelling limits are useful to optimize the protocols of addition and removal of both permeating and non-permeating CPAs. OTL tests of mucosal cells will be done in the future.

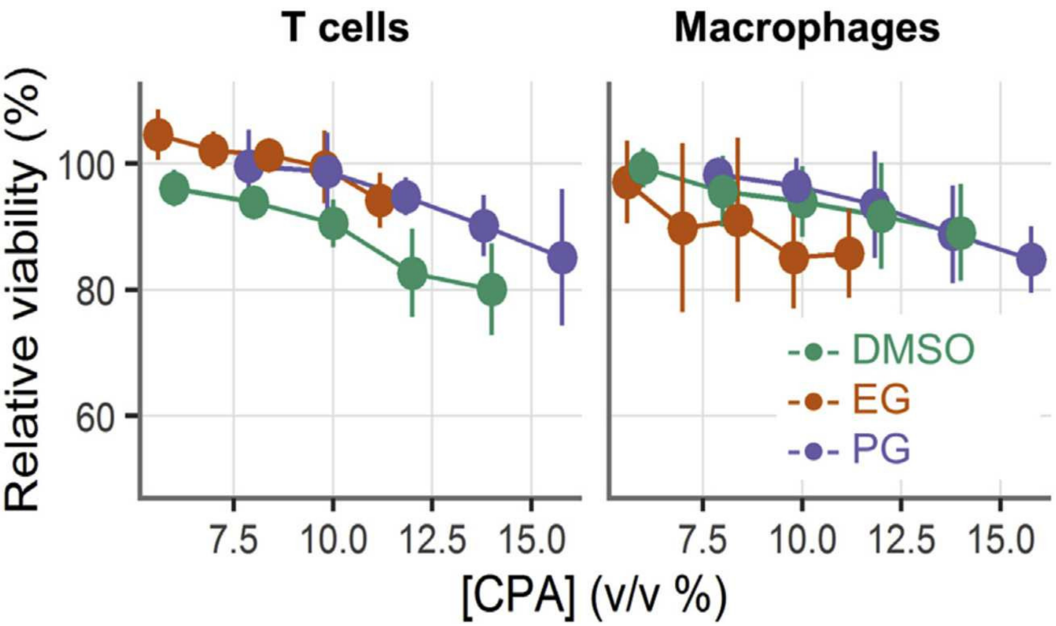

Figure 2.3: Cell volume excursion during perfusion by hypertonic solutions at room temperature:

2.4 Discussion

Cryopreservation of mucosal immune cells or tissues is essential to evaluate HIV vaccines and microbicides. However, there have been few reports of successful mucosal cryopreservation so far. We believe that this is due to a lack of knowledge about the cryobiological characteristics of such specimens. Based on Mazur's theory, freezing of living cells is a process of heat and mass transfer. The cell type-dependent optimal cryopreservation protocol is determined by the intrinsic biophysical properties of each cell type. Therefore, optimization of mucosal cell cryopreservation requires knowing the specimen's properties, such as the osmotically inactive cellular volume and cell membrane permeabilities to water and to CPAs.

In this chapter, a microfluidic perfusion channel was optimized and applied to measure the cryobiological properties of human vaginal T cells and macrophages. Table 2.2 and 2.3 shows the values of these properties for other cell types. It shows that human vaginal immune cells have lower L_p values than oocytes, prostate cancer cells, and megakaryocyte cells, and similar L_p values to those of pancreatic islets and dendritic cells. This suggests that CPA addition and removal should be relatively slow to decrease osmotic injury to mucosal immune cells. This might also indicate that water transfers relatively slowly across cell membranes when T cells and macrophages are frozen (measurement of L_p at subzero temperatures is needed to confirm this), and therefore mucosal immune cells should be frozen at a relatively low cooling rate. Results also showed that L_p values are reduced in the presence of CPA. Further cryopreservation experiments are necessary to optimize the protocol.

Among the four types of CPAs measured, glycerol had much lower permeability than the other three CPAs, for both T cells and macrophages. Therefore, glycerol can cause severe cell volume excursion and osmotic injury during CPA addition and removal, and is thus the worst option for vaginal immune cell cryopreservation. The Ps values for ethylene glycol, propylene glycol, and DMSO were similar for T cells, while for macrophages Ps to DMSO and propylene glycol was two to three times of that for ethylene glycol. For both T cells and macrophages, there was no significant difference between the Ps values for DMSO and propylene glycol. Tests of cytotoxicity and cryopreservation of mucosal immune cells had similar results for DMSO, ethylene glycol, and propylene glycol (separate manuscript in preparation). Therefore, these three CPAs are likely better options than glycerol for cryopreservation of mucosal T cells and macrophages. Currently, the cryopreservation protocol of human vaginal immune cells is generally adopted from that for peripheral blood mononuclear cell (PBMC), where 10% DMSO and cooling rate of 1 °C/min are applied. Our data necessitate further experimental trials with DMSO, ethylene glycol, propylene glycol, or cocktail of them.

The microfluidic perfusion method used here has some limitations. As a photomicrographic method, its measurement accuracy depends on the quality of captured images and accuracy of image processing, which is not yet optimal in current design. It is applicable to only spherical cells because that is assumed in the conversion from two-dimensional image to threedimensional volume. The measured result is not the average of many cells, but of a few individual cells. Moreover, to measure cell membrane properties at other supra-zero temperatures (e.g., 10 °C, 4 °C), a temperature controller is needed to be integrated with the microfluidic device, it cannot be applied at sub-zero temperatures due to liquid freezing in the channel.

2.5 Conclusions

In this chapter, a microfluidic perfusion channel was applied to measure the cryobiological characteristics of human vaginal mucosal T cells and macrophages at room temperature. The osmotically inactive volumes for T cell and macrophage are 0.516 V_0 and 0.457 V_0. Membrane permeabilities to water (L_p) at room temperature for T cells and macrophages are 0.196 and 0.295 μm/min/atm, respectively when no CPA exists in the solution. Among the four tested CPAs, DMSO, ethylene glycol, and propylene glycol have 50e150 times higher Ps values than glycerol. These three CPAs may be better CPA options to avoid severe cell volume excursion and osmotic injury during CPA addition/removal and cryopreservation. CPA exposure tolerance tests showed that the relative viabilities remained above 90% up to concentrations of about 10% (v/v). DMSO had a more negative effect on T cell viability than the other two CPAs, while EG had a more negative effect on macrophage viability than the other two.

Althrough a low cost and easy to operate tool the microfluidic perfusion chamber is, it has the following drawbacks: (1) Lack of local temperature control and monitoring mechanism; (2) The shadow from the block barrier causing errors to the cell volume calculation; (3) Trapped cell may move in large distance during the experiment, resulting in intensive labor during image processing. In order to overcome these drawbacks, a non-contact cell confinement and manipulation platform with local temperature control is proposed in the next chapter.

Chapter 3

DEVELOPMENT OF NON-CONTACT CELL CONFINEMENT AND MANIPULATION PLATFORM WITH LOCAL TEMPERATURE CONTROL

This chapter describes substrate architectures to construct an microfulidic device with instantaneous flow control capability, while being able to manipulate the localized temperature. In the chapter, the development, implementation and validation of the control system of the integrated microfluidic platform was addressed. To achieve the desired device features, a hardware system, with active Input/Output (I/O) communication, consisting of a compact DAQ for on chip gas pressure regulating, microcotroller and high sensitive power supply for heating control, and digital multimeter for sensor temperature reading, was implemented and tested. The real time morphology inside the device is monitored by a high speed camera. Two customized LabVIEW program were developed for a online image processing and inner data manipulation for the whole control system, as a result achieving the demanded control features. Furthermore, multiphysics simulation is counducted to evaluate the temperature uniformity of two types (centered and distributed) of heater design.

3.1 Introduction

Microfluidics is the science and technology of systems that manipulate small (picoliters to microliters) quantities of fluids, with the device characteristic length scales ranging from tens to hundreds of micrometers. [36] Microfluidics has emerged as a versatile method of handling fluids at small length-scales, with advantages in low reagent cost, high resolution and sensitivity, fast prototyping, short analysis time, and a well controlled microenvironment in concentration, pH, and temperature [37–42]. In particular, microfluidics has been employed to generate double emulsion droplets, [43] Janus particles, [44] enhanced mixing, [45] cell encapsulations, [46] focusing and sorting cells and particles, [47] and stretching DNA and deformable cells at cross-slot microchannels [48, 49]. Among them, precise trapping and manipulation of suspended objects in fluids (e.g., particles, long chain molecules, drops and cells), is challenging but particularly useful for operations such as flow cytometry, cell-on-chip, [50–52] microfluidic crystallization, [42] and isolation of rare cells from solutions. Simultaneous control of flow and temperature on a single device is more difficult to achieve, yet critical for a wide range of applications such as polymerase chain reaction (PCR) [53, 54] and chemical reactions. [53, 55, 56]

3.1.1 Flow control

Various passive methods to manipulate objects in microfluidics have been reported, such as inertial migration, [57] pinched flow fractionation (PFF), [58] deterministic lateral displacement, [59] and hydrodynamic chromatography. [60] These methods are limited to the high-throughput focusing and sorting, but lack of precise trapping of the objects at a specific zone. Alternatively, several active strategies have been explored for trapping and manipulating suspended objects in fluids, by applying external driving forces such as acoustic, [61, 62] optical, [63] electrophoretic, [64] magnetic, [65] and hydrodynamic [66] techniques. Each active manipulation method has its own limitations. For example, the acoustic and magnetic methods are limited by their fabrication techniques to scale down the device; the electrophoretic method requires an ionic working fluid since it uses a charged interface between the particle surface and surrounding fluid; the optical method generates limited force range (0.1∼100 pN), which is only suitable to manipulate nano or sub-micron scale objects. The hydrodynamic method offers several advantages for trapping and manipulating single objects with high spatial resolution on chip without the need for additional external fields. Moreover, this method gives nonperturbative observation and analysis of single objects in a solution, which offers the possibility for easy trapping, real time analysis and visualization, easy integration with additional microenvironment control systems. [67]

Hydrodynamic trapping of suspended objects in fluids was first demonstrated by Taylor in 1934, [68] which was known as "four-roll mill" method. For decades, researchers have improved the original method to extend its ability for multiple types of fluid flows. [69–72] Recent efforts focused more on integrating computer based feedback control with the microfluidic chip, aiming to provide controllability and fine tuning of micron objects under extensional flows. [73–75] Especially, controlled pneumatic technique by regulating force field is a well known method for the non-contact trapping of isolated targets. The pneumatic valve is referred to as the Quake's valve [76], which involves multilayered soft lithography (MSL). The liquid flows in the bottom layer (fluid layer) of the device, while the upper layer (control layer) pushes down the thin membrane polydimethhlsiloxane (PDMS) in the bottom layer by regulating the pressure inside the control layer. Based on this operating principle, components such as on-off valves, switching valves, metering valves, mixers and pumps can be designed in the microfluidic device for versatile flow control. [77] Furthermore, by carefully regulating the air pressure in the control layer, small objects (e.g. particles, cells, and long chain molecules) can be trapped hydrodynamically at the stagnation point created by an extensional flow. [78] Utilizing similar flow control techniques, cell/particle sorting [79] and further cell/particle manipulation [80, 81] by the hydrodynamic force can be achieved.

3.1.2 Temperature control

Since temperature variations significantly affect the intrinsic properties of fluids, on-chip temperature control is necessary for stable operations inside microfluidic devices. Existing global temperature control methods either preheat the carrying fluid [82] inside the device, or use a printed wiring board (PWB) heating unit under the entire microfluidic device [83]. Localized temperature control methods have used either micropatterning wire on silicon [55, 84, 85] or micropatterning wire on glass [86–89] embedded in the device. While precise temperature control can be accomplished by using global temperature control for devices on the order of $\sim$ 10 mm, it is challenging to achieve precise localized temperature control in a small and confined area ($\sim 10\ \mu\mathrm{m}^2$). Furthermore, the global temperature control usually measures the temperature outside the microchannel by using a thermocouple and utilizes a Peltier element to manipulate the temperature stage, leading to inaccurate temperature measurement inside the microchannel and causing slow cooling and heating at a rate around 10 °C/min, with temperature stability in the range of 1 °C. [90] As thermo-responsive physical phenomenon have drawn much attention in applications such as the stimuli of thermoresponsive polymers, [91] biological membrane response to temperature, [92] polymerase chain reaction (PCR), [53, 54] and chemical reactions occuring at micron scales [53, 55, 56]. Microfabrication technology has enabled advances in accurate temperature control and manipulation inside microchannels with temperature ramp rates ranging from 0.1 to 20 °C per second and constant temperature gradients along the direction of the channel width from 6 to 40 °C/mm, [93] which allows more accurate investigations of thermal effects in microfluidic experiments.

3.1.3 Integrated control features

Although controlling individual microenvironment parameters has shown promising success, managing multiple microenvironment parameters with isolated targets (e.g., trapping target particles while manipulating the pH or temperature simultaneously), is still challenging. Commercial temperature stages have been coupled with flow control devices to control millimeter sized heating zones, but not for localized micron size features. [90] Progresses in simultaneous localized flow and temperature control on a single chip can provide unique opportunities to improve our understanding of fundamental fluid mechanics and biomechanics problems, such as transient interfacial dynamics between partially miscible fluids, and measurement of instantaneous cell stiffness in-situ.

Taking steps forward to design an integrated microfluidic platform with both flow and temperature control features, we construct and report a specific microfluidic platform which consists of a flow-focusing channel for the generation of emulsion droplets and subsequent trapping in a cross junction, pressure control, and localized temperature control to demonstrate the working principle of our platform, with the goal of (1) trapping and manipulating of isolated targets by a precise pressure feedback control, (2) thermal management at the specific zone by a temperature feedback control, and (3) real time image processing and analysis for tracking the location and observing the morphological change of the isolated objects.

This charpter is organized as follows. Section 2 provides fabrication procedures of the microfluidic device, schematics of the control system, information of the hardware used for on-chip feedback control. Section 3 introduces specific design criteria of the integrated platform involving both flow and localized temperature control. Section 4 showcases the device performance criteria *e.g.*, condition and stability of droplet generation and trapping, precision and accuracy of temperature control, and discusses factors affecting the control performances, followed by a validation experiment with aqueous glycerol and liquid crystal to demonstrate the working principle of the integrated microfluidic platform. Section 5 summarizes the features of our integrated microfluidic platform, with an outlook and potential applications.

3.2 Materials and methods

3.2.1 Device fabrication

The device fabrication consists of several core steps below: conductive wire patterning on glass slides, double-layered PDMS microfluidic channel fabrication, and the device assembly (Fig. 3.1a).

Conductive wire patterning

A glass slide (EMF, CA-134) with a 1000 Å thick gold film on a 50 Å thick chrome adhesion layer was used for conductive wire patterning. The slide was spincoated with a positive photoresist with thickness ~ 1.5 μm (Microchem, AZ-1512), followed by a soft baking process at 110 °C for 2 min. The microheater and the adjacent temperature sensor were designed by AutoCAD and printed on a transparency with 50,800 dpi resolution (Fineline Imaging, OR). The exposure process was carried out by using a mask aligner (ABM-aligner, ABM-USA Inc.) under wavelength of 365 μm for 5–6 sec. The photoresist was then developed by using 25 % v/v aqueous photoresist solution (Microchem, AZ-340) for 1 min. The glass slide with the patterned photoresist was baked at 110 °C for 1 hr for better adhesion and curing. A wet etching process was conducted by immersing the glass slide into gold etchant (TFA gold etchant, Transene) for 30–35 sec, followed by immersing the glass slide immediately in chrome etchant (TFE chromium etchant, Transene) for 2–3 sec. The glass slide was rinsed by acetone to remove residual photoresist. The etched glass slide was again rinsed with isopropanol (IPA) and water, and dried by nitrogen gas. The glass slide, together with the electric connection pads covered by Teflon tape, was coated with 100 nm silicon dioxide to prevent any electrolysis.

Double layered microchannel fabrication

The microfluidic channel was fabricated using standard multilayer soft-lithography (MSL). [76] Photomasks were designed using AutoCAD and printed on a transparency with 50,800 dpi resolution using commercial laser photoplotting service (Fineline Imaging, OR). The masters were fabricated by contact photolithography using a negative photoresist (SU-8 2050, Microchem). The photoresist was spincoated onto a plasma-cleaned 100 mm silicon wafer (test grade wafer, SVM). After a soft baking process at 65 °C for 3 min then at 95 °C for 9 min, an exposure process was carried out by using a mask aligner (ABM-USA Inc., ABM-aligner) with a 365 μm wavelength UV light for 22 sec. After post baking (2 min at 65 °C, 7 min at 95 °C), the master was then developed with a propylene glycol monomethyl ether acetate (PGMEA) (Y020100, Microchem), followed by surface treatment with trichloro (1H, 1H, 2H, 2H-perfluorooctyl) silane (448931, Sigma-Aldrich) vapor under a vacuum condition for easy peeling of PDMS replica from the master.

Two SU-8 masters of fluidic layer (70 μm deep) and control layer (70 μm deep) were fabricated. The fluid layer with a thin PDMS valve membrane was obtained by spincoating the fluidic SU-8 master with PDMS (Sylgard 184, Dow Corning) at 15:1 ratio of the base resin and the crosslinker. The control layer was fabricated by casting PDMS at 5:1 ratio of base resin and crosslinker onto the corresponding SU-8 master. Both PDMS layers were partially cured by baking at 65 °C for 25 min. The thick PDMS replica (control layer) was then peeled off from the master, aligned, and was hermetically sealed onto the thin PDMS layer (fluidic layer). The bonded PDMS double-layer was placed on a hot plate at 65 °C for 4 hr to form an integrated monolithic device. Verified by the microscopy image, the double-layered microchannel has a 17.5 μm thin PDMS valve membrane, 70 μm control layer, and 70 μm fluid layer (Fig. 3.1b).

3.2.2 Control systems

Simultaneous on-chip flow and temperature control is accomplished by employing a custom designed LabVIEW virtual interface that communicates with a gas regulator, temperature controller, and a digital multimeter (Fig. 3.2). The pressure regulation of pneumatic valves was achieved by using a gas regulator (Proportion-Air, QPV1), whose output has the maximum pressure of 150 psi with ±0.1% of setting output pressure accuracy. The output of the gas regulator was connected to the inlet port of the upper layer (control layer) in the device, when pressurized, deforming the elastomeric membrane in the the bottom layer (fluid layer) of the device, decreasing the cross section area of the fluidic channel. The pressure difference will be identical in every case. The gas regulator changes the flow resistance in one of the outlet channels, leading to a control of the flow rates in both channels, redistributing the planar extensional flow pattern, thus relocating the stagnation point position at the cross junction. Through active feedback control of the droplet position using the valve pressure, droplets can be trapped in the velocity potential well, created by actively manipulating the stagnation point of the extensional flow at the cross junction. A multifunction data acquisition module (National Instruments, PCI 6229) with a connection terminal (National Instruments, BNC 2110) is used as digital Input/Output (I/O) for the feedback control of the gas regulator. A high precision programmable power supply (BK Precision, 9124) is used as a power source for the microheater. A MOSFET switch module, controlled by the pulse width modulation

(PWM) signal from a microcontroller board (Arduino, UNO-R3), was used for the fine control over the heating power of the microheater. A digital multimeter (Keithley, 2700 with 1300 switch module) was used to measure the real time resistance of the temperature sensor, which can be converted to the temperature reading by the resistance-temperature relation obtained from the temperature sensor calibration. Syringe pumps (Cetoni, neMESYS Base 120) were used to pump fluids inside the microfluidic channel. The microfluidic chip was placed on an inverted microscope (Nikon, Eclipse Ti-U). Images were recorded by a high speed camera (Phantom vision research, M310) with the resolution of 256 by 320 pixels, 8-bit depth (256 gray levels), while having a real time image processing rate at 30 frames per second (fps) and up to 1,000 fps acquisition rate for transient phenomenon studies.

3.3 Design criteria of integrated platform

In this section, we show the rationale of design criteria of the integrated platform for both flow and localized temperature control. A specific integrated platform is developed to accomplish the following tasks on a single chip: generate size-specific emulsion droplets with the flow focusing geometry, hydrodynamically deliver and trap one droplet at the stagnation zone of the cross-junction by modulating the cross section area of the microchannel with active feedback control. Once the droplet trapping is achieved, the temperature is locally mediated on chip with a localized microheater, controlled by a temperature controller. Upon initiating data acquisition, the morphological change of the droplet and the temperature profile can be recorded in real time at the specific region of interest. The schematics of this microfluidic platform is illustrated in Fig. 3.3. The microfluidic channel (Fig. 3.3) consists of two core regions: flow focusing region (Fig. 3.3c-1) for emulsion droplet generation, and the cross-slot junction (Fig. 3.3c-2) in the center of the platform for droplet trapping. Furthermore, a conductive circular patterned wire (Fig. 3.3c-2), acting as a localized microheater and temperature sensor, is placed in the center of the cross junction region for precise temperature control of the trapped droplet.

3.3.1 Integrated flow control

The integrated platform has two patterned PDMS layers, a thin fluidic layer forming passage way for fluid flow and a thick layer containing two pneumatic valves. The fluidic layer (Fig. 3.3a, highlighted in red) has three inlets, two for the continuous phase and one for the dispersed phase, with a flow focusing junction (Fig. 3.3a, box in cyan) for droplets generation, and a cross-slot junction (Fig. 3.3a, box in black) for subsequent droplet trapping. The inlet streams flow, from each half, in opposing direction towards the cross-slot junction, converge, then exit via two outlets (O_1 and O_2 in Fig. 3.3a). The control layer has two dead-end channels sitting perpendicular to the fluidic channel, forming the pneumatic channels with elastomeric membrane valves. By regulating the pressure inside a pneumatic channel of the control layer, the cross section area of fluidic channel underneath can be modulated, leading to changes in the fluidic resistance at the valve section.

Emulsion droplet generation

The formation of uniform sized emulsion droplets is enabled by using a flow-focusing design. The microfluidic channel consists of two inlets, labeled as (1) for the continuous phase and (2) for the dispersed phase (Fig. 3.3a). The continuous and dispersed phases flow from both sides to the cross-junction. By controlling the flow rate ratio between the two phases, dispersed phase droplets with uniform sizes are continuously generated. The orifice of the flow-focusing channel is 75 μm and 100 μm in width and height, respectively.

Droplet trapping

Once the emulsion droplets are produced, they flow towards the cross junction area and the flow bifurcates from the cross-junction to the two outlets. The width and height of the cross-junction are 350 μm and 232 μm. Gas regulators control the fluid resistance in the fluidic channel by regulating the pressure inside the control channel. A syringe pump introduces fluid flow inside the fluidic channel. Two pneumatic valves with 500 μm in width are located at the horizontal and perpendicular direction of the microchannel labeled as V_x and V_y. These valves can be controlled by gas regulators that control the pressure in the control channels to block the cross-section of the microchannels. This modulates the fluid resistance inside the fluidic channels, manipulating the position of the stagnation point along the x- and y-directions.

Flow control

The control program for the hydrodynamic trapping of particles was first developed by Tanyeri et. al. [78] by using LabVIEW. We built upon their program with our customized hardware setup. We also optimized the algorithm for real-time image processing of trapped droplets at the cross-junction to remove the optical background introduced by the micro-heater and the temperature sensor embedded in the device.

A region of interest (ROI) was defined at the center of the cross-junction to establish a set point and spatial limits for real-time image processing within the field of view. The center of the ROI (x_t, y_t) corresponds to the user-defined trapping position of the droplet. The real-time images could be adjusted by controlling the threshold of the image to enhance the image contrast and identify the edge of the droplet. The pre-processed images were then converted into binary images after implementing a series of morphology processing with a built-in particle analysis function in LabVIEW (more details about real time image processing is available in SI). The center of the droplet (x_c, y_c) obtained by the image analysis was considered as the current position of the droplet. The trapping error was defined as $e_x = x_c - x_t$ and $e_y = y_c - y_t$ along the x- and y-direction. Once the droplet was trapped in the ROI, the controller automatically compensated the trapping error with a customized proportional control algorithm.

3.3.2 Localized temperature control

The microheater (Fig. 3.3c-2, highlighted in gold) is designed in a zigzag pattern with a circular heating zone for efficient heating, with the dimension ~ 20 μm, 900 μm, and 200 μm in width, length, and diameter, respectively. The temperature sensor is etched adjacent to the microheater on chip (Fig. 3.3c-2, highlighted in orange), with feature dimensions approximately $\sim 20\ \mu$m, 430 μm, and 20 μm in width, length, and gap from the microheater, respectively. The circular geometry of the microheater is important, as it allows the access for droplet edge detection in real time image processing. These heater and sensor geometries also enable good heating uniformity and precise localized temperature sensing in application scenarios with circular object. [94]

The sensing of the temperature change is achieved by measuring the change of resistance in the sensor as the microheater heats up the fluid and glass substrate first, with the temperature change of the fluid and glass substrate altering the resistance on the temperature sensor. Thus, monitoring and manipulating the temperature in a local region as small as hundreds of μm is possible with our active feedback control procedure. We developed the virtual instrument operation interface by LabVIEW for the monitoring and manipulation of localized temperature, achieving an active feedback control between the microheater and the temperature sensor. A temperature setpoint was defined by user as the set temperature (T_s). The current temperature (T_c) was obtained by transferring sensor resistance to real time temperature reading, using the temperature calibration curve (see subsection below). The temperature error was defined as $e_T = T_c - T_s$, which is compensated to converge to zero via a built-in proportional-integral-derivative (PID) control algorithm.

Temperature sensor calibration

The underlying mechanism of temperature measurement in the temperature sensor rests upon the temperature dependency of the electrical conductivity of the wire. Thus, it is important to calibrate the temperature sensor to obtain a reliable and precise temperature. A PDMS slab with a reservoir, holding calibration fluid, was placed on the glass slide etched with the microheater and temperature sensor. A J-type thermocouple (Omega, SA1-J) was placed into the reservoir as the temperature reference. The temperature sensor was connected to one channel of the digital multimeter for 4-wire resistance measurement, while the thermocouple was connected to the other channel for the temperature reading (Fig. 3.4a). The reservoir was then filled with hot water, the calibration fluid, while measuring both the temperature and sensor resistance simultaneously. A series of resistance data which corresponds to the temperature ranging from room temperature to 60 °C was collected to obtain a linear curve fit that was used as a general calibration curve between the sensor resistance and real temperature. This calibration curve was implemented into the temperature control algorithm in the LabVIEW code. Once the calibration is finished, the PDMS slab was removed from the glass slide, and the double-layered microfluidic channel was bonded with the glass slide. Inlet and outlet tubings were then connected to the device (Fig. 3.4b) for further experiments.

3.3.3 Heater pattern design and temperature distribusion simulation

To examine the spacial temperature profile created by on-chip microheater with different shapes, we conducted multiphysics simulation (COMSOL 5.2) of laminar flow conjugated heat transfer, coupled with Joule heating. The heat transfer in solid and fluid is governed by

$$\rho C_p \frac{\partial T}{\partial t} = \nabla \cdot (k \nabla T) + Q \tag{3.1}$$

$$\rho C_p \frac{\partial T}{\partial t} + \rho C_p \mathbf{u} \cdot \nabla T = \alpha_p T \left(\frac{\partial p_{\mathrm{A}}}{\partial t} + \mathbf{u} \cdot \nabla p_{\mathrm{A}} \right) + \nabla \cdot (k \nabla T) + Q \tag{3.2}$$

respectively, where ρ, C_p, T, t, $\mathbf{u}$, α_p, p_{A}, k and Q are the density, specific heat, temperature, time, fluid velocity, thermal expansion coefficient, pressure, thermal conductivity and heat source. The heat source produced inside the microheater is given by $Q_J = J \cdot E = \sigma (\nabla V)^2$, where $J = \sigma E$ is the current density, $E = -\nabla V$ is the electric field, and σ is the electrical conductivity of the microheater. Q_J acts as a boundary heat flux for both the heat transfer in solid and the heat transfer in fluid. The convective heat flux $q_0'' = h\left(T_{ext} - T\right)$ is applied to the bottom of glass slide.

The boundary and initial conditions of the multiphysics simulation are showen in Fig. 3.5.

3.4 Results and discussions

3.4.1 Droplet trapping performance

Even though trapping solid particles such as polystyrene beads and cells are already reported, it is more challenging to trap emulsion droplets due to the following reasons. First, the size of the droplet produced at the flow-focusing device (on the order of tens to hundreds of microns) is comparatively larger than that of a polystyrene bead for trapping purposes. In addition, the density of certain liquids (i.e., liquid crystal) can be 30 % higher than that of polystyrene, thus the larger mass and hence inertia from the droplet can lead to difficulty when trapping the droplet using the pressure difference with the pneumatic valve. Second, the droplet trapping involves liquid/liquid interfaces between the two liquid phases, which introduces additional instability to the system. Due to these difficulties, the following issues should be resolved to achieve successful droplet trapping: (1) establishing the optimal droplet generation conditions at the flow-focusing region, and (2) stablizing the trapped droplet with respect to flowing liquids. In the following two subsections, we demonstrate the influence of droplet generation conditions and flow rate conditions on the droplet trapping performance.

Influence from droplet generation

To explore the influence of droplet generation conditions on the trapping performance, we used oleic acid with a small amount of Span 80 (0.1 wt%) as the continuous phase, and 50 wt% aqueous glycerol solution as the dispersed phase in the microfluidic channel. Flow rates are varied from 8 $\mu l/hr$ to 1000 $\mu l/hr$ to produce the aqueous droplet with varying sizes. The droplet generation occurs either in the dripping regime or the jetting regime. [95, 96] The dripping regime occurs at relatively low flow rates and is characterized by the periodic formation of highly uniform spherical droplets. Due to the competition between the viscous and capillary forces, the dispersed phase breaks into discrete droplets periodically under certain flow rate ratios. The droplet production is mainly governed by the flow rate ratio, viscosity ratio, and the capillary number ($Ca = \eta_0 V_0/\sigma_i$), where η_0 is the dynamic zero shear viscosity of the continuous phase, V_0 is the average velocity of the continuous phase at the orifice, and σ_i is the interfacial tension between the dispersed and continuous phases. Generally, droplet diameters are proportional to the ratio between the interfacial tension and the viscous force exerted from the continuous phase. [97, 98] With increasing flow rates of both phases, the dripping regime gives way to a jetting regime, which features a long jet that stretches downstream (Fig. 3.6b4). Jetting is a consequence of the increased flow rates that force the filament to travel at a greater rate. Unlike in the dripping regime, droplets do not form at the orifice, but instead form at the tip of the jet farther downstream. In general, the length of the jet will increase with increasing flow rates of both phases. Meanwhile, the jet becomes quite thick and produces larger droplets than in the dripping regime. We show that it is possible to generate droplets as small as 10 μm – 30 μm in diameter. However, the distance between these traveling droplets becomes much shorter, which causes obstacles in trapping droplets at the cross-junction due to drop–drop interaction.

Flow rate effects

The hydrodynamic trapping relies on the extensional flow at the cross-junction to balance againist the Brownian motion and flow fluctuations, by applying appropriate pressure using pneumatic valves to confine the objects close to the stagnation point. Planar extensional flow is generated in the cross-junction channel by introducing two laminar streams, which can create a stagnation point at the center of the cross-junction region. The stagnation point is a semi-stable point, whose velocity potential can be expressed as:

$$\varphi = \left(\frac{\dot{\varepsilon}}{2}\right)\left(x^2 - y^2\right), \tag{3.3}$$

where $\dot{\varepsilon}$ is the strain rate (s^{-1}), x and y are the spatial coordinates with respect to the stagnation point along the inlet and outlet. Equation (1) entails that the stagnation point is a semi-stable point (saddle point). In principle, using the feedback control system, the stability of the stagnation point can be actively controlled to some extent, conserving a potential well for the steady hydrodynamic trapping. [67]

To trap larger objects at the cross-junction, one can either increase the proportional control gain (K_p) from the LabVIEW code or increase the flow rate of the fluid. However, both strategies have their limitations. The control signal output for pneumatic valve regulation is proportional to the proportional control gain (K_p), correlated with the trapping error. For larger K_p, the controller is prompted to eliminate the error by adjusting the fluid resistence of the outflowing stream, as a result, moving the stagnation point corresponding to modified extensional flow at the cross junction. Large K_p may lead to sufficient disturbances in the extensional flow to prevent droplet trapping. Increasing the flow rate of the fluid provides larger driving force by generating sharper velocity potential distributions, which requires higher image resolution and short feedback cycle to achieve steady trapping. The working principle to strike a fine balance between K_p and flow rates is illustrated in Fig. 3.7 A. Fig. 3.7 A (a–h) shows a series of histograms of the trapping error along the Y direction with flow rates ranging from 65–290 μ l/hr. With perfect trapping, the error distribution should form a sharp peak around Y=0. When the trapping becomes unstable, the trapping errors exhibit a wide distribution with a flat peak. Fig. 3.7 A shows that the droplet trapping becomes unstable when the flow rate exceeds 240 μ l/hr. Moreover, the deformation of the droplet becomes more significant as the flow rate increases, see Fig. 3.7 B. These results demonstrate that the steady hydrodynamic trapping for droplets is possible by creating a potential well using the extensional flow and regulation of the pressure by the pneumatic valve.

3.4.2 Localized temperature control performance

To evaluate the localized temperature control performance, we ran an aqueous glycerol solution (65 wt%) through the device and set the temperature to 35 °C. After the temperature was stabilized, we maintained the temperature at 35 °C for 2 min, while acquiring localized temperature sensing data. Figure 7 shows the results. The temperature varied as little as ±0.25°C with a low relative standard deviation (σ = 0.083 °C).

3.4.3 Design validation experiment

To demonstrate the capabilities of our integrated microfluidic platform with both flow and temperature control, we selected a thermotropic liquid crystal (LC), 4-Cyano-4'-pentylbiphenyl (5CB) as the droplet phase for the proof of concept studies since 5CB undergoes rapid and reversible nematic-to-isotropic transition at approximately 35°C. [99] An aqueous glycerol solution (65 wt%) with 3.5 mM of the surfactant Sodium dodecyl sulfate (SDS) was used as the continuous phase. The flow rates of the continuous and dispersed phases were initially adjusted to be 200 μL/hr and 10 μL/hr to generate uniform sized LC droplets with a diameter around 110 μm at the flow-focusing junction, at room temperature (Fig. 3.9a).

Once nematic LC droplets were generated at the flow-focusing region, they continued to flow towards the cross junction zone, with the flow rate of the LC phase being reduced to zero to avoid possible coalescence between the trapped LC droplet and flowing LC droplets. The on-chip pneumatic valve was used to regulate the relative flow resistance in the outlet streams, which enables fine control of the position of the stagnation point for easier trapping. At the cross-junction of the microchannel, the nematic LC droplet with diameter of 110 μm was successfully recognized and trapped (Fig. 3.10a), by employing real time image processing using built-in edge detection and particle analysis algorithm (see SI video). A region of interest (ROI) within the imaging window was defined to establish a set point and spatial limits for real-time image processing within the field of view. In this experiment, an initial pressure of the pneumatic valve was set to 1 psi which was regulated via the LabVIEW GUI. The trapped nematic LC droplet was confined in the ROI within the tolerance of $\pm 3\mu$m using a proportional controller (Kp=-0.01).

Upon trapping, the temperature of the microheater underneath the trapped LC droplet was increased from room temperature to 35 °C, with the aid of the temperature controller. A polarized optical microscope was used to capture the nematic-to-isotropic transition of the LC droplet with localized temperature variations (Fig. 3.10). The LC droplet exhibited the nematic state initially at room temperature, and started the transition into the isotropic state at 21.67 sec as the temperature reached around 33 °C. The LC droplet became transparent at 59.58 sec as the temperature reached 35 °C, indicating the complete nematic-to-isotropic transition of the LC droplet. This process is reversible and our experiments show reproducibility.

3.4.4 Multiphysics simulation results

Fig. 3.11 shows the results from multiphyscis simulation. Fig. 3.11(a) to (c) shows the results of centered heater design; while 3.11(d) to (f) indicate the results of distributed heater design. Fig. 3.11(a,d,) and (b,e) demonstrate the spacial temperature distribution and spacial temperature gradient distribution, respectively. Fig. 3.11 (c,f) plot the 1 dimension temperature variaion along the center line of trapping region (marked in red dashed line in Fig. 3.11 a and d), respectively.

From Fig. 3.11, when maintaining the trapping region at around 37 to 42 °C of both heater design, the distributed heater design provides a better temperature uniformity of less than 0.03 °C temperature difference at the center of the trapping region, compared to 1.4 °C temperature difference of centered heater design.

3.5 Conclusions and perspective

In this chapter, an integrated microfulidic platform was developed, which consists of a flow-focusing channel for the generation of emulsion droplets, with instantaneous flow and localized temperature control. A double-layered microfluidic channel was fabricated, and integrated with the microheater and temperature sensor to control the flow and temperature simultaneously. Both flow and temperature were manipulated by the LabVIEW with active feedback control. In particular, we used thermotropic liquid crystal (LC) as the droplet phase to demonstrate the temperature control capacity of our integrated microfluidic platform as a proof-of-concept experiment. The liquid crystal droplet was successfully trapped at the cross-junction of the channel with a pneumatic valve regulated by LabVIEW feedback control with the proportional air pump. The temperature was mediated by the microheater and the temperature sensor underneath the LC droplet by the LabVIEW feedback control with multiple hardware Inputs/Outputs (I/O). The LC droplet exhibited its nematic-to-isotropic transition with increasing temperature. The temperature variation was found to be as small as ±0.25°C with a relatively low standard deviation, which guarantees precise control of the temperature within a local region.

Our integrated microfluidic platform offers great potentials to provide direct real-time flow and temperature control that is critical to characterize transient interfacial dynamics in miscible jets and pendant drops, and in the dissolution of sessile drops, relevant to numerous technological processes, ranging from cleansing operations where liquid soaps are rinsed from surfaces, to the dissolution of mucous in the intestinal tract.

Another potential area of applications involves biotechnology such as droplet based rapid PCR and on-chip cellular physiology studies. Although techniques for high throughput on-chip cell culture and monitoring are available, [50–52] developing solutions that offer the possibility of isolating and monitoring single cells, while manipulating multiple variables of a localized microenvironment is still challenging. Our microfluidic platform, with instantaneous flow and localized temperature control features, shows great advantages in providing flexible and accessible solutions. Our proof-of-concept studies with LC droplets demonstrated the capability to trap isolated micron size target while manipulating localized temperature environment precisely with high sensitivity and quick response (15 °C/min with both ramp-up and cool-down cycles, with temperature overshoot less than 2 %). With proper modification of this original design, we envision a similar microfluidic platform can be designed to switch the fluidic environment to study isolated single cells [100].

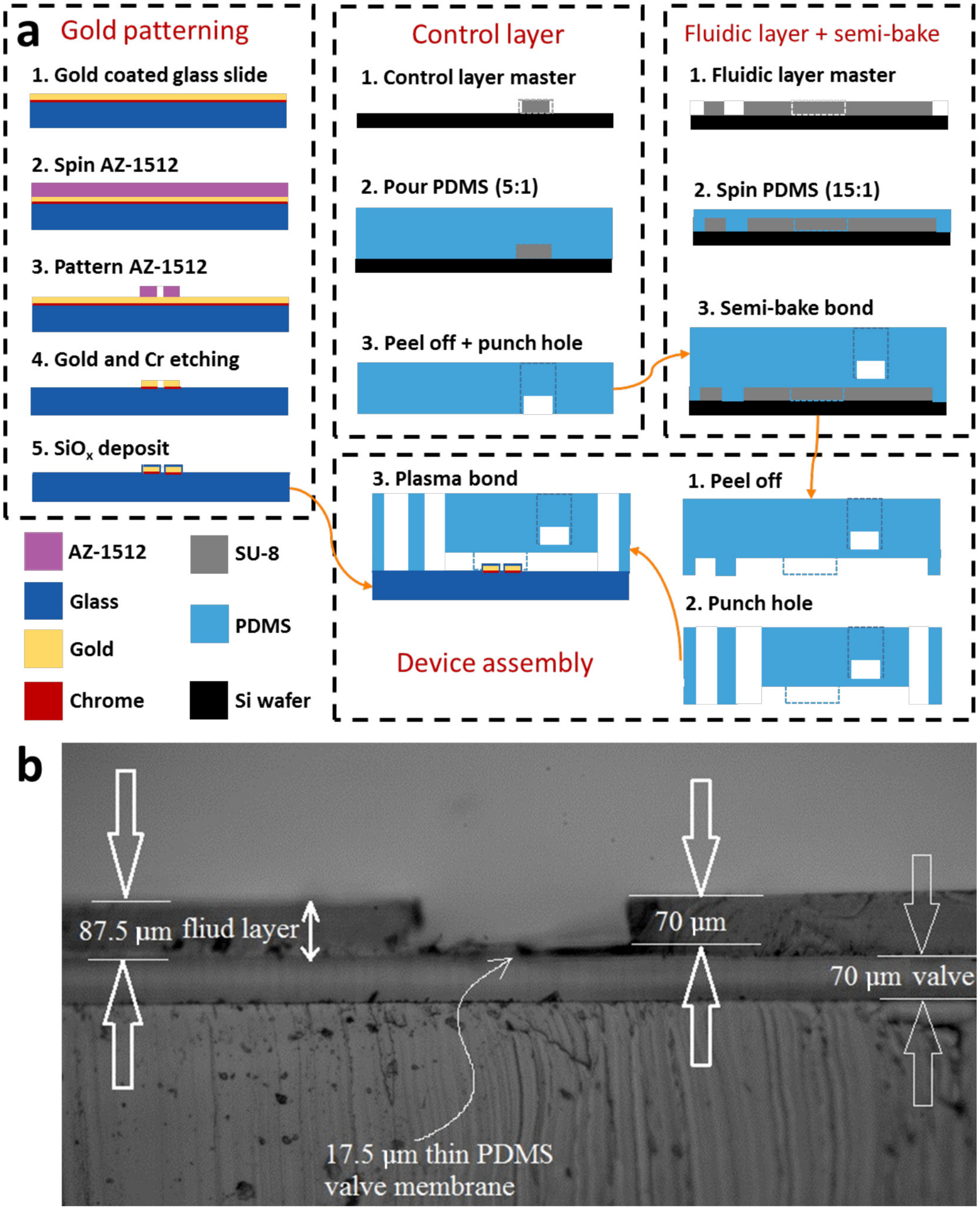

Figure 3.1: Device fabrication and characterizations: (a) Step-by-step procedures of conductive patterning, double-layered PDMS channel fabrication, and device assembling; (b) Optical microscopy image of the cross section of the double-layered PDMS.

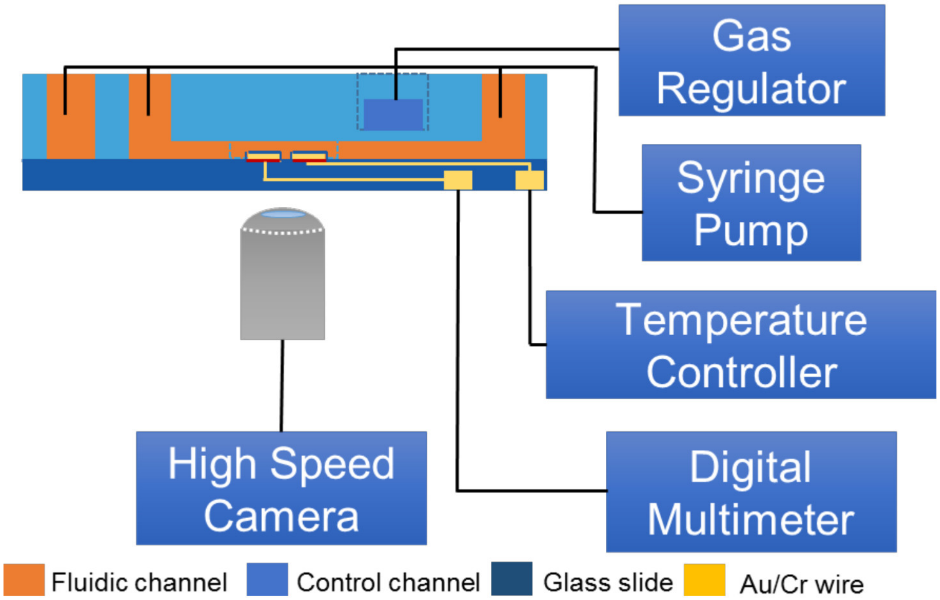

Figure 3.2: Schematics of flow and temperature control systems in the microfluidic platform: A gas regulator controls the fluid resistance in the fluidic channel by regulating the pressure inside the control channel. A syringe pump introduces fluid flow inside the fluidic channel. A temperature controller and a digital multimeter are connected to the micropatterned wires (Gold/Chrome). The microfluidic platform is placed on an inverted microscope equipped by a high speed camera (Phantom Miro 310, vision research). The entire system is remotely controlled by a custom designed LabVIEW virtual interface.

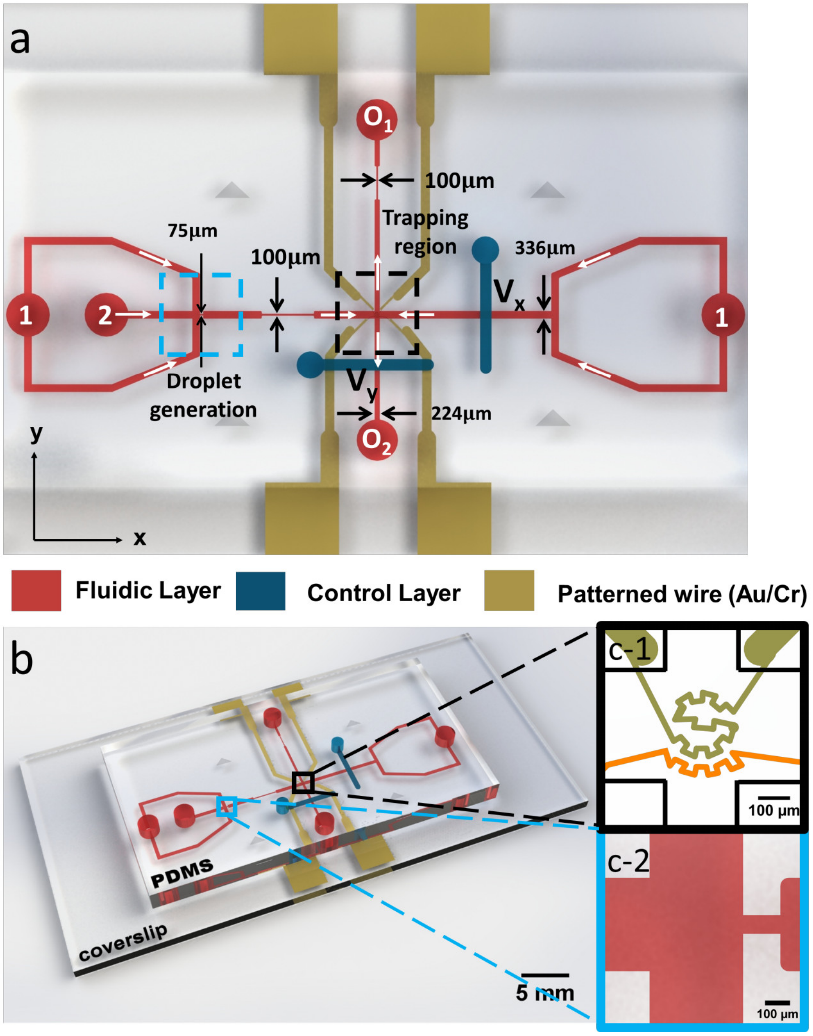

Figure 3.3: Integrated microfluidic platform for both flow and localized temperature control: (a) plane view of the microfluidic device. The continuous and dispersed phases are introduced through inlet (1) inlet and (2), respectively. Emulsion droplets are generated at the flow-focusing region (cyan box), which are then delivered and selectively trapped at the cross-slot junction (black box). After converging at the cross-slot junction, the fluids exit through outlet O_1 and outlet O_2. (b) 3D rendering illustration of the microfluidic device, showing the glass slide etched with gold wires (microheater in the black box region), double-layered PDMS with microchannels in a fluidic layer (in red), and the control layer for pressure manipulation (in blue). (c) Enlarged view of the boxed regions showing: c-1 flow-focusing region, and c-2 microheater (gold) and temperature sensor (orange) at the cross-slot junction.

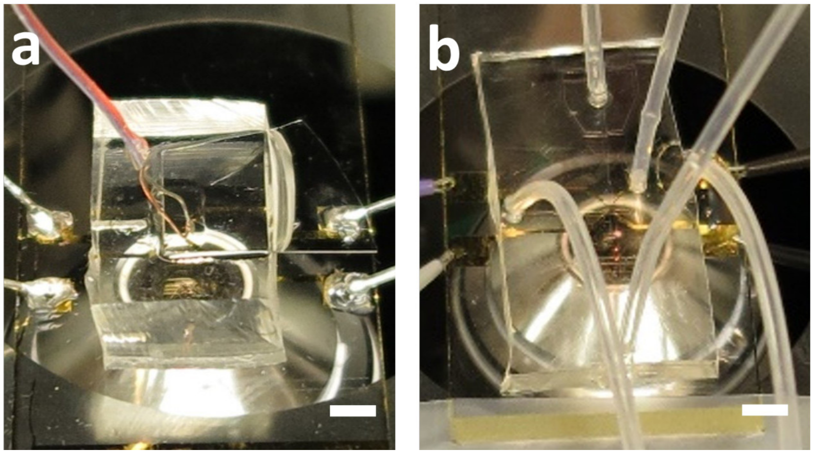

Figure 3.4: Snap shots of the microfluidic device (scale bar = 5 mm) for (a) Temperature sensor calibration. The temperature sensor is connected to one channel of the digital multimeter while J-type thermocouple is connected to the other channel of the digital multimeter. (b) Double-layered microfluidic device with inlet and outlet tubings sitting onto an inverted microscope. Wires from the microheater and temperature sensor are connected to the temperature controller and the multimeter, respectively.

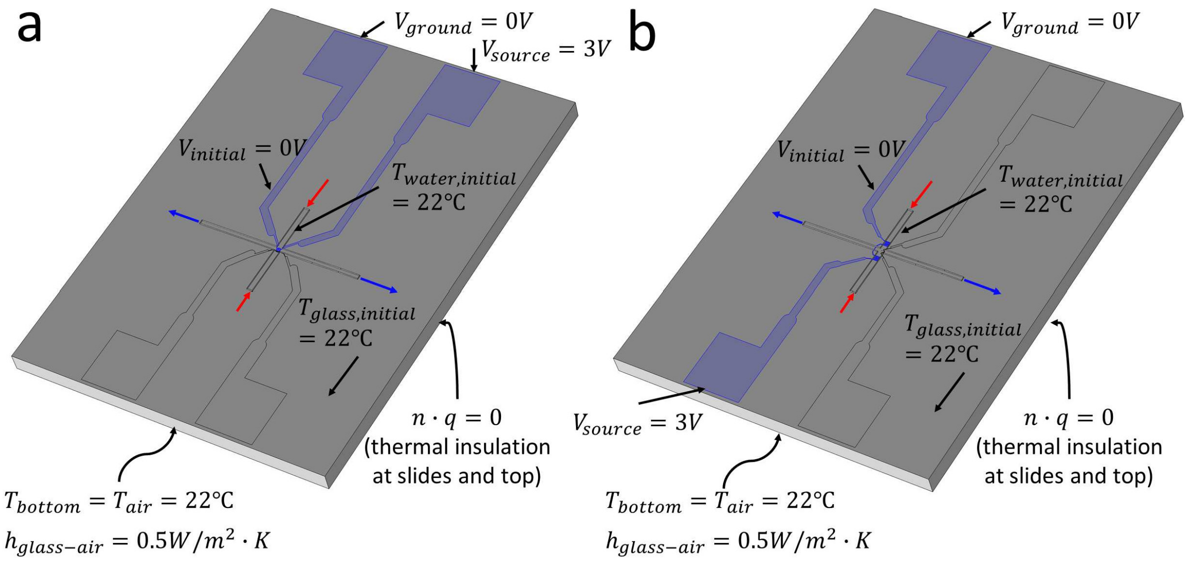

Figure 3.5: Boundary of initial conditions of multiphysics simulation of centered heater design (a) and distributed heater design (b), where the part marked as blue indicateds the wire of microheater, the red arrows implies the flow inlets and the blue arrows implies the flow outlest.

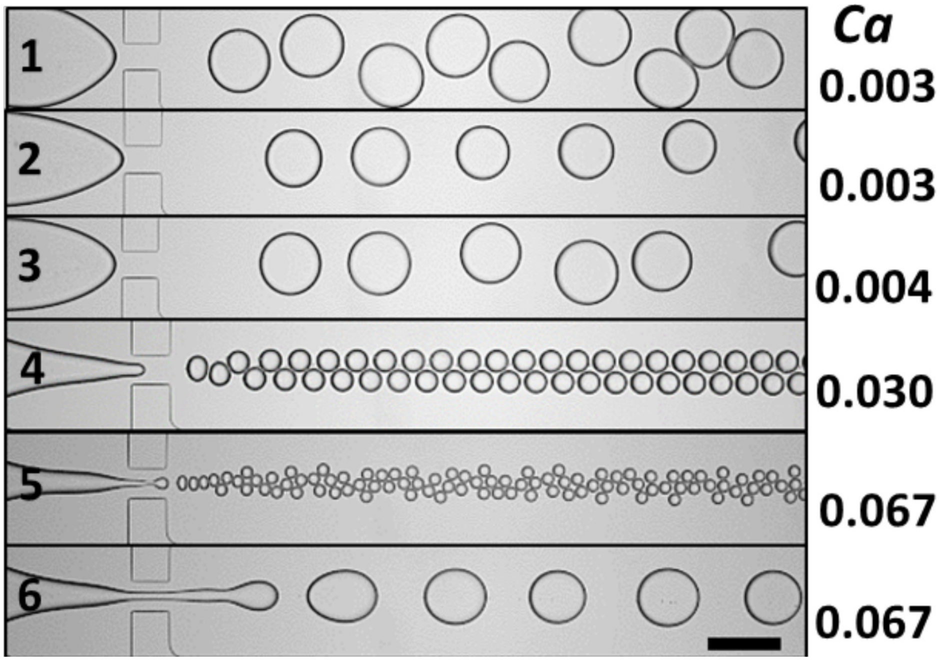

Figure 3.6: Droplet production with varying flow rates: Oleic acid droplet produced at aqueous glycerol solution with varying flow rates ratio (dispensed phase/continuous phase) (1) 0.16, (2) 0.8, (3) 0.667, (4) 0.11, (5) 0.1 (6) 0.2. Scale bars are 200 μm

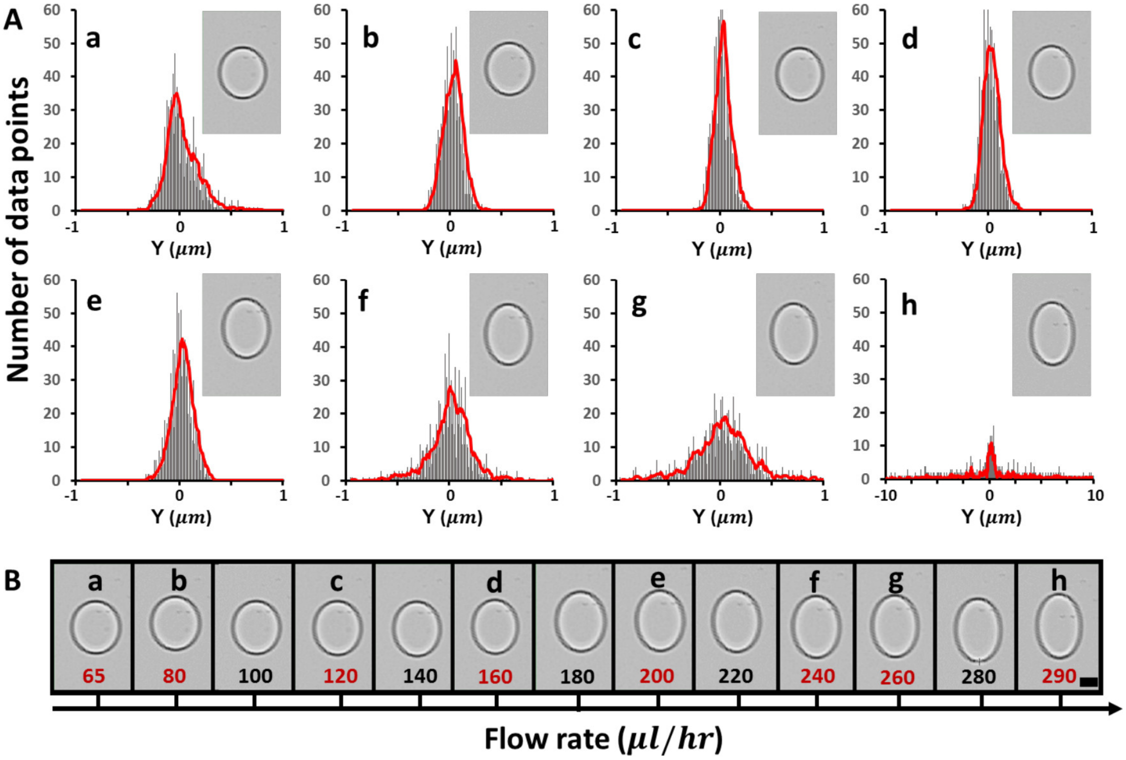

Figure 3.7: Influence of the flow rate to droplet trapping and morphology: (A) The histogram of droplet trapping error along the Y direction at selected continuous phase flow rates; (B) Microscopy images exhibiting droplet deformation under different flow rates. Scale bar is 50 μm.

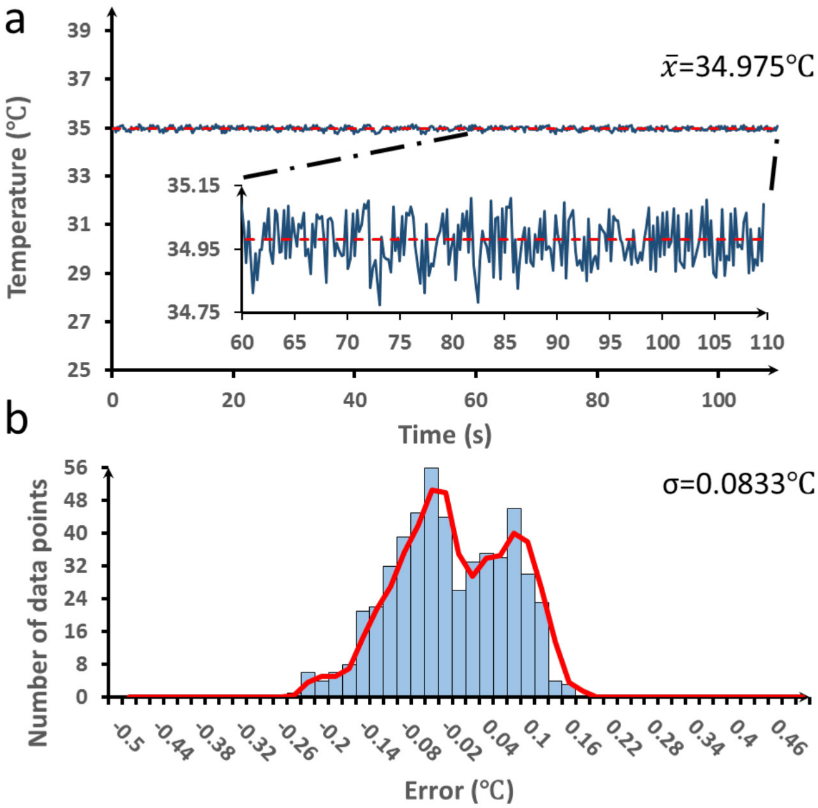

Figure 3.8: Temperature control performance: (a) The temperature variation evaluation of the temperature control, when setting the target temperature at 35°C for 2 min. The variation is within ±0.25°C. $\bar{x}$ is the mean value of the temperature obtained; (b) Histogram of localized temperature control error. The error is defined as $T_c - T_s$. σ stands for the relative standard deviation of the error.

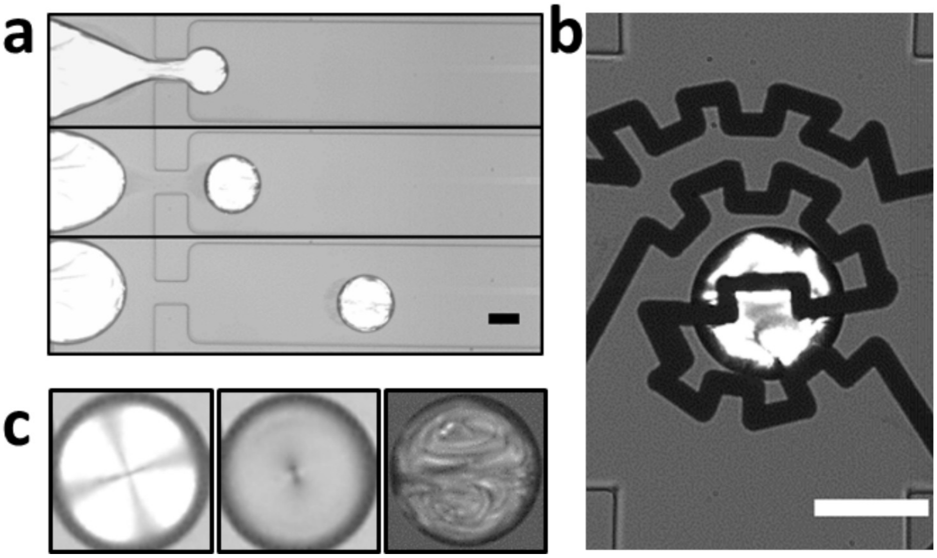

Figure 3.9: Liquid crystal droplet generation and trapping: (a) image sequences showing liquid crystal droplet generation under polarized light. Scale bar is 100 μm; (b) liquid crystal droplet trapped at the cross junction. Scale bar is 100 μm; (c) Microscopy images showing morphology of liquid crystal droplet under polarized light at rest (left), under unpolarized light at rest (middle), and under polarized light of a moving droplet (right).

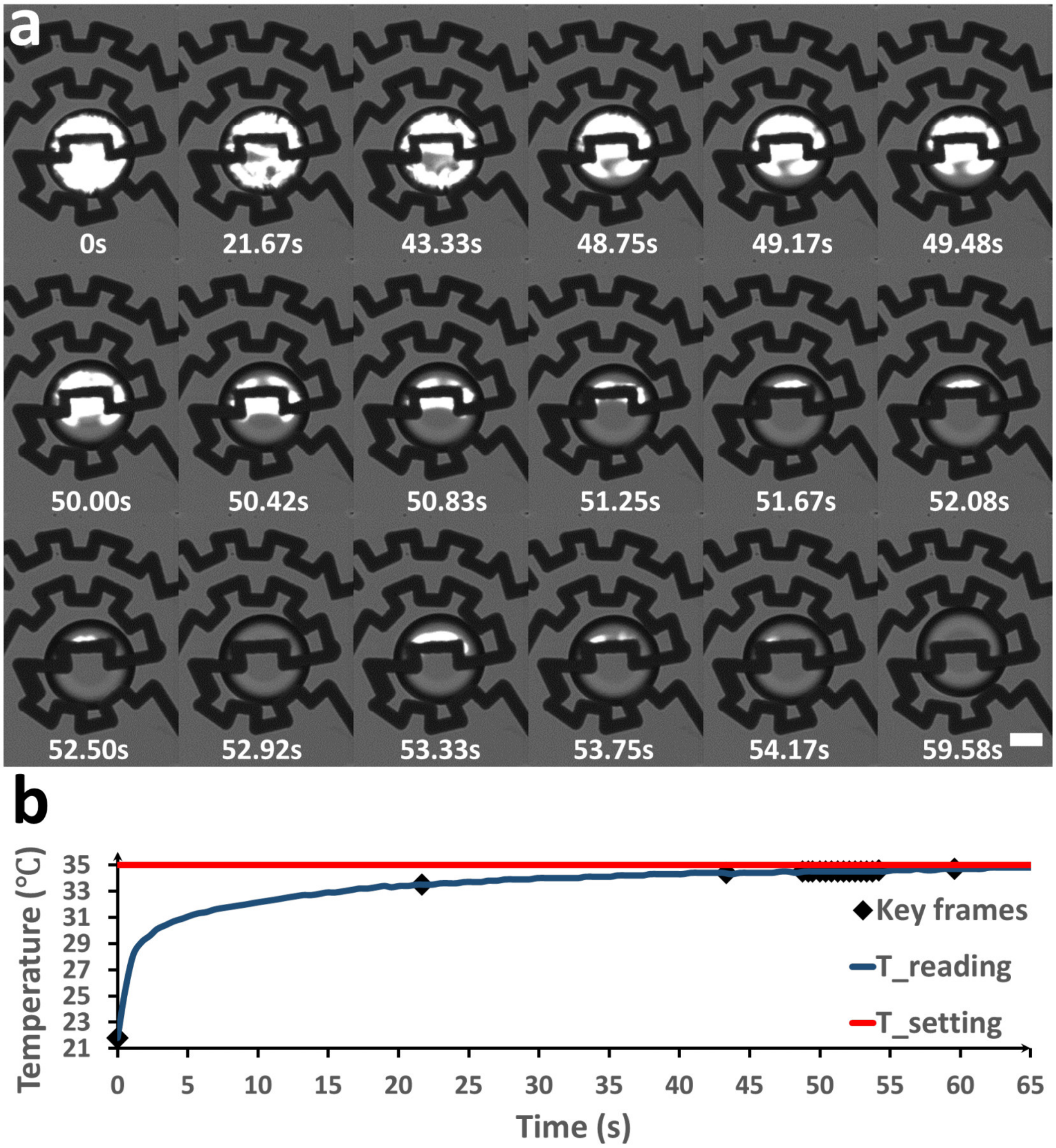

Figure 3.10: Nematic-to-isotropic transition of LC droplet with localized temperature control: (a) the LC droplet (edge highlighted in red) shows nematic-to-isotropic transition with increasing temperature (correlated with elapsed time), with the scale bar= 50 μm. (b) The temperature profile obtained by the temperature sensor, corresponding to captured key frames.

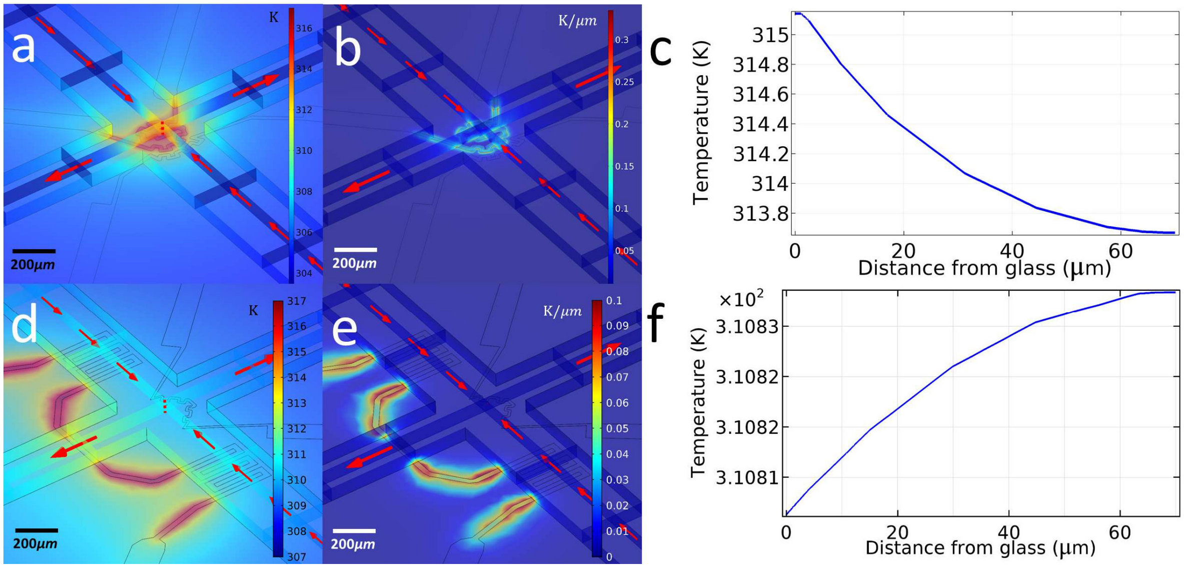

Figure 3.11: Multiphysics simulation results representing the spacial temperature profile: spacial temperature distribution of centered (a) and distribution (d) heater design; spacial temperature gradient distribution of centered (b) and distribution (e) heater design; temperature variation along the center line of trapping region (marked in red dashed line in (a,d) of centered (c) and distributed (f) heater design

Chapter 4

DETERMINATION OF CELL MEMBRANE PROPERTIES AT VARIOUS STATIC TEMPERATURES WITH CELL CONFINEMENT AND MANIPULATION PLATFORM

This chapter moves one step forward to apply the developed cell confinement and manipulation platform to the determination of cell membrane properties, using human acute lymphoblastic leukemia cells (Jurkat, Clone E6-1) as model cell. The membrane transport properties of Jurkat cells was measured, including the osmotically inactive cell volume (V_b) and cell membrane permeabilities to water (L_p) and to cryoprotective agent (CPA) solutions (dimethyl sulfoxide (DMSO) in this study) (P_s) at various temperatures (room temperature, 30°C, and 37°C). Such characteristics of cells are of great importance in many applications, especially in optimal cryopreservation. With the results, the corresponding activation energy for water and CPA transport was calculated. The comparison of the results from the current study with reference data indicates that the developed platform is a reliable tool for emperature-dependent cell behavior study, which provides valuable tools for general cell manipulation applications with precise temperature control.

4.1 Introduction

Cryopreservation suspends the clock of a biomaterial by freezing it and resumes the clock by thawing it back to normal physiological temperature. Since sperm was successfully preserved in 1949 [5], cryopreservation has been widely explored and applied for the long-term storage of DNA/RNA, proteins, biofluids, cells, tissues and organs, meeting the needs of many fields from fundamental research to clinical applications, like cell/tissue banking, diseases study, vaccine and drug development. The key factors behind cryopreservation are the addition of cryoprotective agent (CPA) before the freezing process, removal of CPA after thawing, and the cooling/rewarming rate during the freezing/thawing process, in which cells experience series of highly anisotonic conditions, causing injury [24]. According to Mazur's "Two-Factor Hypothesis" [3], a cell's behavior during freezing varies between different cell types, which is governed by the intrinsic cryobiological properties of various cell types, including the osmotically inactive cell volume (V_b), the permeability of cell membrane to water (L_p), and the permeability of the membrane to CPAs (P_s) [26]. Furthermore,the transport coefficients, e.g. L_p, P_s, are temperature dependent, the relation of which is governed by Arrhenius equations and influenced by the activation energy (E_a). It is necessary to obtain knowledge of cryobiological characteristics of cells to optimize the cryopreservation procedures for different cell types. To obtain these intrinsic cell properties reliably and efficiently, devices that are able to track cells while, at the same time, manipulating the extracellular environment (such as temperature and the composition of the extracellular medium) are required.

Various devices, which were extensively reviewed by McGrath [31], have been developed to quantify the cell membrane transport properties with the help of new techniques, such as nuclear magnetic resonance [101], "stop flow" [102], electron paramagnetic resonance [103], electronic sizing [104–106], and phase contract microscopy [30, 107–109]. Of these methods, phase contrast microscopy is the only one that has been used to determine membrane transport properties by investigating either a large cell population or a single cell. This technique can be used to directly observe, trace, and analyze the volume changes of individual cells in anisotonic environments.

Gao et al. [30] presented a microperfusion chamber capable of manipulating multiple or single cells, and different cell types (e.g. mouse oocytes and golden hamster pancreatic islet cells). Chen et al. [27] also developed a microperfusion chamber that allows for passively trapping cells with straight channel and lowered PDMS ceiling in the middle of channel. In those designs, cells are immobilized with physical barrier of either porous membrane or blocks of PDMS and are perfused instantaneously by target solution. This method avoids mathematical complexity while still being applicable to various cell types and testing conditions, but it requires proper pore size and density of customized membrane depending on different cell types, which adds complexity to device fabrication.

Microfluidics have great advantages in investigating biosystems in highly quantitative manner, e.g. in vitro quantitative cellular analyses [110], quantitative biomolecular analysis [111], and quantitative systems biology study [112]. Recent advances in microfabrication and microscopy further enable the real-time monitoring of the activity of biosystems with single cell precision, enabling studies of gene expression [113] ,chemotaxis, enzymatic activity using chemical cytometry [114, 115], and cell sorting [116–118]. Though various cell manipulation techniques have been developed, certain design restrictions arise depending on specific application scenarios. In a word, there is still a crucial need of improved techniques for single cell analysis in order to provide new information on cell dynamic response.

Current microfluidic-based approaches for single cell analysis can be classified into two categories according to their trapping features: contact based passive trapping and non-contact based active trapping. Contact based trapping includes barrier hydrodynamics and chemical-gel matrices [119–121]. The former uses physical barrier to block cells while letting fluid to pass by, and the later integrates this idea into matrices to achieve high throughput cell trapping, which has advantage of trapping multiple cells while lacks of precise control of individual cells for long time.

Alternatively, several non-contact based strategies have been explored for trapping and manipulating suspended objects in fluids, by applying external driving forces such as acoustic [61, 62], optical [63], electrophoretic [64], magnetic [65], and hydrodynamic [66, 67, 78, 100, 122–124] techniques. Each active manipulation method has its own limitations. For example, the acoustic and magnetic methods are limited by the difficulty to scale down the device due to their fabrication techniques. The electrophoretic method requires an ionic working fluid since it uses a charged interface between the particle surface and the surrounding fluid. The optical method generates limited force range (0.1∼100 pN), which is only suitable to manipulate objects in nano or sub-micron scale. Research also shows that long time optical exposure can cause damage to proteins on cell membrane, which makes optical method not suit for long term manipulation of cells [125].

Comparatively, the hydrodynamic method offers several advantages for trapping and manipulating single objects with high spatial resolution without the need of additional external fields. Hydrodynamic trapping force scales linearly with the particle radius, which enables easy confinement of small target particles [122]. Moreover, this method gives nonpertubative observation and analysis of single objects in a solution, which offers the possibility for easy trapping, real time visualization and analysis, and easy integration with additional microenvironment control systems (e.g., temperature).

Since temperature variations significantly affect the intrinsic properties of fluids and cells, on-chip temperature control is necessary for stable operations inside microfluidic devices. Existing global temperature control methods either preheat the carrying fluid [82] inside the device, or use a printed wiring board (PWB) heating unit under the entire microfluidic device [83]. Localized temperature control methods have used either micropatterning wire on silicon [55, 84, 85] or glass [86–89] embedded in the device. While precise temperature control can be accomplished by using global temperature control for devices on the order of ~ 10 mm, it is still challenging to achieve precise localized temperature control in a small and confined area ($\sim 10\ \mu\text{m}^2$). Furthermore, global temperature control usually measures the temperature outside the microchannel by using a thermocouple and utilizes a Peltier element to manipulate the temperature stage, leading to inaccurate temperature measurement inside the microchannel and causing slow cooling and heating at a rate around 10 °C/min, with temperature stability in the range of 1 °C [90] .As thermo-responsive physical phenomena have drawn much attention in applications such as the stimuli of thermo-responsive polymers [91], biological membrane response to temperature [92], polymerase chain reaction (PCR) [53, 54] ,and chemical reactions occurring at micron scales [53,55,56]. Microfabrication technology has enabled advances in accurate temperature control and manipulation inside microchannels with temperature ramp rates ranging from 0.1 to 20 °C per second and constant temperature gradients along the direction of the channel width from 6 to 40 °C/mm [93], which allows more accurate investigations of thermal effects in microfluidic experiments.

Although controlling individual microenvironment parameters has shown promising success, managing multiple microenvironment parameters with isolated targets (e.g., trapping target suspended object while manipulating the pH or temperature simultaneously), is still challenging. Commercial temperature stages have been coupled with flow control devices to control millimeter sized heating zones, but not for localized micron size features [90]. Progress in simultaneous and localized flow and temperature control on a single chip can provide unique opportunities to improve our understanding of fundamental fluid mechanics and biomechanics problems, such as transient interfacial dynamics between partially miscible fluids, and measurement of instantaneous cell stiffness in-situ. Overall, an integrated microfluidic platform that can trap cells, and exchange extracellular media at long time scales, while being able to monitor and control the local temperature around the cell is still unavailable and in critical need.

As a step towards an integrated microfluidic platform with both flow and temperature control features, we constructed a specific microfluidic platform which achieves (1) non-contact trapping and manipulating of isolated targets by a precise feedback control in pressure; (2) rapid and steadily changing extracelluar media; (3) thermal management at the specific zone by a temperature feedback control, and (4) real time image processing and analysis for tracking the location and observing the morphological change of the isolated objects. To demonstrate the working principle of our platform, we further conducted cell membrane transport property measurements using the Jurkat cell line.

4.2 Materials and methods

4.2.1 Source and preparation of cell suspensions

Human acute lymphoblastic leukemia (ALL) cells (Jurkat, Clone E6-1) [126] were purchased from ATCC (American Type Culture Collection, Manassas, VA). These cells were cultured using RPMI-1640 medium (ATCC, 30-2001) with 10% fetal bovine serum (FBS) (ATCC, 30-2020) along with 100 U.mL penicillin (antibiotic-antimycotic, Life Technologies), 100 μg/mL streptomycin and L-glutamine, and were cultured in T25 flasks (Corning) inside an incubator at 37 °C in a humidified atmosphere containing 5% CO_2. The Jurkat line is a suspension cell line that has a highly spherical cell morphology, which is important for the later image analysis and data processing.

Jurkat cells were experimentally determined to have diameters ranging from 10 μm to 16 μm. The cells were collected, centrifuged at 800 g for 10 minutes, and then resuspended in 1× phosphate buffered saline (PBS) (288 mOsm/kg) at a cell density of about 5×10^5/mL and used for experiments within 3 hr.

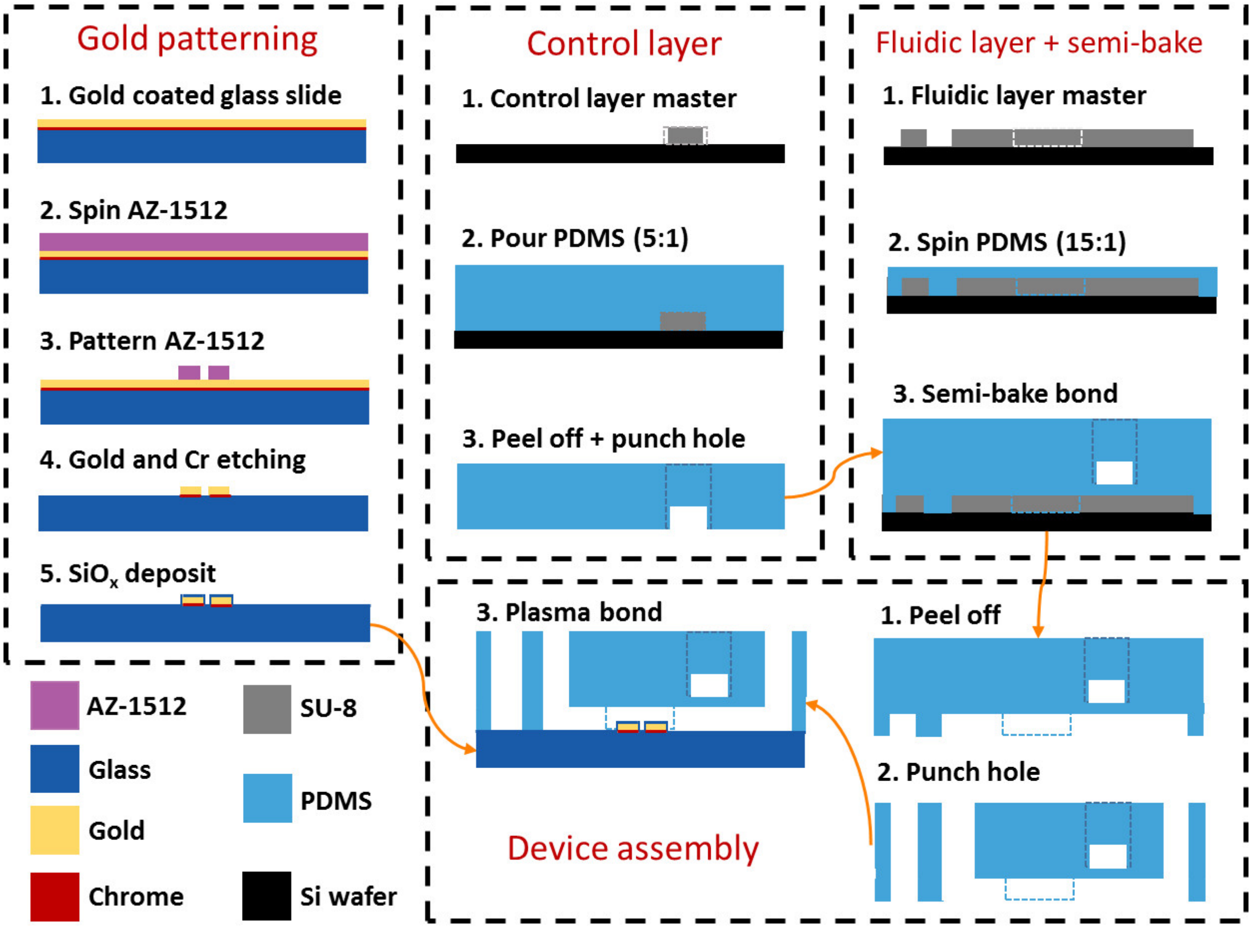

Figure 4.1: Device fabrication: Step-by-step procedures of conductive patterning, double-layered PDMS channel fabrication, and device assembly.

4.2.2 Microdevice fabrication

The device fabrication consists of several core steps as below, including: patterning of conductive wire on the glass slide, fabrication of the double-layered PDMS microfluidic channel, and assembly of the device, which is showed in Fig. 4.1.

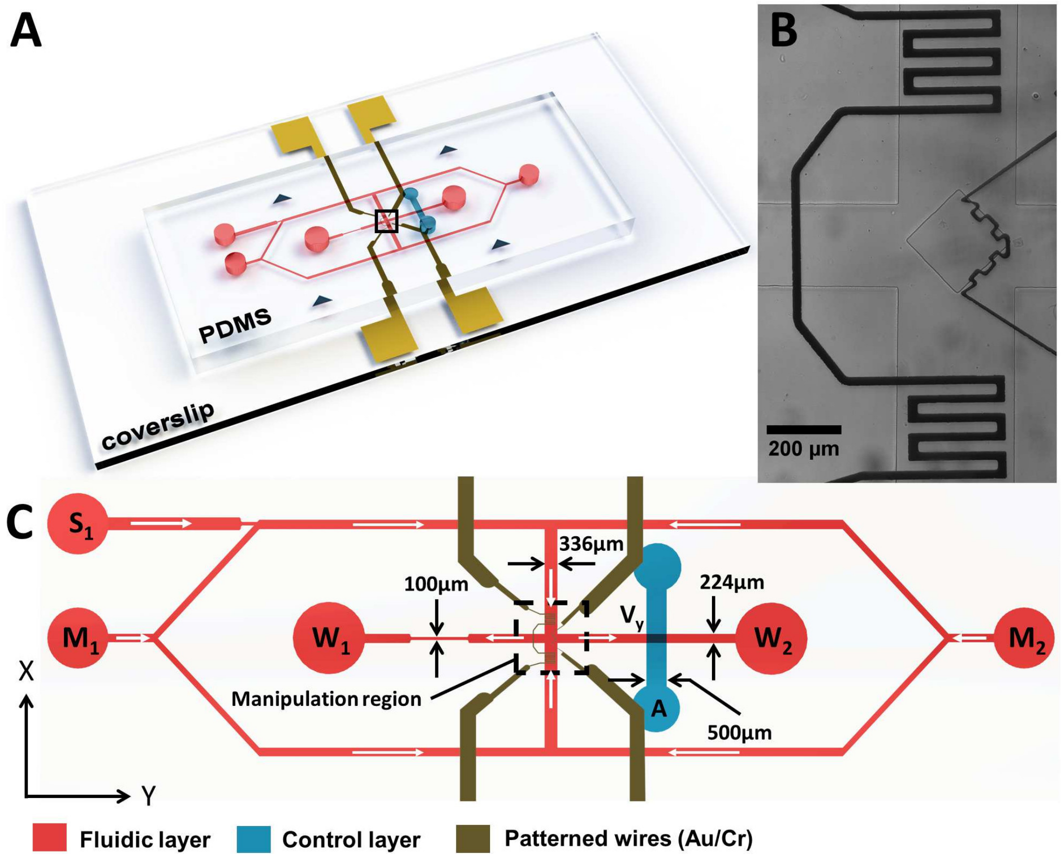

Figure 4.2: Microfluidic platform with integrated flow and temperature control: (A) 3D rendering illustration of the microfluidic device, showing the glass slide etched with gold wires, double-layered PDMS with microchannels; (B) Microscope picture showing enlarged view of the boxed region: microheater (rest on the side) and the temperature sensor (sitting at the cross-slot region); (C) Plane view of the microfluidic device, showing: media inlets M_1, M_2; cell inlet S_1; waste outlets W_1, W_2; valve pressure regulation port A.

Conductive wire patterning

A glass slide (EMF, CA-134) with a 1000 Å thick gold film on a 50 Å thick chrome adhesion layer was used for conductive wire patterning. The slide was spincoated with a positive photoresist with thickness of 1.5 μm (Microchem, AZ-1512), followed by a soft baking process at 110 °C for 2 min. The exposure process was carried out by using a mask aligner (ABM-aligner, ABM-USA Inc.) under wavelength of 365 nm for 5–6 sec. The photoresist was then developed using 25 % v/v aqueous photoresist solution (Microchem, AZ-340) for 1 min. The glass slide with the patterned photoresist was baked at 110 °C for 1 hr. A wet etching process was conducted by immersing the glass slide into gold etchant (TFA gold etchant, Transene) for 30–35 sec, followed by immersing the glass slide immediately in chrome etchant (TFE chromium etchant, Transene) for 2–3 sec. The glass slide was rinsed by acetone to remove residual photoresist. The etched glass slide was again rinsed with isopropanol (IPA) and water, and dried by nitrogen gas. The glass slide, together with the electric connection pads covered by Teflon tape, was coated with 100 nm silicon dioxide to prevent any electrolysis.

Fabrication of the double layered microchannel

The microfluidic channel was fabricated using standard multilayer soft-lithography (MSL) with PDMS. [76] The designed double layered microchannl consist of two layer of PDMS: (1) the control layer, where the pressure regulated gas goes, used to control the local flow resistance of the channel of fluidic layer; (2) the fluidic layer, where is liquid flow goes, containing experiment media and sample cells. The fabrication procedure is shown in Fig. 4.1 and addressed in details in the ESI.

4.2.3 Experimental setup

Simultaneous on-chip flow and temperature control was accomplished by employing a LabVIEW virtual interface that communicated with pressure regulator, temperature controller, and digital multimeter (Fig. 4.3).

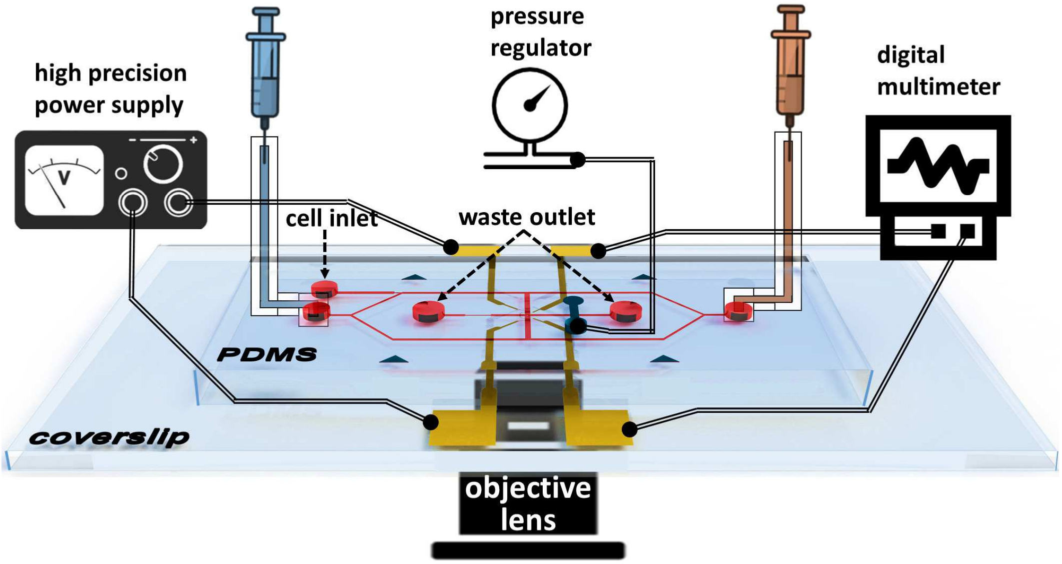

Figure 4.3: Schematic of the cell trapping and manipulation microfluidic platform with integrated flow and temperature control: a gas regulator controls the fluid resistance in the fluidic channel by regulating the pressure inside the control channel; a syringe pump introduces fluid flow inside the fluidic channel; a high precision power supply and a digital multimeter are connected to the micropatterned wires. The microfluidic platform is placed on an inverted microscope equipped by a high speed camera (Phantom V310, vision research). The entire system is remotely controlled by a custom designed LabVIEW virtual interface.

The pressure regulation of pneumatic valves was achieved with a gas regulator (Proportion-Air, QPV1). The gas regulator changes the flow resistance in one of the outlet channels, leading to a control of the flow rates in both channels, redistributing the planar extensional flow pattern. Through active feedback control, cell can be trapped in the velocity potential well, created by actively manipulating the stagnation point of the extensional flow. A multifunction data acquisition module (National Instruments, PCI 6229) with a connection terminal (National Instruments, BNC 2110) is used as digital Input/Output (I/O) for the feedback control of the gas regulator. A high precision power supply (BK Precision, 9124) is used as a power source for the microheater. A MOSFET switch, controlled by the pulse width modulation (PWM) signal from a microcontroller module (NI USB 6009), was used for the fine control over the heating power of the microheater. A digital multimeter (Keithley, 2700 with 7703 switch module) was used to measure the resistance of the temperature sensor, which can be converted to the temperature reading by the resistance-temperature relation obtained from the temperature sensor calibration. Syringe pumps (Cetoni, neMESYS) were used to pump fluids inside the microfluidic channel. The microfluidic chip was placed on an inverted microscope (Nikon, Eclipse Te2000-s). Images were recorded by a high speed camera (Phantom vision research, V310) with the resolution of 600 by 600 pixels, 8-bit depth (256 gray levels).

4.2.4 Image analysis

The raw image frames were enhanced (sharpen), cropped from the original video with Cine Viewer software (Vision Research, Wayne, NJ). The obtained images were then processed, with extended minimum segmentation algorithm followed by morphology processing to find the cell boundary and generate binary cell masks. Thereafter, the two-dimensional cell area was evaluated by pixel counting and then covered to three-dimensional cell surface area and volume based on the assumption of spherical cell shape. In order to assess the hypothesis of spherical cell shape, the sphericity of Jurkat cell (real-time detect through the experiment process) was evaluated, which was defined as $2\pi \cdot r_{equ}/p_{act}$. Here, r_{equ} is the equivalent cell radius calculated with the two-dimensional cell area based on spherical cell shape assumption, and p_{act} is the perimeter of the obtained two-dimensional mask of trapped cell, which is showed in ESI.

4.2.5 Evaluation of temperature control response and stability

To evaluate the temperature control response and stability, we ran 1x PBS through the device and set the target temperature to 37 °C. After the temperature was stabilized, we maintained the temperature at 37 °C for 110 sec, while acquiring temperature sensing data.

4.2.6 Determination of cell membrane properties

Determination of osmotically inactive cell volume (V_b)

The Boyle van't Hoff relationship can be used to determine V_b, the osmotically inactive volume of the cell (μm^3). The osmotic response of the cell volume during hypertonic shrinkage and hypotonic expansion can be described as

$$V = \frac{C_0(V_0 - V_b)}{C_n^i} + V_b \tag{4.1}$$

where V (μm^3) is the cell volume when the intracellular osmolality is C_n^i (Osm/kg water), V_0 is the isotonic cell volume, C_0 is the isotonic osmolality, and V_b is the osmotically inactive cell volume.

Determination of cell membrane permeability to water (L_p) when no CPA exists

The membrane permeabilities to water (L_p) of Jurkat cell (immortalized line of human T lymphocyte cells) were determined by measuring cell volume shrinkage while cells were perfused by hypertonic 3× PBS solutions. The cell volume changes, i.e., water transport across the cell membrane, can be described as [27,30,31]

$$\frac{dV_C(t)}{dt} = L_p \cdot A \cdot (C_n^i - C_n^e) \cdot R \cdot T \tag{4.2}$$

where $V_c(t)$ is the cell volumes (μm^3) at time t (min); L_p is the cell membrane permeability to water ($\mu m/atm/min$; A is the cell membrane area (μm^2) and assumed as constant during perfusion ($= 4\pi r^2$ for a spherical cell shape); C_n^i, C_n^e are the intracellular and extracellular molalities (Osm/kg water), respectively; R is the universal gas constant (=0.008207 (atm L)/(mol K); and T is absolute temperature (in Kelvin). All the calculation was done under the assumption that the cells were spherical. The L_p was determined by least-squares curve fitting of the cell volume change data to the equation using MLAB (Civillized Software Inc., Silver Spring, MD).

Determination of cell membrane permeabilities to water (L_p) and CPA (P_S): two-parameter transport formalism

When permeant CPA (e.g. DMSO) and salts (e.g., NaCl) co-exist in a solution, the cell membrane permeability to water (L_p) and to the CPA (P_S) can be determined with a two-parameter transport model, where the cell volume change depends on both factors: [27,32–35]

$$\frac{dV_C(t)}{dt} = \frac{dV_S(t)}{dt} + L_p \cdot A \cdot (C^i - C^e) \cdot R \cdot T \tag{4.3}$$

where $V_C(t)$ and $V_S(t)$ are cell volume and intracellular CPA volume, respectively, at time t, and C^i, C^e are intra- and extracellular molalities (including both salts and CPA).

The CPA flux is given by

$$\frac{dN_S(t)}{dt} = P_S \cdot A \cdot (C_S^e - C_S^i) \tag{4.4}$$

where P_S is the cell membrane permeability to the CPA (cm/min); C_S^e and C_S^i are the extracellular and intracellular CPA molalities, respectively; and $N_S(t)$ is the mole of intracellular CPA at time t.

$N_S(t)$ and $V_S(t)$ are interchangeable by

$$N_S(t) = V_S(t)/\bar{V}_S \tag{4.5}$$

Here, $\bar{V}_S$ is the partial molar volume of the CPA.

The determination of L_p and P_S was done by least-squares curve fitting of the experimental data to the above two-parameter formalism using MLAB (Civilized Software Inc.)

4.2.7 Determination of the activation energy (E_a) of L_p and P_S

If the transport coefficients at room temperature (22 $°C$) are known, the original Arrhenius equation can be modified into form shown below:

$$L_p = L_{p0} \cdot \exp\left(-\frac{E_{a,water}}{R} \cdot \left(\frac{1}{T} - \frac{1}{T_0}\right)\right) \tag{4.6}$$

$$P_S = P_{S0} \cdot \exp\left(-\frac{E_{a,CPA}}{R} \cdot \left(\frac{1}{T} - \frac{1}{T_0}\right)\right) \tag{4.7}$$

Here, L_{p0} and P_{S0} are the the cell membrane permeability to water (μm/min/atm) and to the CPA (cm/min) at room temperature (22 $°C$), respectively. E_a is the activation energy of corresponding transport coefficient. The determination of E_a of L_p and P_S was done by least-squares curve fitting of the measured L_p and P_S result at 22 $°C$, 30 $°C$ and 37 $°C$, to the modified Arrhenius equation.

4.3 Results

4.3.1 Temperature control stability and temperature profile

Fig. 4.4A presents the actual temperature response to the target temperature change when 30 °C, 37 °C, and then 30 °C were set as the target temperatures. It shows that the temperature of the medium can reach target temperature in 20 sec. Fig. 4.4B shows the temperature stability when keeping 37 °C as the setting temperature. During the recording period (110 secs), temperature reading was very stable, and the fluctuation was within ±0.25°C. Fig. 4.5 shows the results from multiphyscis simulation. Fig. 4.5A and C demonstrate the spacial temperature distribution and spacial temperature gradient distribution, respectively. Fig. 4.5B and D plot the 1 dimension temperature distribution and temperature gradient along the center line of trapping region (marked in red dashed line in Fig. 4.5A and C), respectively. The results show that the temperature in the trapping region is around $37°C$, with temperature gradient less than $0.0034°C/\mu m$, which means the temperature nonuniformity would by only $0.034°C$ for a region of $10\mu m$. Therefore, we can assume that temperature is uniform around a cell with diameter of $10\mu m$.

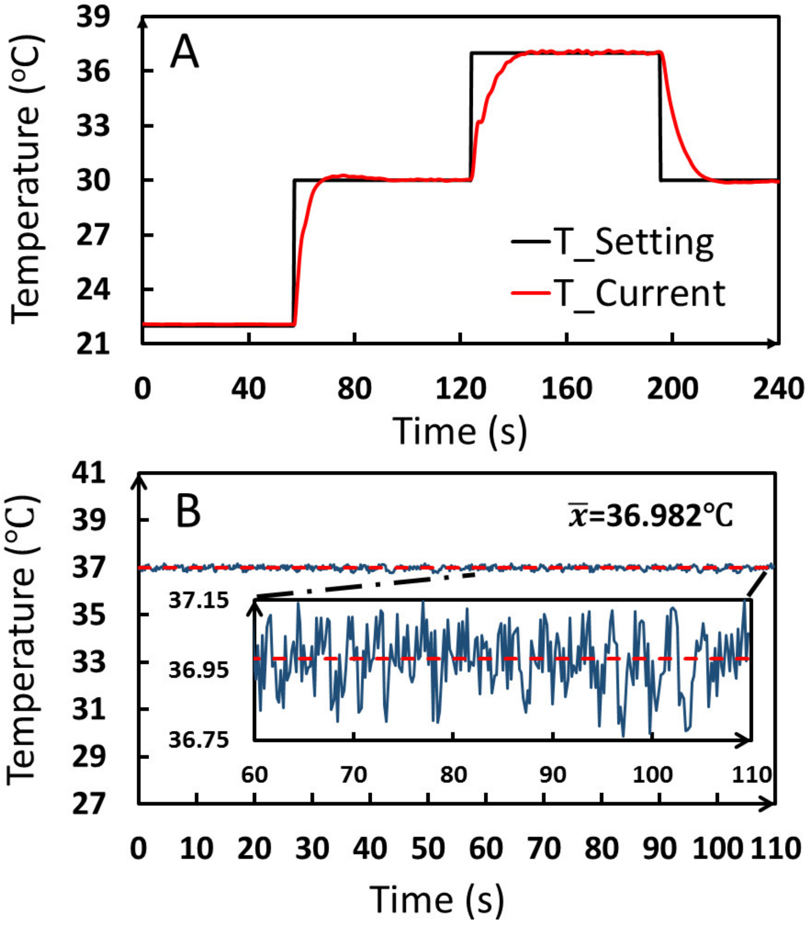

Figure 4.4: Temperature control performance: (A) Temperature response under steps of setting temperatures (30 °C, 37 °C then 30 °C); (B) variation of recorded temperature when maintaining setting temperature at $37°C$, $\bar{x}$ is the mean value of the recorded temperature in 110 sec.

4.3.2 Osmotically inactive cell volume V_b

The Boyle van't Hoff plot of Jurkat cells is shown in Fig. 4.6. The equilibrium cell volumes in isotonic (1× PBS), hypertonic (1.5×, 2× and 3× PBS), and hypotonic (0.7× PBS) saline solutions, normalized to the cell volume in isotonic solution are plotted with respect to the reciprocal of the osmolality of the solution. The y-intercept is the osmotically inactive cell volume fraction (V_b/V_0), i.e., the remaining cell volume when the osmolality approaches infin-

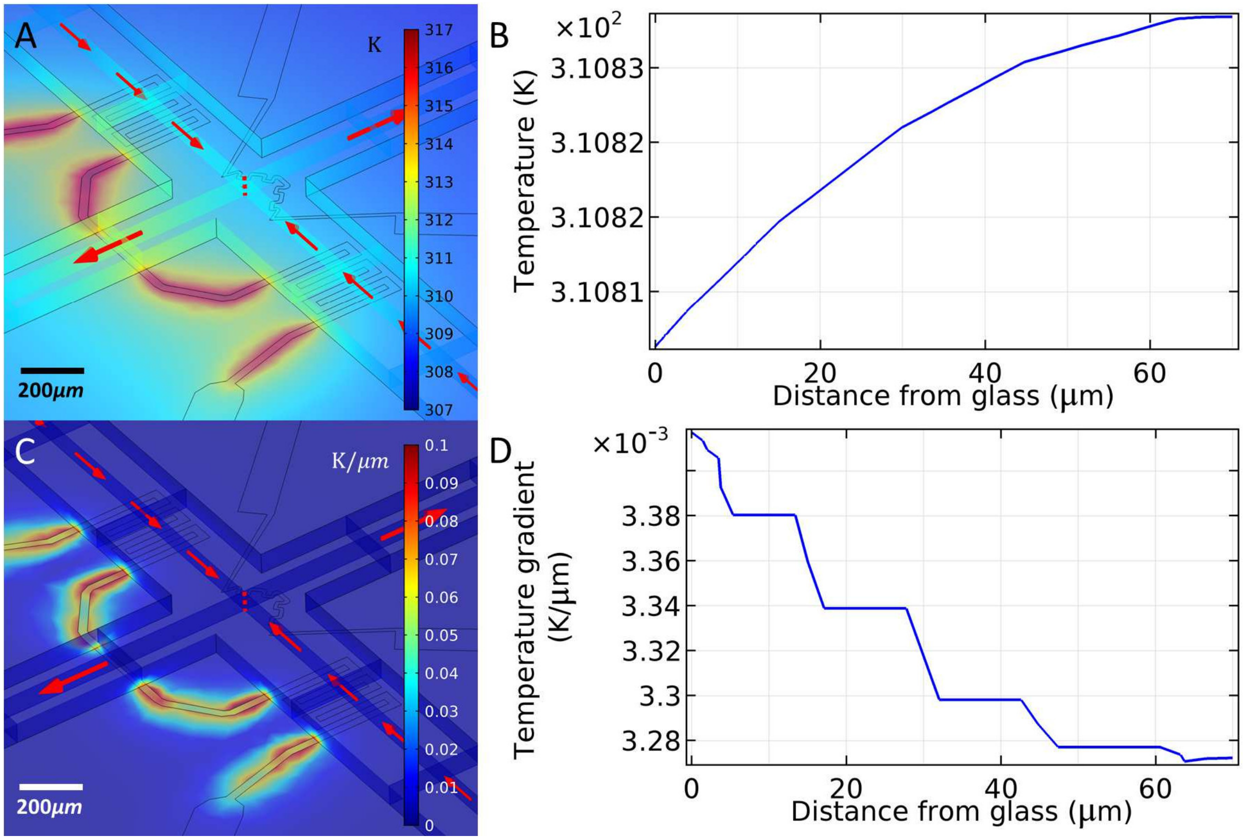

Figure 4.5: Multiphysics simulation results: (A) Spacial temperature distribution; (B) temperature variation along the center line of trapping region (marked in red dashed line in (A)); (C) spacial temperature gradient (K/μm) distribution; (D) temperature gradient variation along the center line of trapping region (marked in red dashed line in (C))

ity. As shown in the plot, the osmotically inactive volume V_b of Jurkat cells was determined to be $67.41 \pm 4.07\%$ V_0.

4.3.3 Cell membrane permeabilities to water (L_p) and cryoprotective agents (P_S) at various temperatures

Examples of the Jurkat cell volume excursion history when perfused by a hypertonic saline solution and a permeating CPA solution under various temperatures are show in Fig. 4.7. The cell volume derived from the last of the 30 frames in each second was calculated and

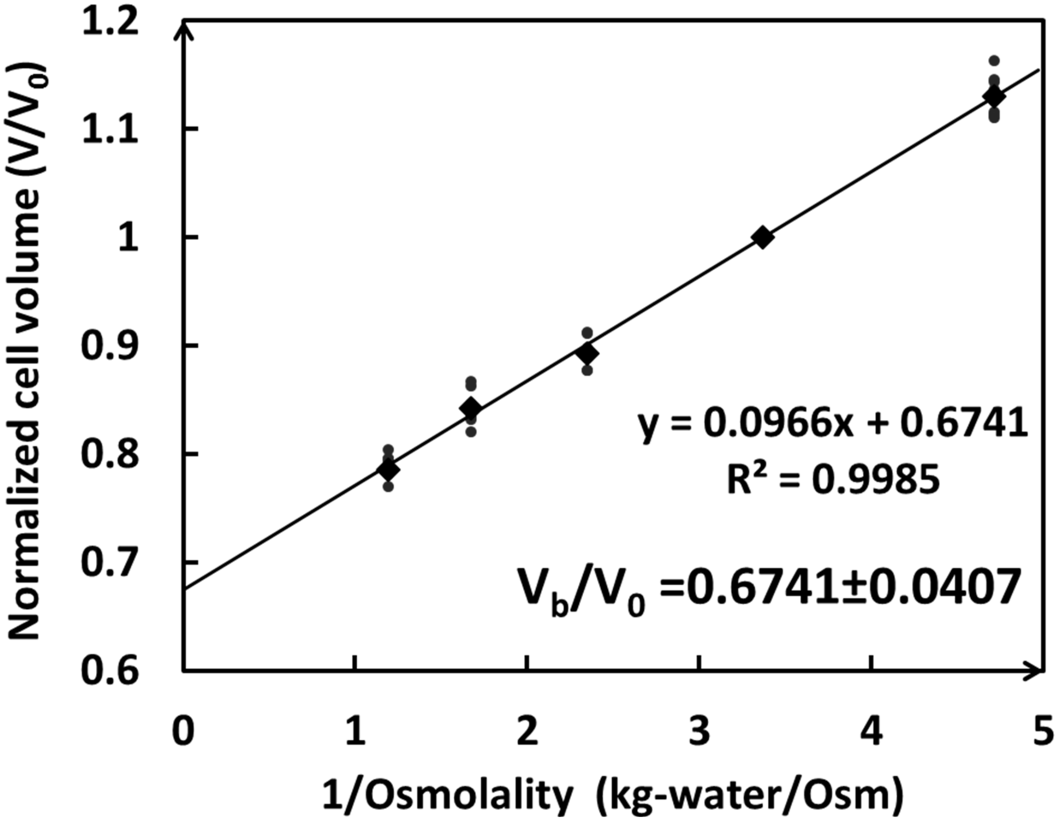

Figure 4.6: Determination of osmotically inactive cell volume V_b with linear curve fitting Boyle van't Hoff plots: x axis indicates the reciprocal of osmolality, y axis shows the equilibrium cell volumes normalized to the cell volume in isotonic solution. The data points used for linear curve fitting are the average of ten measurement results at corresponding concentrations. The obtained osmotically inactive cell volume V_b is $67.41 \pm 4.07\%$ V_0.

presented in the figures.The left column of Fig. 4.7 shows that when a cell is exposed to a hypertonic saline solution, its volume continuously decreases until it reaches the final equilibrium value. Based on the volume excursion data, the water transport ability, i.e., cell membrane permeability to water L_p, can be simulated. The right column of Fig. 4.7 shows the volume excursion of one cell perfused by 10% DMSO in 0.9% NaCl solution. The result indicates that the cell shrinks first and then gradually expands back, which is caused by the transport of both water and permeating CPA. By fitting the cell volume excursion history to the water/CPA transport governing equations (Eq. 4.2, 4.3), the cell membrane

Table 4.1: Membrane permeabilities of Jurkat cells to water and DMSO at various temperatures (mean±standard deviation)

	Temp.(°C)	Times	L_p (μm/min/atm)	P_S (10^{-3}cm/min)
PBS	22	8	0.370 ± 0.019	
	30	10	0.388 ± 0.027	
	37	7	0.775 ± 0.072	
DMSO	22	9	0.158 ± 0.011	0.042 ± 0.004
	30	7	0.188 ± 0.011	0.241 ± 0.005
	37	8	0.436 ± 0.013	0.675 ± 0.032

permeabilities to water and CPA can be calculated. The cell membrane permeabilities to water (L_p) and CPA (P_S) were simulated by least-squares curve fitting using MLAB. The results are shown in Table 4.1.

4.3.4 The activation energy (E_a) of cell membrane permeabilities to water (L_p) and cryoprotective agents (P_S)

After obtaining the cell membrane permeabilities to water (L_p) and cryoprotective agents (P_S) at different temperatures, these results were fitted to the Arrhenius equation (Eq. 4.6&4.7) to estimate the activation energy (E_a) of cell membrane transport properties. The activation energy (E_a) of L_p was determined to be 7.075 kcal/mol when no CPA exists, the activation energy (E_a) of L_p was determined to be 9.566 kcal/mol and the activation energy (E_a) of P_S was determined to be 34.416 kcal/mol, respectively, when CPA and salts co-exist.

4.4 Discussion

Cryobiologists attempt to develop optimal cryopreservation protocols from scratch based on fundamental cell membrane properties, which ensures minimal cell injury from ice crystal formation and hypertonic solutes. To aid this process, various devices and measurement technology have been developed to characterize intrinsic cell membrane transport properties. The determination of intrinsic cell membrane transport properties is essential for the development of optimal cryopreservation, in the following three aspects: (I) It helps to evaluate whether a CPA is a good option for certain cell type. Generally, it's preferred to use the CPA that has large P_S and low toxicity for the cell type; (II) P_S and L_p reflect how fast the CPA and water transfer across cell membrane, which is critical for the mass transfer across cell membrane and cell volume excursion during the CPA addition and removal procedure. In order to minimize the osmotic injury to the cells, we need to add/remove CPA solution in a stepwise manner. With such L_p and P_S values determined, we can develop the optimal CPA addition/removal protocol, minimizing both the osmotic injury to the cell and cytotoxicity (the longer of exposure time in the CPA, the higher toxicity to the cells); (III) With L_p, P_S and corresponding E_a determined, we can predict the optimal cooling rate for certain cell type. According to Mazurs two-factor hypothesis, [3] two different kinds of injuries may happen to cells during cooling: (1) when the cooling rate is too fast, a large amount of water will remain inside the cell and be crystallized, causing intercellular ice formation (IIF) injury ; (2) on the other hand, when the cooling rate is too slow, water has enough time to travel out of cell before ice formation happens, raising intercellular medium concentration, causing osmotic and solute injury to the cell. Hence, an optimal cooling procedure should be slow enough to avoid IIF injury and fast enough to avoid the solute injury. Such optimal cooling rate is determined by the temperature-dependent cell membrane permeabilities.

However, problems like limited experiment time scale for individual cells, precise localized temperature control and measurement, and image processing error from the compromised images with significant noise remain unsolved. Due to these challenges, very few reports have been published about temperature-dependent cell membrane transport properties. We believe this is due to a lack of reliable technology for cell manipulation and temperature control. In other words, a device that can trap and manipulate single cells, while maintaining fast and robust control of the local temperature, is still unavailable. Our device achieved instantaneous non-contact trapping and localized temperature control, which provided access to not only trapping single cell and switching extracellular media, but also manipulating the

Table 4.2: L_p and P_s (to DMSO) of various cell types at room temperature (RT)

Cell type	L_p at RT (μm/min/atm)	P_S to DMSO at RT (10^{-3}cm/min)	Reference
Rat basophilic leukemia cell	0.38	0.49	27
Golden hamster pancreatic islet	0.27		30
Human prostate cancer cell	0.45		127
Human granulocyte	0.18	0.464	128
Human lymphocyte (from blood)	0.46		129
Human vaginal mucosal T cell	0.196	0.4972	130
Human vaginal mucosal macrophage	0.295	0.978	130
Human acute lymphoblastic leukemia cell	0.370	0.042	Current study

local temperature of extracellular media.

In this work, we developed a device with integrated local temperature control and hydrodynamic cell trapping, while enabling rapid media switching. Targeted cell can be steady trapped from tens of minutes up to several hours, within a continuously flowing extensional flow. [100] This ensures uniform on-membrane mechanical interaction and a chemostatic extracellular environment, which reduces the inherent errors coming from experimental setup and improve following image process precision. Considering high temperature may cause injury to cell, we applied a conservative controller setting to avoid significant temperature overshoot. Even though, the rise time (the time required for the response to rise from 10% to 90% of its final value) is within 10 sec and the setting time (the time required for the response to reach and stay within 5% of the final value) is within 20 secs, with variation within ± 0.25 °C. The temperature gradient at cell trapping region is below 0.0034 °C/μm, indicating that for a cell with 10μm in diameter, the temperature nonuniformity across a cell is less than 0.034 °C.

Furthermore, we used the microfluidic cell manipulation platform to measure the cryobiological properties of Jurkat cells, i.e. cell membrane permeability to water (L_p) and to cryoprotective agent (CPA) solution (dimethyl sulfoxide (DMSO) in this study) (P_s) at various temperatures (room temperature, 30°C, and 37°C). The osmotically inactive cell volume V_b, is determined as 67.41% of the isotonic cell volume V_0, which shows good fit to the literature results. [131] Cell osmotic behavior during perfusion with 3×PBS and 10% DMSO was observed. As a result, cell membrane permeabilities to water (L_p), when perfused to impermeable solutes only, at various temperatures were determined to be: 0.370 ± 0.019 (22°C), 0.388 ± 0.027 (30°C), 0.775 ± 0.072 (37°C). Cell membrane permeabilities to water (L_p) and to DMSO (P_S), when perfused with CPA and salts co-exist solution, at various temperature were determined to be: 0.158 ± 0.011 and 0.042 ± 0.004 (22°C), 0.188 ± 0.011 and 0.241 ± 0.005 (30°C), 0.436 ± 0.013 and 0.675 ± 0.032 (37°C). Table 4.2 compares cell membrane transport properties of various cell types with our results at room temperature (RT). This comparison indicates that Jurkat cell has similar L_p to rat basophilic leukemia cell, human lymphocyte, which may be due to their similar cellular structure and function. Jurkat cell also presents the lowest P_s to DMSO at RT, which suggests a slower process of DMSO addition and removal for this specific cell type. Table 4.3 compares the results of our study with references at various temperatures. An increase in L_p and P_s was observed when the temperature of surrounding medium was increased, as expected. Moreover, current study shows that Jurkat cell membrane transport properties are more sensitive to temperature change (relatively high Ea value), which can be helpful during the CPA addition and removal, as it can significantly reduce the required time of cell exposure to the CPA at slightly higher temperature. The comparison from current study with references listed in Table 4.2 and Table 4.3 indicates the reported platform a reliable method to determine the intrinsic cell membrane permeabilities. With above temperature-dependent transport properties measured, the activation energy (E_a) of L_p was determined to be 7.075 kcal/mol ($R^2 = 0.716$) when no CPA exists, the activation energy (E_a) of L_p was determined to be 9.566 kcal/mol ($R^2 = 0.716$) and the activation energy (E_a) of P_S was determined to be 34.416 kcal/mol ($R^2 = 0.716$), respectively, when CPA and salts co-exist. The results of P_s yielded a good linear fit, while the results of L_p did not. In our opinion, this may be caused by the phase transition of the cell membrane during the temperature change, which can alter the activation energy of cell membrane permeability to water. [132]

Table 4.3: L_p and P_s (to DMSO) of various cell types at various temperature

Cell type	Temp.°C	L_p (μm/min/atm)	P_S to DMSO (10^{-3}cm/min)	Reference
Human oocyte	20	0.40		133
	30	0.55		
	37	0.55		
Human megakaryocytic cell	12	2.17	1.32	32
	22	2.26	1.8	
	37	3.87		
Mouse dendritic cell	22	0.16	0.63	28
	25	0.95		
	32	1.54		
Human acute lymphoblastic leukemia cell	22	0.370	0.042	Current study
	30	0.388	0.241	
	37	0.775	0.675	

4.5 Conclusions

In this chapter, a co-flow media switching mechanism was integrated to developed cell confinement and manipulation platform for the determination of the temperature-dependent cell membrane permeabilities. The reported platform achieves the following features: (1) hydrodynamic confinement of single cell; (2) switching extracellular medium during the cell trapping; (3) controlling surrounding medium temperature at the same time. It offers a truly chemostatic environment for observing cell osmotic behavior, allowing for continuous delivery of fresh media with continuous removal of contacted media, under precise local media temperature control. As proof-of-principle validation, the reported platform was used for the determination of Jurkat cell membrane transport properties under various temperatures. The comparison of reported results of Jurkat cell with the reference data [27,129,131] demonstrates it a reliable method for temperature-dependent cell behavior study. In comparison to alternative techniques, this integrated platform provides straightforward method for temperature-dependent cell osmotic behavior study. The design principle is highly transformable to application scenarios that require cell manipulation and temperature control at the same time, as the main additional components to accomplish our design are pressure regulators (Proportion Air) and LabVIEW software/hardware. In a word, the features of the reported platform suggest it a valuable tool for the study and analysis of temperature-dependent cell properties that requires reliable cell confinement technique with ability to manipulate extracellular environment, such as advanced cell therapy and drug test.

Overall, the integrated microfluidic platform presented in this work offers a new method for observing cell osmotic behavior under robust temperature control. As it provides a truthful cellular morphology image recording, without the interference from the physical barrier, and precise local temperature reading, the reported platform improves the precision of intrinsic cell cryobiological property measurement, which can assist cell cryopreservation, including the selection of optimal CPA, the optimization of CPA addition and removal, and the prediction of the optimal cooling rate.

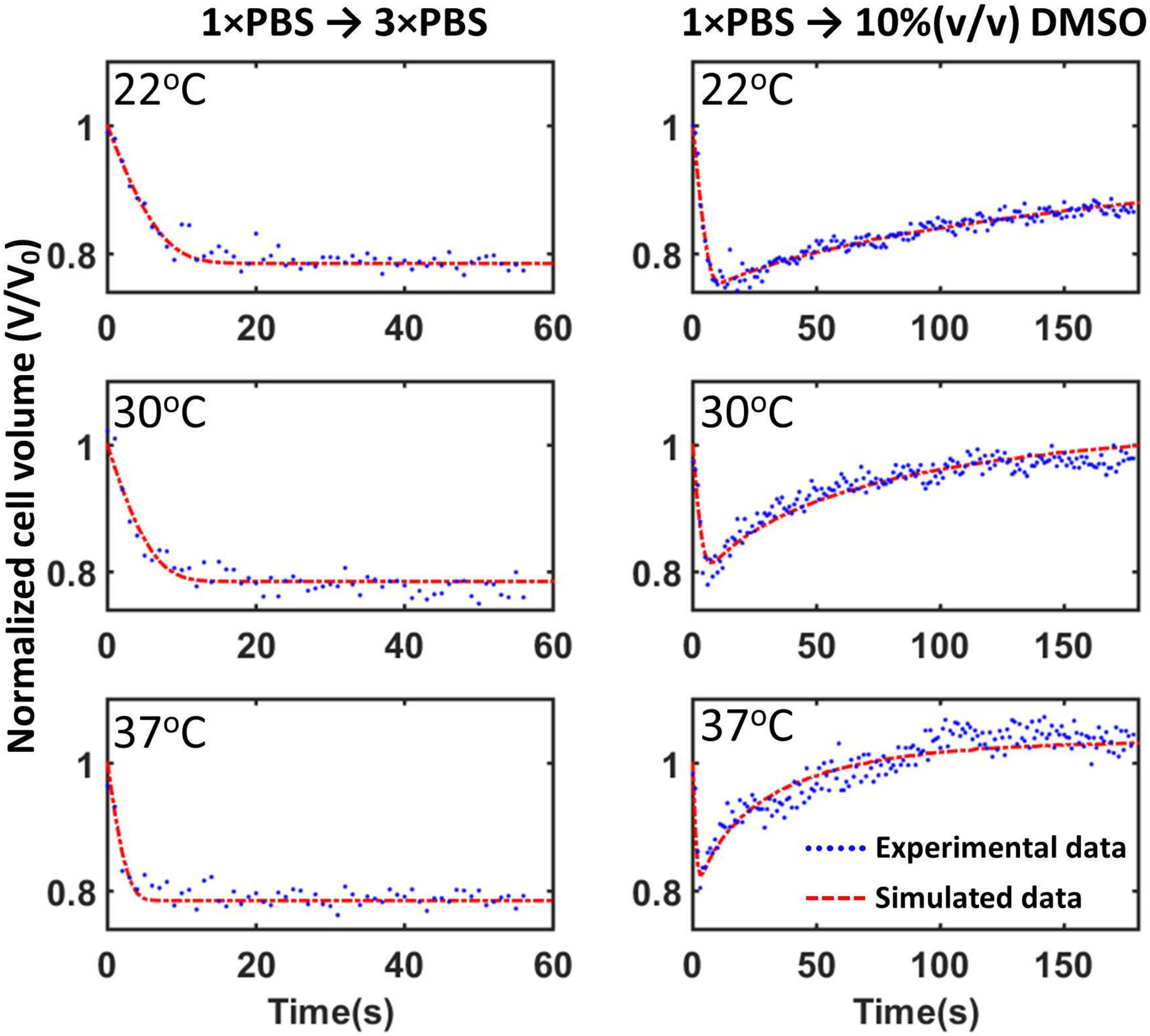

Figure 4.7: Cell volume excursion during perfusion by hypertonic solutions at various temperature: The left column: 1×PBS to 3×PBS at 22°C, 30°C, 37°C; The right column: 1×PBS to 10% (v/v) DMSO at 22°C, 30°C, 37°C.

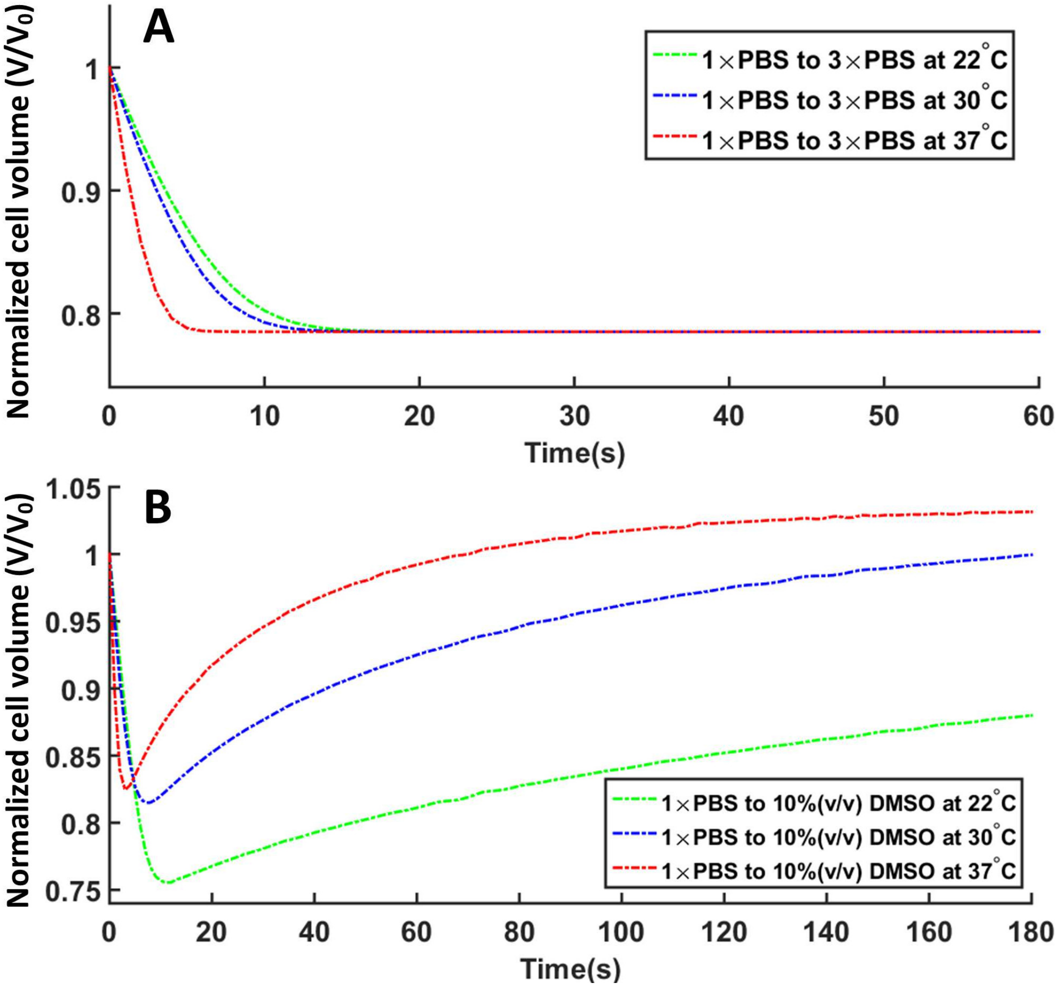

Figure 4.8: Simulated curves of cell volume excursion during perfusion by hypertonic solutions at various temperatures: (A) 1×PBS to 3×PBS at 22°C, 30°C, 37°C; (B) 1×PBS to 10% (v/v) DMSO at 22°C, 30°C, 37°C.

Chapter 5

DIRECT MEASUREMENT OF CELL MEMBRANE TRANSPORT COEFFICIENTS' ACTIVATION ENERGY: A TEMPERAUTRE DEPENDENT MASS TRANFER FORMALISM AND VALIDATION

A temperature dependent across cell membrane mass transfer formalism was proposed in this chapter, which has the advantages, like reflecting the actual cryopreservation situation; including the effect from the potnecial membrane phase transfer and more straightforward and efficient measurement procedure, over traditional method of activation energy measure under static temperatures. Numerical simulation was conducted to investigate the best temperature scanning profile for experimental measurement procedures. Relying on the temperature control capbility of developed cell confinement and manipulation platform, the proposed temperature dependent mass transfer formalism was validated with measurement experiment under controlled temperature scanning profile.

5.1 Introduction

As addressed in previous charpter, cryobiologists need to obtain the membrane permeability of cells or tissues, like L_p P_s, in order to propose the optimal protocols for the addition and remoal of cryoprotective solutes and the optimal cooling rates for cell cryopreservation. A number of formalisms have been proposed druing the past several decades, including a one-parameter (solute permeability) model introduced by Mazur and colleagues [134, 135], a classic two-parameter (water and solute permeability) model [136], and a three-parameter model developed by Kedem and Katchalsky [136]. As the one-parameter model only appliable under many ideal assumptions, we only focus our discussion between the three-parameter Kedem-Katchalsky (KK) model and the two-parameter model.

Three-parameter Kedem-Katchalsky model to two-parameter model

The main difference between three-parameter Kedem-Katchalsky model and two-parameter model is that the KK model introduces an interaction term, sigma [136], to deal with solvent and solute transport through a common channel specifically. Thanks to its universality, the KK model is also generally appliabile to other simple transport situation with or without cotransporting. Although most general of the three transport model, the KK model has the disadvantages that the interaction parameter, sigma, significantly increases the complexity of the transport formalism and is commonly misunderstood and improperly calculated. New discoveries of molecular biology indicate that, in natural biological membranes, cotransport is often unlikely or negligible [137]. These findings lead cryobiologist to believe that sigma and the KK model are often unnecessary, while a classic two-paramete model is appropriate and simpler in the actual cryobiological research. To better demostrate this idea, the special case of the KK model when a common channel for solute and solvent is not present (shown in Eq. 5.1) and the two-paramete model (shown in Eq. 5.2) are compared side by side.

$$\begin{cases} \frac{dV_{w+s}}{dt} = -L_pART\left\{\left(M_n^e - M_n^i\right) + \sigma\left(M_s^e - M_s^i\right)\right\} \\ \frac{dN_s}{dt} = (1-\sigma)\frac{M_s^e - M_s^i}{2}\frac{dV_{w+s}}{dt} + P_sA\left(M_s^e - M_s^i\right) \\ V_c = V_{w+s} + V_b \end{cases} \tag{5.1}$$

$$\begin{cases} \frac{dV_{w+s}}{dt} = -L_pART\left(M_{n+s}^e - M_{n+s}^i\right) + P_sA\widehat{V}_s\left(M_s^e - M_s^i\right) \\ \frac{dN_s}{dt} = \left(M_s^e - M_s^i\right)\left(\frac{1}{2}\frac{dV_{w+s}}{dt}\frac{P_s\widehat{V}_s}{L_pRT} + P_sA\right) \\ V_c = V_{w+s} + V_b \end{cases} \tag{5.2}$$

The observed total cell volume (V_c) is the volume of interest, which is found by adding the cell solids volume (V_b) to the water and solute volume (V_{w+s}). σ is constrained by the condition

$$0 \leq \sigma \leq 1 - P_s\widehat{V}_s/L_pRT \tag{5.3}$$

where $\widehat{V}_s$ is the partial molar volume of the solute. An special case happens when σ equals to 1, representing the scenario that P_s is zero and the membrane is completely impermeable to the solute, from the perspective of a reflection coefficient σ, meaning that all of the solute is reflected ' back' from the membrane. When solute and solvent cross the membrane via independent pathways, e.g., water via channels while solute via lipid bilayer diffusion, the reflection coefficient σ reaches its right bound, the noninteracting (NI) case, that

$$\sigma_{\mathrm{NI}} = 1 - P_s\widehat{V}_s/L_pRT \tag{5.4}$$

where σ is not an independent paramemter but is completely determined by L_p and P_s.

In the two-parameter transport model, cell membrane permeability to water (L_p) and to CPA (P_s) are the independent parameters used to characterize membrane permeability when, a permeable solute (CPA in this study), and a nonpermeable solute (NaCl in this study) are present. The governing equations are shown in Eq. 5.2

The measurement of temperature dependency of cell membrane permeability: the activation energy

Frequently, the membrane permeability of cell is measured as a function of temperature. The temperature dependence of transport parameters is generally expressed as an acivation energy (E_a) which is related to permeability via the Arrhenius relationship:

$$P = P_o \exp\left(-E_a/RT\right) \tag{5.5}$$

where P is the permeability parameter of interest and P_o is a reference constant determined at reference temperature. With the determination of activation energy, we can predict the permeability of interested cell at other temperatures beside measured temerpature. The activation energy is traditionally found by making an Arrhenius plot of the data (ln[P] vs 1/T), least squares fitting the slople, and $E_a = -R{\cdot}\text{slope}$. However, it has drawbacks like (1) limited number of the permeability results of interested cell at static temerpatures may affect the precision of the activtion energy; (2) the measurement conditons are different from actual cryopreservation process, which is under monotonous changing temperature; (3) the measurement procedures are complicated and may introduce more errors during the data processing.

In a word, a direct measurement method of the activation energy, under a monotonous changing temperature condition, is needed, which offers the advantages as followed: (1) tt reflects the actual cryopreservation situation; (2) tt takes the potnecial membrane phase transfer into account; (3) the measurement procedures are more straightforward and efficient.

5.2 Materials and methods

5.2.1 Formalism of mass transfer equations with dynamic temperature

In order to develop a temperature dependent mass transfer model, it's necessary to transfer the equations from time domain to temperature domain, which is realized through Eq. 5.6

$$\frac{dV_c\left(t\right)}{dt} = \frac{dT}{dt} \cdot \frac{dV_c\left(t\right)}{dT} = B\left(T\right) \cdot \frac{dV_c\left(t\right)}{dT} \tag{5.6}$$

The expression of $dV_C(t)/dt$ depends on whether cell membrane permeable solute is presented or not, shown as followed.

Mass transfer equation for non-permeable solute only situation

The membrane permeabilities to water (L_p) of Jurkat cell (immortalized line of human T lymphocyte cells) were determined by measuring cell volume shrinkage while cells were perfused by hypertonic 3× PBS solutions. The cell volume changes, i.e., water transport across the cell membrane, can be described as [27, 30, 31]

$$\frac{dV_C(t)}{dt} = L_p \cdot A \cdot (C_n^i - C_n^e) \cdot R \cdot T \tag{5.7}$$

where $V_c(t)$ is the cell volumes (μm^3) at time t (min); L_p is the cell membrane permeability to water ($\mu m/atm/min$; A is the cell membrane area (μm^2) and assumed as constant during perfusion ($= 4\pi r^2$ for a spherical cell shape); C_n^i, C_n^e are the intracellular and extracellular molalities (Osm/kg water), respectively; R is the universal gas constant (=0.008207 (atm L)/(mol K); and T is absolute temperature (in Kelvin). All the calculation was done under the assumption that the cells were spherical. The L_p was determined by least-squares curve fitting of the cell volume change data to the equation using MLAB (Civillized Software Inc., Silver Spring, MD).

Mass transfer equation for non-permeable solute with permeable CPA binary solutoin

When permeant CPA (e.g. DMSO) and salts (e.g., NaCl) co-exist in a solution, the cell membrane permeability to water (L_p) and to the CPA (P_S) can be determined with a two-parameter transport model, where the cell volume change depends on both factors: [27,32–35]

$$\frac{dV_C(t)}{dt} = \frac{dV_S(t)}{dt} + L_p \cdot A \cdot (C^i - C^e) \cdot R \cdot T \tag{5.8}$$

where $V_C(t)$ and $V_S(t)$ are cell volume and intracellular CPA volume, respectively, at time t, and C^i, C^e are intra- and extracellular molalities (including both salts and CPA).

The CPA flux is given by

$$\frac{dN_S(t)}{dt} = P_S \cdot A \cdot (C_S^e - C_S^i) \tag{5.9}$$

where P_S is the cell membrane permeability to the CPA (cm/min); C_S^e and C_S^i are the extracellular and intracellular CPA molalities, respectively; and $N_S(t)$ is the mole of intracellular CPA at time t.

$N_S(t)$ and $V_S(t)$ are interchangeable by

$$N_S(t) = V_S(t)/\bar{V}_S \tag{5.10}$$

Here, $\bar{V_S}$ is the partial molar volume of the CPA.

5.2.2 The evaluation of temperautre dependency of across cell membrane transport properties: the arrhenius relation

If the transport coefficients at room temperature (22 $^{\circ}C$) are known, the original Arrhenius equation can be modified into form shown below:

$$L_p = L_{p0} \cdot \exp\left(-\frac{E_{a,water}}{R} \cdot \left(\frac{1}{T} - \frac{1}{T_0}\right)\right) \tag{5.11}$$

$$P_S = P_{S0} \cdot \exp\left(-\frac{E_{a,CPA}}{R} \cdot \left(\frac{1}{T} - \frac{1}{T_0}\right)\right) \tag{5.12}$$

Here, L_{p0} and P_{S0} are the the cell membrane permeability to water (μm/min/atm) and to the CPA (cm/min) at room temperature (22 $^{\circ}C$), respectively. E_a is the activation energy of corresponding transport coefficient.

5.2.3 The coupled mass transfer equations under temperature dynamic

Based on the time domain to temperature domain transformation equation (Eq. 5.6), static temperature mass transfer model (Eq. 5.7 and 5.8) and temperature dependency evaluation of across cell membrane transport properties (Eq. 5.11 and 5.12), the result temperature dependent mass transfer equation is shown as Eq. 5.13. Moreover, the mass transfer equation can be further segmented into the water flux ralated volume change portion and the CPA flux ralated volume change portion, as Eq. 5.14 and Eq. 5.15 respecitively.

$$\frac{dV_c\left(t\right)}{dT} = \frac{dV_s\left(t\right)}{dT} + \frac{L_{p,0}ART}{B\left(T\right)} \cdot \exp\left[\frac{E_{a,L_p}}{R}\left(\frac{1}{T_0} - \frac{1}{T}\right)\right] \cdot \left(C_n^i - C_n^e\right) \tag{5.13}$$

$$\frac{dV_c\left(t\right)}{dT} = \frac{L_{p,0}ART}{B\left(T\right)} \cdot \exp\left[\frac{E_a}{R}\left(\frac{1}{T_0} - \frac{1}{T}\right)\right] \cdot \left(C_n^i - C_n^e\right) \tag{5.14}$$

$$\frac{dV_s(t)}{dT} = \frac{P_{s,0}A}{B(T)} \cdot \exp\left[\frac{E_{a,P_s}}{R}\left(\frac{1}{T_0} - \frac{1}{T}\right)\right] \cdot \left(C_s^e - C_s^i\right) \cdot \widehat{V}_s \tag{5.15}$$

5.2.4 Numerical simulation for optimal temperature scanning profile during measurement

Since temperature is changing during the measurement with temperature dependent mass transfer model, it's important to identify a temperature scanning profile that is suitalbe to the cell volume excursion time window when cell is exposed to hypertonic solution. Numerical simulation using the proposed temperature dependent mass transfer model with various temeprature ramp conditions was conducted.

5.3 Results

5.3.1 Simulation results of temperature dependent across cell membrane mass transfer model

The simulated cell voulme excursion curve under temperature ramps of 0.02K/s, 0.04K/s, 0.06K/s, 0.08K/s, 0.1K/s,0.2K/s,0.3K/s,0.4K/s, with a fixed Ea values of 10 kcal/mole and 35 kcal/mole, are showed in Fig 5.1.

5.3.2 The activation energy (E_a) of cell membrane permeabilities to water (L_p) and cryoprotective agents (P_S) under controlled temperature profile

Examples of the Jurkat cell volume excursion history when perfused by a permeating CPA solution under raising temperature are show in Fig. 5.2. The cell volume derived from the last of the 30 frames in each second was calculated and presented in the figures. The temperature profile cell experienced during the media perfusion is showed in Fig. 5.3

The activation energys of cell membrane permeabilities to water (L_p) and cryoprotective agents (P_S) are determined to be $9.38 \pm 0.57\ kcal \cdot mol^{-1}$ and $65.66 \pm 0.62\ kcal \cdot mol^{-1}$.

Table 5.1: Membrane permeabilities of Jurkat cells to water and DMSO at various temperatures (mean±standard deviation)

	Temp.(°C)	Times	L_p (μm/min/atm)	P_S (10^{-3}cm/min)
PBS	22	8	0.370 ± 0.019	
	30	10	0.388 ± 0.027	
	37	7	0.775 ± 0.072	
DMSO	22	9	0.158 ± 0.011	0.042 ± 0.004
	30	7	0.188 ± 0.011	0.241 ± 0.005
	37	8	0.436 ± 0.013	0.675 ± 0.032

5.4 Discussion

To validate the proposed temperature dynamic coupled mass transfer model, the activation energy results are compared to the values determined by the traditional static temeprature measuremnt medthod.

The activation energy (E_a) of cell membrane permeabilities to water (L_p) and cryoprotective agents (P_S) by static temperature measurement method

From the previous study, we determined Jurkat cell membrane permeabilities to water (L_p) and DMSO (P_S) at various temperatures (room temperature, 30 °C and 37 °C). The results are showed in Table 5.1.

After obtaining the cell membrane permeabilities to water (L_p) and cryoprotective agents (P_S) at different temperatures, these results were fitted to the Arrhenius equation (Eq. 5.11&5.12) to estimate the activation energy (E_a) of cell membrane transport properties. The activation energy (E_a) of L_p was determined to be 7.075 $kcal \cdot mol^{-1}$ when no CPA exists, the activation energy (E_a) of L_p was determined to be 9.566 $kcal \cdot mol^{-1}$ and the activation energy (E_a) of P_S was determined to be 34.416 $kcal \cdot mol^{-1}$, respectively, when CPA and salts co-exist.

The activation energy (E_a) of L_p results are similar, with 9.566 $kcal \cdot mol^{-1}$ for static temperatures measurement and 9.38 $kcal \cdot mol^{-1}$ for dynamic temperature scanning measurement. However, the activation energy (E_a) of P_s results differ from each other with with 34.416 $kcal \cdot mol^{-1}$ for static temperatures measurement and 65.66 $kcal \cdot mol^{-1}$ for dynamic temperature scanning measurement, which may be caused by involving more data point weight from after the cell membrane phase transition.

With the advatages the proposed mass transfer model aquired, there are more potencial benifits of this measurement method, for instance, with wider range of temperature scan, the effect of activation energy of continous temperature window is reflected in the recorded cell volume excursion data. In this way, with once of the measurement experiment, it's possible for us to obtain the activation energy at multiple temperature window within our temperature scan range.

5.5 Conclusions

In this chapter, a coupled across cell membrane mass transfer model under temperature dynamic was proposed. With the assist of numerical simulation of the developed mass transfer model, the optimal temperature scanning profile is indentified and used for the measurement experiement.

The measurement of the activation energy using developed integrated platform, with controlled temeprature scanning profile, was conducted. The activation energys of Jurkat cell membrane permeabilities to water (L_p) and cryoprotective agents (P_S) are determined to be 9.38 ± 0.57 $kcal \cdot mol^{-1}$ and 65.66 ± 0.62 $kcal \cdot mol^{-1}$. The measurement results are compared with the result from the measurement under static temperatures. The experiment validated the coupled across cell membrane mass transfer model under temperature dynamic and demostrated that the developed integrated microfluidic platform has advanced features as followed: (1) Precise and sensitive monitoring of local temperature; (2) Rapid and uniform heating of local extracellular media; (3) Robust and quick media switching.

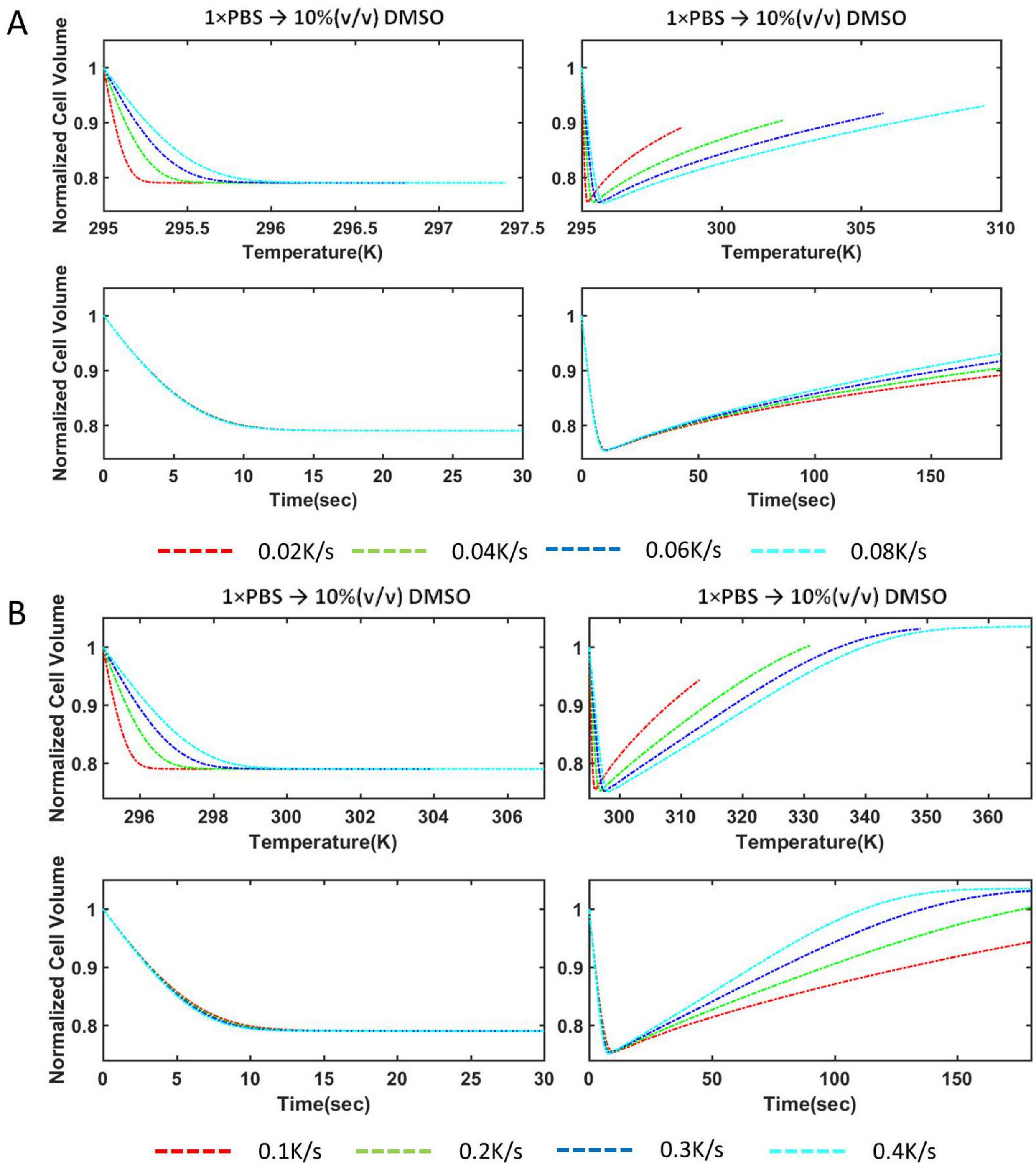

Figure 5.1: Simulation result of cell volume excursion during perfusion by hypertonic solutions at rising temperature under various temperature ramps

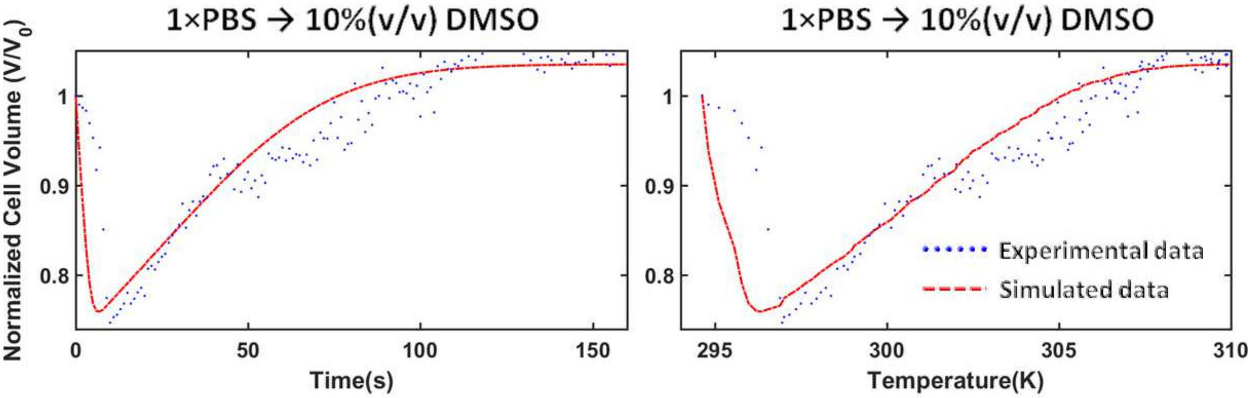

Figure 5.2: Cell volume excursion during perfusion by hypertonic solutions at rising temperature

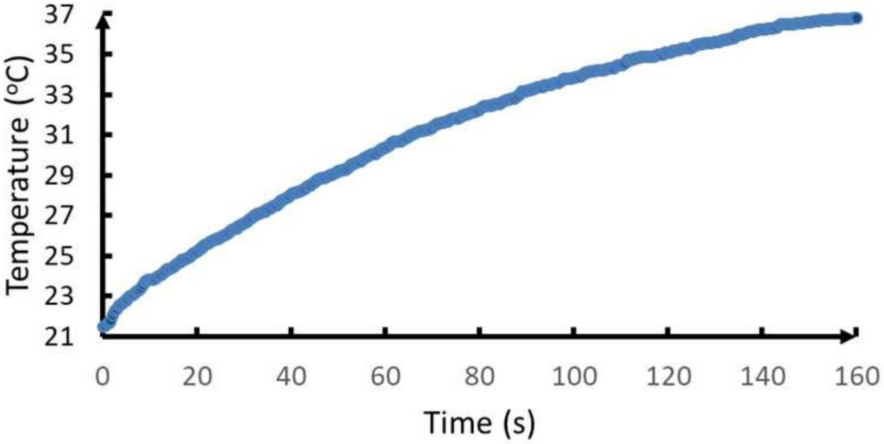

Figure 5.3: The controlled temperature profile during the measurement experiment

Chapter 6

CONCLUSIONS AND FUTURE WORK

6.1 Conclusions

Through the process of human civilization, tehcnology is continously invented to improve the health situation of humam being. Various efforts have benn made from fundamental research to clincial trials by scientists and engineers to fight diseases. Even through we have cured many disease during hunman history, there are more we can't treat them effectively. Cellular therapy, a novel treatment method effectively proved by clinical trials, shows great potenials of offering solutions to the currently incurable diseases, expending a new front line for the war of disease fighting. At the mean time, great challenges and needs arise in cryopreservation during the development and execution of cellular therapy. Specifically speaking, the challenges include the selection of the optimal cryoprotective agents (CPAs), addition of CPA, optimization of the cooling procol, removal of CPAs after thawing, and designing instruments assisting these processes. The optimal cryopreservation protocol of a biomaterial is unachievable without prescisely determining the intrinsic cryobiological characteristics of cells and tissues. In this dissertation, analysis methods and instruments were developed to measure these improtant properties efficiently and precisely, to achieve the optimal biopreservation.

This dissertation has focused on developing cell confinement and manipulation microfluidic platform for the determination of cell membrane properties, which assist the exploration of optimal biopreservation method for cells. Two types of cell confinement technique are investigated: a contact cell confinement using microfluidic perfusion channel and a non-contact cell confinement with hydrodynamic trapping. For the micro-scale local temperature control, by comparision between simulation result of centerred heater design and distributed heater design, the distributed heater design is choosen for better temperature uniformity.

The dissertation also analysed the features, challenges and potencials of developed cell confinement and manipulation platform with the application of determination of cell membrane properties.The developed non-contact cell confinement and manipulation platform achieves features as followed: (1) hydrodynamic confinement of single cell; (2) switching extracellular medium during the cell trapping; (3) controlling surrounding medium temperature at the same time. With the hydrodynamic trapping, the developed platform avoids the interference from the blocker edge of the microfluidic perfusion design and the considerable cell movement during the experiment, which greatly improves the image processing efficiency and the accuracy of measurement results. Ultilizing the developed cell confinement and manipulation platform, the cryobiological propteries of cells like the osmotically inactive cell volume (V_b), the permeability of cell membrane to water (L_p), and the permeability of the membrane to CPAs (P_s) can be determined, which assists the optimization of cryopreservation protocols. Relying on the advanced features of developed cell confinement and manipulation platform, a temperture dependent across cell membrane mass transfer model is proposed and validated with measurement experiment. The comparison of reported results with the reference data demonstrates it a reliable method for temperature-dependent cell behavior study.

Across cell membrane mass transfer model governs solvent and solute exchange across cell membrane, affecting the intercelluar media concerntration. Since the cryoinjuries of cell during freezing depends on the history of intercelluar media concerntration, cryobiologists use across cell membrane mass transfer model to determine cell cryobiological propeties and explore optimal preservation protocol. Traditionally, the mass transfer equations are modeled under thermal equilibrium condition at constant temperature. To evaluate temperature dependency of cell membrane transport propeties, Arrhenius relation is applied with the obtained data from measurement at various constant temperatures. However, a temperature dependent mass transfer model can provide continous temperature dependency of cell membrane transport properties within the measurement window and simplify the experiement procedures. In this dissertation, I origninlly coupled the mass transfer equations with arrhenius relation, transferred the time domain formalism to temperature domain formalism and developed an temperature dependent across cell membrane mass transfer model for the determination of activation energy of transport properties with single measurement experiment. The rapid and sensitive temeprature control capbility of the developed cell confinement and manipulation platform make this mesurement possible. The proposed formalism and measurement method may also inspire new inversitgation approaches of temperature-dependent phenomenon.

In conclusions, valuable tools and methods were developed and investigated with experiments, including a novel non-contact cell confinement and manipulatoin platform with local temperature control, a temperature dependent across cell membrane mass transfer model and a suggested measurement procedures for the activation energy esitimation with the developed temperature dependent across cell membrane mass transfer model. These tools and methods provides more accurate and effcient determination of instric cell cryobiological properties, which assists the investigation of optimal cryopreservation of cells/tissues. Furthermore, thanks to the advanced microscale flow and temperature control capbility, the developed platform provides a valuble tool for general temperature dependent chemical, biochemical, biological study.

6.2 Future work

Beyond the study covered in this thesis, the future of the developed cell confinement and manipulation platform rests on both the further device features integration and application exploration. Although the developed platform offers the capbility of cell trapping and local temperature control, other features, like on-chip active cooling, local fluid shear stress control and the scale up of the current design, can extend the application potencials of the developed platform to the study that required multi-factors control under microscale, for instance on-chip single cell gene expresion study, and the study of shear stress intiated cell differeniation.

To be more specific, beside the heating and temperature control capbility of developed cell confinement and manipulatin platform, further integrating an on-chip cooling mechanism will extend the study range of current platform the beloew room temperature range (Fig. 6.1). Moveover, with an on-chip active cooling source availalbe, more complex temperature profile with quick cooling rate will be possible. In our early stage prototype, we can achieve on-chip temperature history as shown in Fig. 6.2.

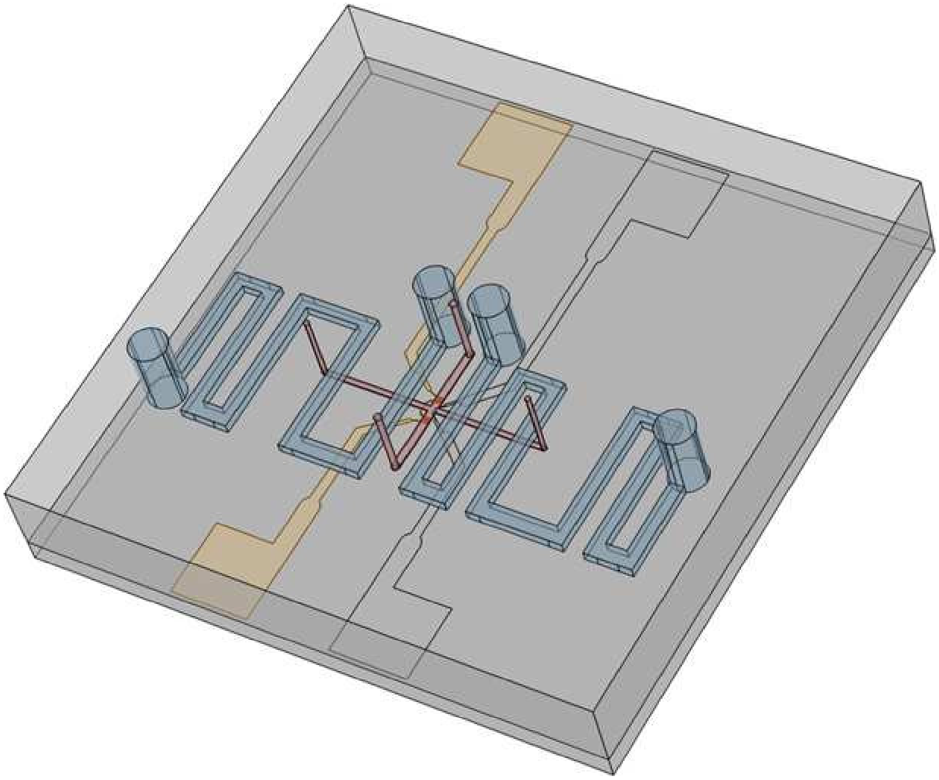

Figure 6.1: Schematic of microfluidic design with on-chip active cooling with microheater (marked in gold), sample fluid layer (marked in red) and cooling layer (marked in blue).

In addition, the developed platform can be applied to investigate and choose novel CPAs for specific cell types. Trahalose is a cell membrane non-permeable CPA that have capbility of inhibiting ice formation during cooling with low cytotoxicity [138]. However, since it's cell membrane non-permeable, cryobiologists can't use it to reduce intracellular ice formation. But reasearches find out that certain treatment conditions (temperature, chemical and so on) can transform the cell membrane to be temporarily permeable to trahalose. With

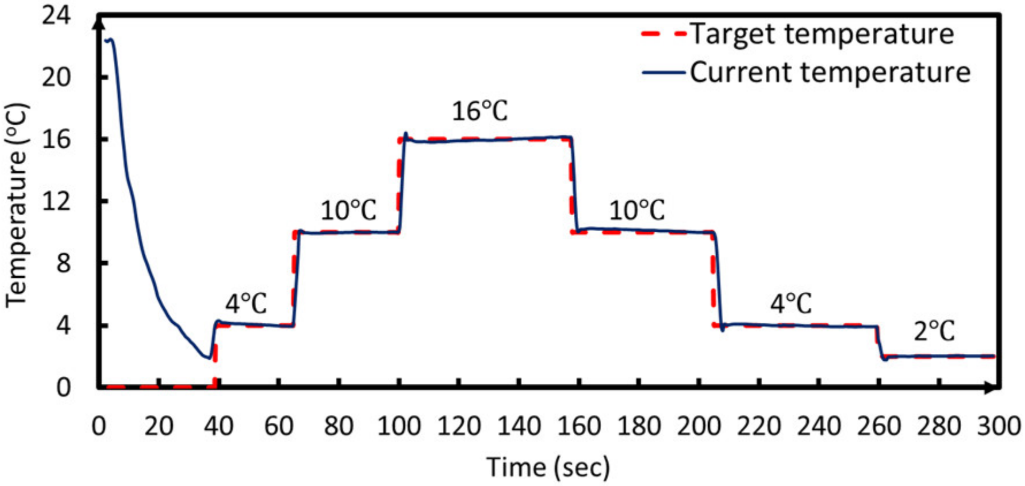

Figure 6.2: On-chip temperature history with active cooling and heating microfluidic

the develoed cell confinement and manipulation platform, this kind of attempts to introduce trahalose inside the cell membrane can be conducted in more controlled and effective way. Another candidate of novel CPAs we are working on now is Betaine, which has been widely used in chemical engineering for protecting protein and nucleotides from themal and osmotic damages. As to its excellent biocompatibility and acting as a osmotic regulator, recent research has indicated the potencial of Betaine as a novel CPA type [139], both used independently or as a combination with traditional CPA.

BIBLIOGRAPHY

[1] LLC medtech market analysis at MedMarket Diligence. Applications, global markets in tissue engineering and cell therapy. `https://blog.mediligence.com/2014/04/17/applications-global-markets-in-tissue-engineering-and-cell-therapy/`.

[2] Doyong Gao and J. K. Critser. Mechanisms of cryoinjury in living cells. *ILAR Journal*, 41(4):187–196, 2000.

[3] Peter Mazur. Cryobiology: The freezing of biological systems. *Science*, 168(3934):939–949, 1970.

[4] Gang Zhao and Jianping Fu. Microfluidics for cryopreservation. *Biotechnology Advances*, 35(2):323–336, 2017.

[5] C. Polge, A. U. Smith, and A. S. Parkes. Revival of spermatozoa after vitrification and dehydration at low temperatures. *Nature*, 164(4172):666, 1949.

[6] E. D. Thomas, H. L. Lochte, W. C. Lu, and J. W. Ferrebee. Intravenous infusion of bone marrow in patients receiving radiation and chemotherapy. *The New England Journal of Medicine*, 257(11):491, 1957.

[7] idem A. Akkk, Mette R. Holte, Jon M. Tangen, Bjrn stenstad, and ystein Bruserud. Hematopoietic engraftment of dimethyl sulfoxidedepleted autologous peripheral blood progenitor cells. *Transfusion*, 49(2):354–361, 2009.

[8] A. M. Bakken, O. Bruserud, and J. F. Abrahamsen. No differences in colony formation of peripheral blood stem cells frozen with 5 *Journal of hematotherapy and stem cell research*, 12(3):351, 2003.

[9] R. Cordoba, R. Arrieta, A. Kerguelen, and F. Hernandez-Navarro. The occurrence of adverse events during the infusion of autologous peripheral blood stem cells is related to the number of granulocytes in the leukapheresis product. *Bone Marrow Transplantation*, 40(11):1063, 2007.

[10] E. Fos, M. Desmartin, S. Benhamida, F. Xavier, V. Vanneaux, D. Rea, J. P. Fermand, B. Arnulf, N. Mounier, M. Ertault, J. P. Lotz, L. Galicier, E. Raffoux, M. Benbunan, J. P. Marolleau, and J. Larghero. Recovery, viability and clinical toxicity of thawed and

washed haematopoietic progenitor cells: analysis of 952 autologous peripheral blood stem cell transplantations. *Bone Marrow Transplantation*, 40(9):831, 2007.

[11] J. D. Hidalgo, R. Krone, M. W. Rich, K. Blum, D. Adkins, M. Y. Fan, R. Brown, S. Devine, T. Graubert, W. Blum, M. Tomasson, L. T. Goodnough, R. Vij, J. Dipersio, and H. Khoury. Supraventricular tachyarrhythmias after hematopoietic stem cell transplantation: incidence, risk factors and outcomes. *Bone Marrow Transplantation*, 34(7):615, 2004.

[12] Yuji Hirata, Koji Kishino, Fumiko Onozaki, Yoko Nakaki, Shin-Ichiro Fujiwara, Chizuru Yamamoto, Kazuya Sato, Tomohiro Matsuyama, Katsutoshi Ozaki, Masaki Mori, Keiya Ozawa, and Kazuo Muroi. Use of cryoprotectant-depleted allogeneic peripheral blood stem cells for transplantation. *Hematology (Amsterdam, Netherlands)*, 16(4):221, 2011.

[13] Ayhan Donmez, Murat Tombuloglu, Ayse Gungor, Nur Soyer, Guray Saydam, and Seckin Cagirgan. Clinical side effects during peripheral blood progenitor cell infusion. *Transfusion and Apheresis Science*, 36(1):95–101, 2007.

[14] Zaher K. Otrock, Ahmad Beydoun, Wissam M. Barada, Rami Masroujeh, Rola Hourani, and Ali Bazarbachi. Transient global amnesia associated with the infusion of dmso-cryopreserved autologous peripheral blood stem cells. *Haematologica*, 93(3):e36, 2008.

[15] A. M. Jnior, C. A. Arrais, R. Saboya, R. D. Velasques, P. L. Junqueira, and F. L. Dulley. Neurotoxicity associated with dimethylsulfoxide-preserved hematopoietic progenitor cell infusion. *Bone Marrow Transplantation*, 41(1):95, 2007.

[16] P. F. Scholander, L. Van Dam, J. W. Kanwisher, H. T. Hammel, and M. S. Gordon. Supercooling and osmoregulation in arctic fish. *Journal of Cellular and Comparative Physiology*, 49(1):5–24, 1957.

[17] M. Juliana McElrath and Barton F. Haynes. Induction of immunity to human immunodeficiency virus type-1 by vaccination. *Immunity*, 33(4):542–554, 2010.

[18] Lyle R. McKinnon, Sean M. Hughes, Stephen C. De Rosa, Jeffrey A. Martinson, Jill Plants, Kirsten E. Brady, Pamela P. Gumbi, Devin J. Adams, Lucia Vojtech, Christine G. Galloway, Michael Fialkow, Gretchen Lentz, Dayong Gao, Zhiquan Shu, Billy Nyanga, Preston Izulla, Joshua Kimani, Steve Kimwaki, Alfred Bere, Zoe Moodie, Alan L. Landay, Jo-Ann S. Passmore, Rupert Kaul, Richard M. Novak, M. Juliana McElrath, and Florian Hladik. Optimizing viable leukocyte sampling from the female

genital tract for clinical trials: An international multi-site study.(research article). *PLoS ONE*, 9(1):e85675, 2014.

[19] W. Virgin Herbert and D. Walker Bruce. Immunology and the elusive aids vaccine. *Nature*, 464(7286):224, 2010.

[20] Craig R. Cohen, Anna-Barbara Moscicki, Mark E. Scott, Yifei Ma, Stephen Shiboski, Elizabeth Bukusi, Ibrahim Daud, Anu Rebbapragada, Joelle Brown, and Rupert Kaul. Increased levels of immune activation in the genital tract of healthy young women from sub-saharan africa. *AIDS (London, England)*, 24(13):2069, 2010.

[21] Phalguni Gupta, Deena Ratner, Bruce K. Patterson, Kathy Kulka, Lisa C. Rohan, Michael A. Parniak, Charles E. Isaacs, and Sharon Hillier. Use of frozen-thawed cervical tissues in the organ culture system to measure anti-hiv activities of candidate microbicides. *AIDS research and human retroviruses*, 22(5):419, 2006.

[22] Lenine J. Liebenberg, Hoyam Gamieldien, Nonhlanhla N. Mkhize, Shameem Z. Jaumdally, Pam P. Gumbi, Lynette Denny, and Jo-Ann S. Passmore. Stability and transport of cervical cytobrushes for isolation of mononuclear cells from the female genital tract. *Journal of Immunological Methods*, 367(1-2):47–55, 2011.

[23] Ian McGowan, Karen Tanner, Julie Elliott, Javier Ibarrondo, Elena Khanukhova, Charina McDonald, Terry Saunders, Peter A. Anton, and Ying Zhou. Nonreproducibility of ”snap-frozen” rectal biopsies for later use in ex vivo explant infectibility studies. *AIDS Research and Human Retroviruses*, 28(11):1509–1512, 2012.

[24] Peter Mazur. Equilibrium, quasi- equilibrium, and nonequilibrium freezing of mammalian embryos. *Cell Biophysics*, 17(1):53–92, 1990.

[25] P. Mazur. Freezing of living cells: mechanisms and implications. *The American journal of physiology*, 247(3):C125–142, 1984.

[26] P. Mazur. Kinetics of water loss from cells at subzero temperatures and the likelihood of intracellular freezing. *The Journal of general physiology*, 47:347, 1963.

[27] Hsiu-Hung Chen, Jester J. P. Purtteman, Shelly Heimfeld, Albert Folch, and Dayong Gao. Development of a microfluidic device for determination of cell osmotic behavior and membrane transport properties. *Cryobiology*, 55(3):200–209, 2007.

[28] Hsiu-Hung Chen, Hong Shen, Shelly Heimfeld, Kenny K. Tran, Joanna Reems, Albert Folch, and Dayong Gao. A microfluidic study of mouse dendritic cell membrane transport properties of water and cryoprotectants. *International Journal of Heat and Mass Transfer*, 51(23):5687–5694, 2008.

[29] S. R. Gunn and M. S. Nixon. A robust snake implementation a dual active contour. *Pattern Analysis and Machine Intelligence, IEEE Transactions on*, 19(1):63–68, 1997.

[30] D. Y. Gao, C. T. Benson, C. Liu, J. J. McGrath, E. S. Critser, and J. K. Critser. Development of a novel microperfusion chamber for determination of cell membrane transport properties. *Biophysical Journal*, 71(1):443–450, 1996.

[31] J. J. McGrath. Quantitative measurement of cell membrane transport: Technology and applications. *Cryobiology*, 34(4):315–334, 1997.

[32] Hy Tseng, S. J. Sun, Zq Shu, W. P. Ding, Ja Reems, and Dy Gao. A microfluidic study of megakaryocytes membrane transport properties to water and dimethyl sulfoxide at suprazero and subzero temperatures. *Biopreservation And Biobanking*, 9(4):355–362, 2011.

[33] Igor I. Katkov. A two-parameter model of cell membrane permeability for multisolute systems. *Cryobiology*, 40(1):64–83, 2000.

[34] F. W. Kleinhans. Membrane permeability modeling: Kedem katchalsky vs a two-parameter formalism. *Cryobiology*, 37(4):271–289, 1998.

[35] M. H. Jacobs. The simultaneous measurement of cell permeability to water and to dissolved substances. *The American Journal of the Medical Sciences*, 185(4):599, 1933.

[36] Gm Whitesides. The origins and the future of microfluidics. *Nature*, 442(7101):368–373, 2006.

[37] Henrik Bruus. *Theoretical microfluidics.* Oxford : Oxford University Press, Oxford, 2008.

[38] George Karniadakis. *Microflows and nanoflows : fundamentals and simulation.* New York, NY : Springer, New York, NY, 2005.

[39] D. J. Beebe, G. A. Mensing, and G. M. Walker. Physics and applications of microfluidics in biology. *Annual Review of Biomedical Engineering*, 4:261–286, 2002.

[40] Guilhem Velve-Casquillas, Mal Le Berre, Matthieu Piel, and Phong T. Tran. Microfluidic tools for cell biological research. *Nano Today*, 5(1):28–47, 2010.

[41] Jacques Leng and Jean-baptiste Salmon. Microfluidic crystallization. *Lab on a Chip*, 9(1):24–34, 2009.

[42] Yo Tanaka, Kae Sato, Tatsuya Shimizu, Masayuki Yamato, Teruo Okano, and Takehiko Kitamori. Biological cells on microchips: new technologies and applications. *Biosensors and bioelectronics*, 23(4):449, 2007.

[43] Shingo Okushima, Takasi Nisisako, Toru Torii, and Toshiro Higuchi. Controlled production of monodisperse double emulsions by two-step droplet breakup in microfluidic devices. *Langmuir*, 20(23):9905–9908, 2004. PMID: 15518471.

[44] Zhihong Nie, Wei Li, Minseok Seo, Shengqing Xu, and Eugenia Kumacheva. Janus and ternary particles generated by microfluidic synthesis: design, synthesis, and self-assembly. *Journal of the American Chemical Society*, 128(29):9408–9412, 2006. PMID: 16848476.

[45] Helen Song, Joshua D. Tice, and Rustem F. Ismagilov. A microfluidic system for controlling reaction networks in time. *Angewandte Chemie*, 115(7):792–796, 2003.

[46] Sarah Koster, Francesco E. Angile, Honey Duan, Jeremy J. Agresti, Anton Wintner, Christian Schmitz, Amy C. Rowat, Christoph A. Merten, Dario Pisignano, Andrew D. Griffiths, and David A. Weitz. Drop-based microfluidic devices for encapsulation of single cells. *Lab Chip*, 8:1110–1115, 2008.

[47] Lotien Richard Huang, Edward C. Cox, Robert H. Austin, and James C. Sturm. Continuous particle separation through deterministic lateral displacement. *Science*, 304(5673):987–990, 2004.

[48] Daniel R. Gossett, Henry T. K. Tse, Serena A. Lee, Yong Ying, Anne G. Lindgren, Otto O. Yang, Jianyu Rao, Amander T. Clark, and Dino Di Carlo. Hydrodynamic stretching of single cells for large population mechanical phenotyping. *Proceedings of the National Academy of Sciences*, 109(20):7630–7635, 2012.

[49] T. T. Perkins, D. E. Smith, and S. Chu. Single polymer dynamics in an elongational flow. *Science (New York, N.Y.)*, 276(5321):2016, 1997.

[50] Ivar Meyvantsson and David J. Beebe. Cell culture models in microfluidic systems. *Annual Review of Analytical Chemistry*, 1:423–449, 2008.

[51] Nianzhen Li, Anna Tourovskaia, and Albert Folch. Biology on a chip: Microfabrication for studying the behavior of cultured cells. *Critical Reviews in Biomedical Engineering*, 31(5-6):423–488, 2003.

[52] S. Takayama, Jc McDonald, E. Ostuni, Mn Liang, Pja Kenis, Rf Ismagilov, and Gm Whitesides. Patterning cells and their environments using multiple laminar fluid

flows in capillary networks. *Proceedings Of The National Academy Of Sciences Of The United States Of Ame*, 96(10):5545–5548, 1999.

[53] A. Jain and K. E. Goodson. Thermal microdevices for biological and biomedical applications. *Journal of Thermal Biology*, 36(4):209–218, 2011.

[54] G. Maltezos, A. Gomez, J. Zhong, F. A. Gomez, and A. Scherer. Microfluidic polymerase chain reaction. *Applied Physics Letters*, 93(24):243901, 2008.

[55] A. I. K. Lao, T. M. H. Lee, I. M. Hsing, and N. Y. Ip. Precise temperature control of microfluidic chamber for gas and liquid phase reactions. *Sensors and Actuators a-Physical*, 84(1-2):11–17, 2000.

[56] A. Manz, N. Graber, and H. M. Widmer. Miniaturized total chemical-analysis systems - a novel concept for chemical sensing. *Sensors and Actuators B-Chemical*, 1(1-6):244–248, 1990.

[57] Dino Di Carlo, Daniel Irimia, Ronald G Tompkins, and Mehmet Toner. Continuous inertial focusing, ordering, and separation of particles in microchannels. *Proceedings of the National Academy of Sciences*, 104(48):18892–18897, 2007.

[58] Masumi Yamada, Megumi Nakashima, and Minoru Seki. Pinched flow fractionation: continuous size separation of particles utilizing a laminar flow profile in a pinched microchannel. *Analytical chemistry*, 76(18):5465–5471, 2004.

[59] Lotien Richard Huang, Edward C Cox, Robert H Austin, and James C Sturm. Continuous particle separation through deterministic lateral displacement. *Science*, 304(5673):987–990, 2004.

[60] Emil Chmela, Robert Tijssen, Marko T Blom, Han JGE Gardeniers, and Albert van den Berg. A chip system for size separation of macromolecules and particles by hydrodynamic chromatography. *Analytical chemistry*, 74(14):3470–3475, 2002.

[61] M. Evander, L. Johansson, T. Lilliehorn, J. Piskur, M. Lindvall, S. Johansson, M. Almqvist, T. Laurell, and J. Nilsson. Noninvasive acoustic cell trapping in a microfluidic perfusion system for online bioassays. *Anal. Chem.*, 79(7):2984–2991, 2007.

[62] H. M. Hertz. Standing-wave acoustic trap for nonintrusive positioning of microparticles. *Journal of Applied Physics*, 78(8):4845–4849, 1995.

[63] Ahj Yang, S. D. Moore, B. S. Schmidt, M. Klug, M. Lipson, and D. Erickson. Optical manipulation of nanoparticles and biomolecules in sub-wavelength slot waveguides. *Nature*, 457(7225):71–75, 2009.

[64] A. E. Cohen. Control of nanoparticles with arbitrary two-dimensional force fields. *Physical Review Letters*, 94(11):118102, 2005.

[65] B. G. Hosu, K. Jakab, P. Banki, F. I. Toth, and G. Forgacs. Magnetic tweezers for intracellular applications. *Review of Scientific Instruments*, 74(9):4158–4163, 2003.

[66] V. H. Lieu, T. A. House, and D. T. Schwartz. Hydrodynamic tweezers: Impact of design geometry on flow and microparticle trapping. *Analytical Chemistry*, 84(4):1963–1968, 2012.

[67] Melikhan Tanyeri and Charles M. Schroeder. Manipulation and confinement of single particles using fluid flow. *Nano Letters*, 13(6):2357–2364, 2013. PMID: 23682823.

[68] G. I. Taylor. The formation of emulsions in definable fields of flow. *Proceedings of the Royal Society of London. Series A, Containing Papers of a Mathematical and Physical Character (1905-1934)*, 146(858):501–523, 1934.

[69] Lee Joo Sung, Dylla-Spears Rebecca, P. Teclemariam Nerayo, and J. Muller Susan. Microfluidic four-roll mill for all flow types. *Applied Physics Letters*, 90:074103, 2007.

[70] Pr Start, S. D. Hudson, Ek Hobble, and Kb Migler. Breakup of carbon nanotube flocs in microfluidic traps. *J. Colloid Interface Sci.*, 297(2):631–636, 2006.

[71] S. D. Hudson, Fr Phelan, M. D. Handler, Jt Cabral, Kb Migler, and Ej Amis. Microfluidic analog of the four-roll mill. *Appl. Phys. Lett.*, 85(2):335–337, 2004.

[72] B. J. Bentley and L. G. Leal. A computer-controlled four-roll mill for investigations of particle and drop dynamics in two-dimensional linear shear flows. *J. Fluid. Mech.*, 167:219–240, 1986.

[73] Charles Schroeder, Rodrigo Teixeira, Eric Shaqfeh, and Steven Chu. Characteristic periodic motion of polymers in shear flow. *Physical Review Letters*, 95(1):025025, 2005.

[74] Charles M. Schroeder, Hazen P. Babcock, Eric S. G. Shaqfeh, and Steven Chu. Observation of polymer conformation hysteresis in extensional flow. *Science (New York, N.Y.)*, 301(5639):1515, 2003.

[75] De Smith, Hp Babcock, and S. Chu. Single-polymer dynamics in steady shear flow. *Science*, 283(5408):1724–1727, 1999.

[76] M. A. Unger, H. P. Chou, T. Thorsen, A. Scherer, and S. R. Quake. Monolithic microfabricated valves and pumps by multilayer soft lithography. *Science (New York, N.Y.)*, 288(5463):113, 2000.

[77] K. Au Anthony, Lai Hoyin, R. Utela Ben, and Folch Albert. Microvalves and micropumps for biomemsintroduction to biomems. *Micromachines*, 2(2):179, 2011.

[78] M. Tanyeri, M. Ranka, N. Sittipolkul, and C. M. Schroeder. A microfluidic-based hydrodynamic trap: design and implementation. *Lab on a Chip*, 11(10):1786–1794, 2011.

[79] C. Wyatt Shields Iv, Catherine D. Reyes, and Gabriel P. Lpez. Microfluidic cell sorting: a review of the advances in the separation of cells from debulking to rare cell isolation. *Lab Chip*, 15(5):1230–1249, 2015.

[80] Tomoyuki Yasukawa, Kuniaki Nagamine, Yoshiko Horiguchi, Hitoshi Shiku, Masahiro Koide, Tomoaki Itayama, Fujio Shiraishi, and Tomokazu Matsue. Electrophoretic cell manipulation and electrochemical gene-function analysis based on a yeast two-hybrid system in a microfluidic device.(author abstract)(report). *Analytical Chemistry*, 80(10):3722, 2008.

[81] I. Barbulovic-Nad, H. Yang, P. S. Park, and Ar Wheeler. Digital microfluidics for cell-based assays. *Lab Chip*, 8(4):519–526, 2008.

[82] G. Velve Casquillas, C. Fu, M. Le Berre, J. Cramer, S. Meance, A. Plecis, D. Baigl, J. J. Greffet, Y. Chen, M. Piel, and P. T. Tran. Fast microfluidic temperature control for high resolution live cell imaging. *Lab Chip*, 11(3):484–9, 2011.

[83] Keryn Lian, Shawn O'Rourke, Daniel Sadler, Manes Eliacin, Claudia Gamboa, Robert Terbrueggen, and Marc Chason. Integrated microfluidic components on a printed wiring board platform. *Sensors and Actuators: B. Chemical*, 138(1):21–27, 2009.

[84] D. Resnik, D. Vrtacnik, M. Mozek, B. Pecar, and S. Amon. Experimental study of heat-treated thin film ti/pt heater and temperature sensor properties on a si microfluidic platform. *Journal of Micromechanics and Microengineering*, 21(2):018301, 2011.

[85] H. Yang, C. A. Choi, K. H. Chung, C. H. Jun, and Y. T. Kim. An independent, temperature-controllable microelectrode array. *Analytical Chemistry*, 76(5):1537–1543, 2004.

[86] K. S. Lee, P. Boccazzi, A. J. Sinskey, and R. J. Ram. Microfluidic chemostat and turbidostat with flow rate, oxygen, and temperature control for dynamic continuous culture. *Lab Chip*, 11(10):1730–9, 2011.

[87] V. Bazargan and B. Stoeber. Flow control using a thermally actuated microfluidic relay valve. *J. Microelectromech. Syst.*, 19(5):1079–1087, 2010.

[88] H. Bridle, M. Millingen, and A. Jesorka. On-chip fabrication to add temperature control to a microfluidic solution exchange system. *Lab Chip*, 8(3):480–3, 2008.

[89] L. Y. Liu, S. L. Peng, W. J. Wen, and P. Sheng. Micro thermoindicators and optical-electronic temperature control for microfluidic applications. *Applied Physics Letters*, 91(9):093513, 2007.

[90] Jonathan D Adams, Christian L Ebbesen, Rune Barnkob, Allen H J Yang, H Tom Soh, and Henrik Bruus. High-throughput, temperature-controlled microchannel acoustophoresis device made with rapid prototyping. *Journal of Micromechanics and Microengineering*, 22(7):075017, 2012.

[91] Hyung-il Lee, Joanna Pietrasik, Sergei S Sheiko, and Krzysztof Matyjaszewski. Stimuli-responsive molecular brushes. *Progress in Polymer Science*, 35(1):24–44, 2010.

[92] Lior Atia and Sefi Givli. A theoretical study of biological membrane response to temperature gradients at the single-cell level. *Journal of The Royal Society Interface*, 11(95):20131207, 2014.

[93] Vincent Miralles, Axel Huerre, Florent Malloggi, and Marie-Caroline Jullien. A review of heating and temperature control in microfluidic systems: techniques and applications. *Diagnostics*, 3(1):33–67, 2013.

[94] P. Bhattacharyya. Technological journey towards reliable microheater development for mems gas sensors: A review. *IEEE Trans. Device Mater. Reliab.*, 14(2):589–599, 2014.

[95] Lord Rayleigh. On the capillary phenomena of jets. *Proceedings of the Royal Society of London (1854-1905)*, 29(196):71–97, 1879.

[96] Pierre-Gilles de Gennes. *Capillarity and wetting phenomena : drops, bubbles, pearls, waves.* New York : Springer, New York, 2004.

[97] L. Anna Shelley, Bontoux Nathalie, and A. Stone Howard. Formation of dispersions using flow focusing in microchannels. *Applied Physics Letters*, 82:364, 2003.

[98] Todd M. Squires and Stephen R. Quake. Microfluidics: Fluid physics at the nanoliter scale. *Reviews of Modern Physics*, 77(3):977–1026, 2005.

[99] Benjamind Hamlington, Benjamin Steinhaus, Jamesj Feng, Darren Link, Michaelj Shelley, and Amyq Shen. Liquid crystal droplet production in a microfluidic device. *Liquid Crystals*, 34(7):861–870, 2007.

[100] E. M. Johnson-Chavarria, U. Agrawal, M. Tanyeri, T. E. Kuhlman, and C. M. Schroeder. Automated single cell microbioreactor for monitoring intracellular dynamics and cell growth in free solution. *Lab on a Chip*, 14(15):2688–2697, 2014.

[101] C. V. Paganelli and A. K. Solomon. The rate of exchange of tritiated water across the human red cell membrane. *The Journal of general physiology*, 41(2):259, 1957.

[102] Robert L. Macey and Robert E. L. Farmer. Inhibition of water and solute permeability in human red cells. *BBA - Biomembranes*, 211(1):104–106, 1970.

[103] F. W. Kleinhans, V. S. Travis, Junying Du, P. M. Villines, K. E. Colvin, and J. K. Critser. Measurement of human sperm intracellular water volume by electron spin resonance. *Journal of Andrology*, 13(6):498–506, 1992.

[104] J. A. Gilmore, L. E. McGann, J. Liu, D. Y. Gao, A. T. Peter, F. W. Kleinhans, and J. K. Critser. Effect of cryoprotectant solutes on water permeability of human spermatozoa. *Biology of reproduction*, 53(5):985, 1995.

[105] Chi Liu, Charles T. Benson, Dayong Gao, Brian W. Haag, Locksley E. McGann, and John K. Critser. Water permeability and its activation energy for individual hamster pancreatic islet cells. *Cryobiology*, 32(5):493–502, 1995.

[106] L. McGann, A. Turner, and J. M. Turc. Microcomputer interface for rapid measurements of average volume using an electronic particle counter. *Med. Biol. Eng. Comput.*, 20(1):117–120, 1982.

[107] D. Y. Gao, J. J. McGrath, Jun Tao, C. T. Benson, E. S. Critser, and J. K. Critser. Membrane transport properties of mammalian oocytes: a micropipette perfusion technique. *Journal of Reproduction and Fertility*, 102(2):385–392, 1994.

[108] S. Leibo. Water permeability and its activation energy of fertilized and unfertilized mouse ova. *J. Membrain Biol.*, 53(3):179–188, 1980.

[109] J. J. McGrath. A microscope diffusion chamber for the determination of the equilibrium and non equilibrium osmotic response of individual cells. *Journal of Microscopy*, 139(3):249–263, 1985.

[110] R. Scott Martin, Paul D. Root, and Dana M. Spence. Microfluidic technologies as platforms for performing quantitative cellular analyses in an in vitro environment. *Analyst*, 131:1197–1206, 2006.

[111] Yong Zeng and Tanyu Wang. Quantitative microfluidic biomolecular analysis for systems biology and medicine. *Anal Bioanal Chem*, 405(17):5743–5758, 2013.

[112] B. Okumus, S. Yildiz, and E. Toprak. Fluidic and microfluidic tools for quantitative systems biology. *Current Opinion in Biotechnology*, 25:30–38, 2014.

[113] Long Cai, Nir Friedman, and X. Sunney Xie. Stochastic protein expression in individual cells at the single molecule level. *Nature*, 440(7082):358, 2006.

[114] Michelle L. Kovarik and Nancy L. Allbritton. Measuring enzyme activity in single cells. *Trends in Biotechnology*, 29(5):222–230, 2011.

[115] Michelle L. Kovarik, Pavak K. Shah, Paul M. Armistead, and Nancy L. Allbritton. Microfluidic chemical cytometry of peptide degradation in single drug-treated acute myeloid leukemia cells. *Anal. Chem.*, 85(10):4991–4997, 2013.

[116] Samuel K. Sia and George M. Whitesides. Microfluidic devices fabricated in poly(dimethylsiloxane) for biological studies. *ELECTROPHORESIS*, 24(21):3563–3576, 2003.

[117] Helene Andersson and Albert van Den Berg. Microfluidic devices for cellomics: a review. *Sensors and Actuators B: Chemical*, 92(3):315–325, 2003.

[118] Matthew R. Bennett and Jeff Hasty. Microfluidic devices for measuring gene network dynamics in single cells. *Nat Rev Genet*, 10(9):628–638, 2009.

[119] Dino Di Carlo, Liz Y. Wu, and Luke P. Lee. Dynamic single cell culture array. *Lab Chip*, 6:1445–1449, 2006.

[120] Dino Di Carlo and Luke P. Lee. Dynamic single-cell analysis for quantitative biology. *Anal. Chem.*, 78(23):7918–7925, 2006.

[121] Jacqueline R. Rettig and Albert Folch. Large-scale single-cell trapping and imaging using microwell arrays. *Anal. Chem.*, 77(17):5628–5634, 2005.

[122] Tanyeri Melikhan, M. Johnson-Chavarria Eric, and M. Schroeder Charles. Hydrodynamic trap for single particles and cells. *Applied Physics Letters*, 96:224101, 2010.

[123] Cifeng Fang, Doojin Lee, Boris Stober, Gerald G. Fuller, and Amy Q. Shen. Integrated microfluidic platform for instantaneous flow and localized temperature control. *RSC Advances,*, 5(104):85620–85629, 2015.

[124] Anish Shenoy, Christopher V. Rao, and Charles M. Schroeder. Stokes trap for multiplexed particle manipulation and assembly using fluidics. *Proceedings of the National Academy of Sciences*, 113(15):3976–3981, 2016.

[125] Keir Neuman, Edmund Chadd, Grace Liou, Keren Bergman, and Steven Block. Characterization of photodamage to escherichia coli in optical traps. *Biophysical Journal*, 77(5):2856–63, 1999.

[126] A. Weiss, R. L. Wiskocil, and J. D. Stobo. The role of t3 surface molecules in the activation of human t cells: A two-stimulus requirement for il 2 production reflects events occuring at a pre-translational level. *Journal of Immunology*, 133(1):123–128, 1984.

[127] Hiroshi Takamatsu, Yuichi Komori, Sylwia Zawlodzka, and Motoo Fujii. Quantitative examination of a perfusion microscope for the study of osmotic of cells. *Journal of Biomechanical Engineering*, 126(4):402–409, 2004.

[128] A. M. Vian and A. Z. Higgins. Membrane permeability of the human granulocyte to water, dimethyl sulfoxide, glycerol, propylene glycol and ethylene glycol. *Cryobiology*, 68:35–42, 2014.

[129] H. G. Hempling, S. Thompson, and A. Dupre. Osmotic properties of human lymphocyte. *Journal Of Cellular Physiology*, 93(2):293–302, 1977.

[130] Zhiquan Shu, Sean M. Hughes, Cifeng Fang, Jinghua Huang, Baiwen Fu, Gang Zhao, Michael Fialkow, Gretchen Lentz, Florian Hladik, and Dayong Gao. A study of the osmotic characteristics, water permeability, and cryoprotectant permeability of human vaginal immune cells. *Cryobiology*, 72(2):93–99, 2016.

[131] Nicole Bobak, Vladimir L. Bittner, and et al. Volume regulation of murine t lymphocytes relies on voltage-dependent and two-pore domain potassium channels. *BBA - Biomembranes*, 1808(8):2036–2044, 2011.

[132] Andreas Blicher, Katarzyna Wodzinska, Matthias Fidorra, Mathias Winterhalter, and Thomas Heimburg. The temperature dependence of lipid membrane permeability, its quantized nature, and the influence of anesthetics. *Biophysical Journal*, 96(11):4581 – 4591, 2009.

[133] J. E. Hunter, A. Bernard, B. J. Fuller, J. J. McGrath, and R. W. Shaw. Measurements of the membrane water permeability (lp) and its temperature dependence (activation energy) in human fresh and failed-to-fertilize oocytes and mouse oocyte. *Cryobiology*, 29(2):240–249, 1992.

[134] Peter Mazur and Robert H. Miller. Permeability of the human erythrocyte to glycerol in 1 and 2 m solutions at 0 or 20 c. *Cryobiology*, 13(5):507–522, 1976.

[135] Peter Mazur, S. Leibo, and R. Miller. Permeability of the bovine red cell to glycerol in hyperosmotic solutions at various temperatures. *The Journal of Membrane Biology*, 15(1):107–136, 1974.

[136] Ora Kedem. Commentary on 'thermodynamic analysis of the permeability of biological membranes to non-electrolytes' by o. kedem and a. katchalsky biochim. biophys. acta 27 (1958) 229-246. *BBA - Biochimica et Biophysica Acta*, 1000(C):411–430, 1989.

[137] As Verkman, An Vanhoek, Th Ma, A. Frigeri, Wr Skach, A. Mitra, Bk Tamarappoo, and J. Farinas. Water transport across mammalian cell membranes. 270:C12–C30, 1996.

[138] Hai-Liang Wang and Li Sun. Comparative metagenomics reveals insights into the deep-sea adaptation mechanism of the microorganisms in iheya hydrothermal fields. *World Journal of Microbiology and Biotechnology*, 33(5):1–17, 2017.

[139] Jing Yang, Nana Cai, Hongwen Zhai, Jiamin Zhang, Yingnan Zhu, and Lei Zhang. Natural zwitterionic betaine enables cells to survive ultrarapid cryopreservation. *Scientific Reports (Nature Publisher Group)*, 6:37458, 2016.

[140] R. Dylla-Spears, Je Townsend, L. Jen-Jacobson, Ll Sohn, and S. J. Muller. Single-molecule sequence detection via microfluidic planar extensional flow at a stagnation point. *Lab Chip*, 10(12):1543–1549, 2010.

[141] D. Qin, Yn Xia, and Gm Whitesides. Soft lithography for micro- and nanoscale patterning. *Nat. Protoc.*, 5(3):491–502, 2010.

[142] Mihrimah Ozkan, Mark Wang, Cengiz Ozkan, Richard Flynn, and Sadik Esener. Optical manipulation of objects and biological cells in microfluidic devices. *Biomedical Microdevices*, 5(1):61–67, 2003.

[143] Jonathan D. Adams, Christian L. Ebbesen, Rune Barnkob, Allen H. J. Yang, H. Tom Soh, and Henrik Bruus. High- throughput, temperature- controlled microchannel acoustophoresis device made with rapid prototyping. *High-throughput,*

temperature-controlled microchannel acoustophoresis device made with rapid prototyping, 22(7):075017, 2012.

[144] David E. Pegg. Principles of cryopreservation. *Methods in molecular biology (Clifton, N.J.)*, 1257:3, 2015.

[145] Else Hoffmann, Ian Lambert, and Stine Pedersen. Physiology of cell volume regulation in vertebrates. *Physiol Rev.*, 89:193, 2009.

[146] A. M. Porsche, C. Korber, S. Englich, U. Hartmann, and G. Rau. Determination of the permeability of human-lymphocytes with a microscope diffusion chamber. *Cryobiology*, 23(4):302–316, 1986.

[147] Torsten Vilkner, Dirk Janasek, and Andreas Manz. Micro total analysis systems. recent developments. *Anal. Chem.*, 76(12):3373, 2004.

[148] Colin J. Ingham and Johan E. T. Van Hylckama Vlieg. Mems and the microbe. *Lab chip*, 8(10):1604–1616, 2008.